KU LEUVEN

ARENBERG DOCTORAL SCHOOL
FACULTY OF SCIENCE

Defect detection in a vibrating structure by combining linear and nonlinear piezo-ultrasound signal features

Sebastiaan Creten

Promotor:
Prof. Dr. C. Glorieux

Dissertation presented in partial fulfilment of the requirements for the degree of Doctor of Science: Physics

July 2014

Faculteit Wetenschappen
Celestijnenlaan 200D
B-3001 Leuven (Heverlee)
Belgium

ISBN 978-90-8649-735-5

Acknowledgements

I would like to thank my promotor, Christ Glorieux, for the opportunities and guidance he gave me, during the seven years we collaborated. I would also like to express my gratitude to the ATF staff and to my colleagues, who all contributed in the creation of this work. As always, I would like to thank Liesbeth, my parents, my family and my friends for their relentless support.

Sebastiaan Creten

Abstract

The development of non-destructive evaluation techniques is motivated by the strong demand for the use of lightweight materials in critical components, especially in aeronautical applications, and by the economical drive to keep civil and large mass-produced structures in operation for much longer than originally foreseen. In both situations, it is important to detect damage at the earliest possible stage in order to ensure reliably and safe use. Several linear and nonlinear ultrasonic non-destructive testing techniques are available, nevertheless their practical implementation is still limited. Linear ultrasonic techniques are inadequate when closed cracks need to be detected. The lack in differentiation between sources of nonlinearity makes defects undistinguishable from e.g. nonlinearity induced by mechanical contacts. Additionally, most NDT-techniques are not capable of damage detection under harsh operational conditions. This work presents and validates a technique to detect damage, addressing the aforesaid difficulties in vibrating structures.

The nonlinear interaction of a probing Lamb wave with an air-filled delamination in a steel/rubber bilayer undergoing slow, periodical vibrations is studied. The physical properties of the air layer are periodically changing due to compression, and hence the transmission of the probe wave is dynamically modulated. The dispersion characteristics of the Lamb modes in the steel/air/rubber structure are studied for different thermodynamical (isolated/non isolated) models of air confinement. The coupling between the rubber layer and the steel layer strongly increases close to the cut-off frequencies for longitudinal waves. This effect is accompanied by large changes in the physical properties of the probe wave. In the vicinity of these coupling conditions, the cross-modulation of the probe wave is expected to be maximum. This is validated by a simulation of a dynamically changing delamination. In order to elucidate the optimum conditions for cross-modulation, the relation between the cut-off frequency and the delamination properties is analytically studied. The resulting coupling condition

is a good approximation of the probe frequency- and compression-range at which the steel-rubber coupling is maximum, and consequently in the vicinity of which the cross-modulation is maximum.

Sensing systems to measure transmission amplitudes, using ultrasonic probe waves, are studied. Because the spatial properties of Lamb waves (wavelength, velocity, displacement symmetry) depend on their specific modal nature, transducer arrays can be used to select and amplify a preferred Lamb mode. In this work, three methods of mode selection are validated, using different approaches in how the elements in the transducer array are combined. Wavelength and velocity based mode selection are achieved, with amplification factors close to the experimental maximum values. However, scattering at individual PZT-transducer strips decreases the amplitude of the probe wave propagating through the array, limiting the maximum amplification and the useful number of elements in an array. Symmetry sensitive Lamb mode selection is not feasible, due to the complicated stress patterns of Lamb waves in the PZT transducers. It can be concluded that the choice of transducers has a large influence on the performance of a specific approach.

In order to develop diagnostic algorithms based on the modulation of high frequency probe waves by a dynamically changing crack, a laboratory setup is employed in order to acquire data on two type of samples. In an aluminium plate, i.e. the first type of sample, the PZT transducers in the sensing system are subject to strong nonlinear modulation. In the second type of sample, still with a plate-like crack region, the sensing system is placed in a low strain region of the sample. Five new diagnostic algorithms are presented and compared to two linear ultrasonic techniques, i.e. two techniques using the general evolution of the transmission amplitude measured at quasi-static conditions. The new algorithms compare features of the nonlinear relation between the transmission amplitude and the load on the sample with a threshold value, in order to assess the state of the sample. In the development of these algorithms special attention goes to the requirements of a NDT technique in a practical application. The applications are robust to environmental changes, are based on durable components, while being sensitive to vibrating defects. For each specific component to be monitored, a specific choice of a diagnostic algorithm can be made according to the featured components and on the particular circumstances.

Nederlandstalig abstract

De ontwikkeling van niet-destructieve testtechnieken wordt gemotiveerd door de grote interesse in het gebruik van lichtgewichtmaterialen in kritische onderdelen van luchtvaarttoestellen, en door de economische drijf-veer om civiele- en in-serie geproduceerde structuren langer in gebruik te houden dan initieel voorzien. Om in deze situaties betrouwbaarheid en veiligheid te garanderen is het noodzakelijk schade in een zo vroeg mogelijk stadium de detecteren. Alhoewel er verschillende lineaire en niet-lineaire ultrasone niet-destructieve testtechnieken beschikbaar zijn, worden deze in de praktijk slechts zelden gebruikt. Lineaire ultrasone technieken zijn niet geschikt om gesloten defecten te detecteren. Het gebrek aan differentiatie tussen verschillende bronnen van niet-lineariteit, maakt dat niet-lineaire signaalbijdragen geïnduceerd door defecten niet onderscheidbaar zijn van deze geïnduceerd door bijvoorbeeld mechanische contacten. Bijkomend zijn de meeste NDT-technieken niet in staat schade te detecteren wanneer ze worden toegepast in extreme bedrijfsomstandigheden. In dit werk worden een aantal technieken voorgesteld en getest om defecten te detecteren in vibrerende structuren, met als doel een uitkomst te bieden aan de voornoemde uitdagingen.

De niet-lineaire interactie van een probe-Lamb-golf met een door lucht gevulde delaminatie in een traag periodiek gemoduleerde staal/rubber dubbellaag wordt bestudeerd. De fysische eigenschappen van de luchtlaag veranderen periodiek ten gevolgen van compressie, en bijgevolg wordt de transmissie van de Lamb-golf dynamisch gemoduleerd. De dispersie-eigenschappen van de Lamb-modes in de staal/lucht/rubber structuur worden bestudeerd onder verschillende thermodynamische (geïsoleerd/niet-geïsoleerd) modellen voor het gedrag van de lucht in de delaminatie. De koppeling tussen de rubberlaag en de staallaag neemt sterk toe nabij de 'cut-off' frequenties voor longitudinale golven. Dit effect gaat gepaard met grote veranderingen in de fysische eigenschappen van de Lamb-golven. Wanneer de golffrequenties en de luchtlaag-compressie de voorwaarden voor koppeling tussen de verschillende lagen benaderen, wordt de kruismodulatie van de probe-golven

en de vibratie van de luchtlaag verwacht maximaal te zijn. Dit gedrag wordt gevalideerd door een simulatie van een dynamisch veranderende delaminatie. De optimale omstandigheden voor kruismodulatie worden verder bestudeerd. Daarbij wordt de relatie tussen de cut-off frequentie en de delaminatie-eigenschappen analytisch uitgewerkt. De bekomen koppelingsvoorwaarde geeft een goede benadering van bij welke probe-frequentie en bijbehorend compressiebereik de staal-rubber koppeling maximaal is. Deze uitdrukking kan gebruikt worden om te voorspellen voor welke combinatie van frequentie en luchtlaagdikte de kruismodulatie maximaal is.

Verschillende meetopstellingen om de transmissie-amplitude van ultrasone golven te bepalen worden bestudeerd. Omdat de ruimtelijke eigenschappen van Lamb-golven (golflengte, snelheid, uitwijkingssymmetrie) karakteristieke eigenschappen zijn, kunnen transducerarrays gebruikt worden om gewenste Lamb-modes te selecteren en te versterken. In dit werk worden drie methodes om modes te selecteren getest, waarbij de elementen in de transducerarray op verschillende wijzen gecombineerd worden. Modeselectie gebaseerd op golflengte en snelheid wordt gerealiseerd met versterkingsfactoren nabij de experimenteel maximaal haalbare waarden. Desalniettemin vermindert verstrooiing aan de individuele PZT-transducers de amplitude van de probe-golf die zich door de array verplaatst. Hierdoor wordt het aantal nuttige elementen in een array beperkt. Symmetrie-selectieve Lamb-modeselectie is niet haalbaar door de moeilijke relatie tussen de stresspatronen van de Lamb-modes en de spanning gecreëerd door de PZT-elementen. Er kan besloten worden dat de keuze van transducer een grote invloed heeft op de goede werking van een bepaalde methode.

Om diagnose-algoritmes te ontwerpen, wordt een experimentele opstelling gebruikt. De algoritmes zijn gebaseerd op de modulatie van hoogfrequente probe-golven door een dynamisch variërende scheur. Met deze opstelling worden data verzameld op twee types van stalen. In een aluminium plaat, op dewelke als eerste metingen werden uitgevoerd, worden de PZT transducer in het meetsysteem sterk niet-lineair gemoduleerd. Hierdoor kunnen deze niet gebruikt worden om defectdetectie-systemen te ontwerpen. In het tweede type staal, waarin de scheur-regio nog steeds plaatachtig was, wordt het meetsysteem op een locatie met weinig rek geplaatst. Deze modificatie leidt tot een aanzienlijke vermindering in de ongewilde modulatie van het meetsysteem. Vijf nieuwe diagnose-algoritmes worden voorgesteld en vergeleken met twee lineaire ultrasone technieken. Deze twee laatsten maken gebruik van de algemene evolutie van de transmissie-amplitude gemeten in quasi statische omstandigheden. De nieuwe algoritmes vergelijken

kenmerken van de niet-lineaire relatie tussen de transmissie-amplitude en de belasting van het staal, met een drempelwaarde. Op deze manier wordt de toestand van het staal geëvalueerd. Tijdens de ontwikkeling van deze algoritmes gaat er extra aandacht uit naar de voorwaarden om een NDT techniek te kunnen implementeren in een praktische toepassing. De ontwikkelde toepassingen zijn bestand tegen veranderingen in het milieu en zijn gebaseerd op duurzame onderdelen, terwijl ze gevoelig zijn aan vibrerende defecten. De keuze van het diagnose-algoritme bij de monitoring van een bepaalde component is sterk afhankelijk van de component zelf en van de specifieke omstandigheden.

Table of contents

List of Symbols XII

List of Figures XV

List of Tables XXI

1. Introduction 1

1.1 Background and state of the art 1

1.1.1 Introduction to structural health monitoring 1

1.1.2 State of the art 4

1.2 Motivation and objectives of research 10

1.3 Outline of the dissertation 11

2. Theoretical background 13

2.1 Lamb modes 13

2.1.1 The elastic wave equation in a solid 13

2.1.2 Longitudinal and transversal waves 14

2.1.3 Displacement potentials 15

2.1.4 Construction of a Lamb mode basis in a plate 16

2.1.5 Lamb modes in layered systems 19

2.2 Mode conversion 21

3. Modulation of Lamb modes by a delamination 25

3.1 Introduction 25

3.2 Description of the structure and its properties 28

3.2.1 Physical properties 28

3.2.2 Influence of modulating d_{air} on the physical properties of the air layer 29

3.3 Lamb mode dispersion characteristics 34

3.3.1 Influence of the air layer compression on the Lamb modes of the system 35

3.3.2 Analytical study of the relation between effective coupling and air layer compression 42

3.4 Cross modulation due to delamination compression 47

3.5 Conclusions 53

4. Lamb waves optimised sensing systems 55

4.1 Introduction 55

4.2 Basics of piezoelectricity 57

4.3 Transducer arrays 60

4.3.1 Thick transducers 60

4.3.2 InSensor TF2100 piezoceramic array 63

4.4 Experimental implementation of Lamb mode selection 65

4.4.1 Wavelength selection 66

4.4.2 Velocity selection 71

4.4.3 Displacement symmetry-based selection 74

4.5 Conclusions 78

5. Crack detection in practice 81

5.1 Specific problem statement 81

5.2 Methodology 84

5.3 Quantification of mode-conversion at a modulated crack . . . 86

5.4 Experimental setup 92
5.5 Preliminary tests using Al plates 94
5.5.1 Sample geometry and typical course of the experiment 95
5.5.2 Processing of experimental results 100
5.5.3 Analysis of transmission under average and quasi-static load regimes 105
5.5.4 Amplitude modulation analysis 110
5.5.5 Concluding remarks on the experiments using an aluminium plate as sample. 116
5.6 Crack detection in an aluminium structure 116
5.6.1 Geometry of the sample and fatigue loading experiment 117
5.6.2 Steady state ultrasonic analysis 119
5.6.3 Nonlinear modulation based diagnostic algorithms . . 121
5.7 Automated defect detection algorithms 135

6. Conclusions 143

A. Displacement and stress inside a plate 149

B. Diagnostic algorithms applied on five samples 150

C. Lamb modes in triple layers 158

Bibliography 161

List of Symbols

Abbreviations

AD	Adiabatic
AISHA	Aircraft integrated structural health assessment
BC	Boundary conditions
CA	Correlation analysis
CAN	Contact acoustic non-linearity
CBCOA	Correlation of data below a cut-off load analysis
CWT	Continuous wavelet transform
GEIRA	General evolution of transmission amplitude measured in-rest analysis
GEHLA	General evolution of transmission amplitude measured at high load analysis
HF	High frequency
HTLA	High transmission load analysis
IT	Isothermal
LF	Low frequency
MCA	Modulation coefficient analysis
MCBCOA	Modulation coefficient for data below a cut-off load analysis
MDA	Modulation depth analysis
MTA	Median transmission analysis
NDT	Non-destructive testing
NI	Non-isolated
PZT	Lead zirconate titanate
SHM	Structural health monitoring
TOF	Time-of-flight
US	Ultrasonic

Roman symbols

A_i^j	amplitude of transmitted wave packet in data set j for measurement i
A_n	n^{th} asymmetric Lamb mode
C	compression factor
C_I^k	mode conversion coefficient from mode I into mode k
C_P	specific heat of a gas at constant-pressure
C_V	specific heat of a gas at constant volume
c	acoustic bulk velocity
c_L	longitudinal bulk velocity
c_T	transversal / shear bulk velocity
d	thickness, piezoelectric constant
E	electric field
f	frequency
(h × w × l)	height by width by length
i	imaginary unit
k	wavenumber
$\mathbf{k}$	wave vector
L	Lamb matrix, length
LM_n	n^{th} Lamb mode
Q	Mechanical quality factor
S_n	n^{th} symmetric Lamb mode
T	temperature, period
t	time
$\mathbf{u}$	displacement vector
u_d	scalar component of the displacement vector along the d-axis
V	volume
v	acoustic phase velocity
$\mathbf{x}$	spatial coordinates vector
x, y, z	scalar components of the spatial coordinates vector
Z	specific acoustic impedance

Greek symbols

α_T	transversal/shear wave attenuation coefficient
α_L	longitudinal wave attenuation coefficient
Γ	adaptation coefficient
γ	adiabatic gas constant
ϵ_{ij}	scalar value of strain tensor component ij
ε	electric permittivity
λ	wavelength
ρ	density
σ_{ij}	scalar value of stress tensor component ij
φ	irrotational scalar potential
$\boldsymbol{\psi}$	divergence-free vector potential
ω	angular frequency

List of Figures

2.1 Boundary conditions for Lamb waves in a plate surrounded by vacuum. 17

2.2 Dispersive Lamb modes of a 1 mm aluminium plate: wavenumber versus frequency-thickness product. 18

2.3 Grid plot of the displacement field of an A_0- and a S_0-mode wave packet. 19

2.4 Schematic of mode reflection at opened crack calculated with modal decomposition. 21

2.5 Real and imaginary modes at 600 kHz in a 1 mm thick aluminium plate. 23

3.1 Schematic overview of the modulation of a high frequency probe wave by a modulated air layer between a steel plate and an absorptive rubber layer. 28

3.2 Geometry of the modelled structure: a bilayer composed of steel and rubber with an air-filled delamination. 29

3.3 Compression dependence of the physical properties of the air layer for non-isolated, isolated isothermal, and isolated adiabatic modulation conditions. 33

3.4 Four dispersion curves of the phase velocity and the attenuation coefficient for three different models. 36

3.5 Attenuation of the LM_S mode for the triple layer in the NI model. 37

3.6 Dependence of the phase velocity and the attenuation of LM_{A_1} mode on the compression of the air layer for $f = 600$ kHz. 39

3.7 Dependence of the phase velocity and attenuation of the LM_S mode on the compression of the air layer for a probe wave frequency of 600 kHz. 40

3.8 Detailed view of the behaviour of the LM_S coupling frequencies as a function of the compression ratio for the three different thermodynamic models. 41

3.9 Dependence of numerically calculated LM_S cut-off frequencies, on the delamination layer compression ratio, together with the corresponding coupling frequencies, in the non-isolated model. 43

3.10 Effective impedance of the steel/rubber bilayer and of the air layer in the non-isolated case versus frequency. 46

3.11 Tangential evolutions of the normalised normal displacement magnitude at the free surfaces, for an incident LM_S mode, for different isolated and non-isolated air layer thicknesses and for the extreme cases of slip and stress-free boundary conditions. 48

3.12 Tangential profile of different harmonic components of the normal displacement pattern of a probing LM_S Lamb wave at the free steel and rubber interface for non-isolated air gap thicknesses between $d_{min} = 0.01\,\mu m$ and $d_{max} = 0.02\,\mu m$. . . 51

3.13 Tangential profile of different harmonic components (fundamental frequency (black line), first (red line) and third (green line) harmonics) of a probing LM_S Lamb mode at the free steel (bottom) and rubber (top) interface in the neighbourhood of an L=0.5 cm stress-free/perfect clapping delamination. 51

4.1 Transducer response for the combination of different Lamb modes and reflections. 56

4.2 The response of a piezoelectric material to a potential difference U_z over its top and bottom. 59

4.3 Signal response in a transmitter-receiver system of two PZT transducers. 61

4.4 Normalised amplitude of a wave packet measured by an individual element of the transducers array for two arrays based on PZT transducers of two different PZT element geometries. 62

4.5 Boundary conditions for an infinite transducer array. 63

4.6 Meggitt InSensor TF2100 transducer arrays on a 1 mm stainless steel plate. 64

4.7 Logarithmic intensities (a.u.) of the wavenumber - frequency spectrum for one element in a InSensor TF2100 piezoceramic array excited by a nanosecond pulse. 65

4.8 Normalised amplitude of a wave packet measured by individual elements of the InSensor TF2100 array. 65

4.9 Lamb wave dispersion curves of an aluminium plate. 67

4.10 Representation of mode selection in an array of 6 elements with a spacing corresponding to the wavelength of the A_0 mode. 67

4.11 Envelopes of transducer responses for different approaches of wavelength based mode selection. 70

4.12 Experimental results of velocity selection in an aluminium plate. 73

4.13 Placement of the transmitter transducer and the two receiver transducers on the sample 74

4.14 Experimental results for symmetry selection in an aluminium plate. 75

4.15 Simulated results for symmetry selection in an aluminium plate. 75

4.16 The displacement of PZT transducers near the top and on the bottom of a 1 mm aluminium plate for the S_0 and A_0 modes of a 600 kHz wave. 77

5.1 A slat track and its actual position and function in a wing. . 82

5.2 General concept of the developed crack detection method. . . 86

5.3 The evolution of a crack during one fatigue cycle. 87

5.4 Simulated transmitted energy fraction versus average crack size given for an incident Lamb mode of the S_0 or the A_0 mode for three types of defect symmetry in a 1 mm aluminium plate. 89

5.5 Transmitted energy of the S_0 and A_0 Lamb modes versus average crack size for a symmetric crack. 90

5.6 Simulated transmitted energy of the A_0 and S_0 mode versus average crack size, for the case of a symmetric crack in a fatigue loading experiment. 91

5.7 MTS-810 load bench, fitted with an aluminium plate. 93

5.8 Schematic overview of the latest setup. 94

5.9 Geometry of a 1 mm aluminium plate sample. 96

5.10 Crack length versus number of cycles. 97

5.11 Fatigue crack on the back side of a sample after $(79\pm2)\,10^3$ cycles. 98

5.12 Overlaid plot of the applied fatigue load versus phase of the fatigue loading cycle for 85 sets of 50 measurements. 99

5.13 Histograms of the load for all measurements and for a random set of 50 measurement. 100

5.14 Examples of transmitted probe waves and the applied time gate in an experiment with a 1 mm aluminium plate sample. 102

5.15 Schematic representation of the determination of a transmission quantifying parameter in time and frequency domain. . . 102

5.16 Relative difference between transmission amplitude calculated by different methods to the quantifier based on the peak amplitude (A) and the absolute values of the corresponding transmission amplitude. 104

5.17 Comparison between the transmission quantified as the peak intensity and quantified as the integral of the frequency spectrum. 104

5.18 Schematic overview of the signal processing from experiment to data set. 106

5.19 Normalised transmission amplitudes of the S_0-part in different load regimes versus fatigue loading time in a 1 mm aluminium plate 107

5.20 Ratio between the S_0 and A_0 transmission amplitudes for experimental and simulated data. 111

5.21 Peak amplitude versus time for the entire experiment; fatigue load, peak amplitude, and peak frequency versus phase of fatigue loading; and peak amplitude versus load for one fatigue cycle. 112

5.22 Transmission efficiency and corresponding amplitude modulation in a not vibrating 1 mm aluminium plate. Probe waves of variable excitation frequencies were transmitted between an actuator and a sensor. 115

5.23 Transmission versus measured frequency in one set of measurements of a fatigue loading experiment 115

5.24 Overlaid plot of the applied fatigue load versus phase of to the fatigue loading cycle for 212 sets of 50 measurements. . . 118

5.25 Examples of transmitted probe waves and the applied time gate in an experiment with a 6 mm aluminium bar with a 1 mm thick crack susceptible region region. 118

5.26 An intact 6 mm aluminium bar with a 1 mm thick crack susceptible region 118

5.27 Normalised transmission amplitudes of the S0-part in different load regimes versus fatigue loading time in a 6 mm aluminium bar with a 1 mm thick crack susceptible region . . 120

5.28 Fatigue load, transmission amplitude, and the peak frequency versus phase of fatigue loading and transmission amplitude versus load. 122

5.29 Combined transmission amplitude modulation by varying load. 124

5.30 Correlation between the transmission amplitude and the applied load versus time. 126

5.31 Modulation coefficient of the normalised transmission amplitudes as a function of applied load versus time. 128

5.32 Normalised transmission amplitude and corresponding modulation depth versus time. 130

5.33 Average load of the 5 highest transmission amplitudes. 132

5.34 Normalised transmission amplitudes, median of the normalised transmission amplitudes and the corresponding threshold. . . 133

5.35 The outcome of the different diagnostic algorithms for five different samples. To evaluate the state of the sample, the different defect development quantifiers were compared the corresponding threshold values, plots thereof are presented in appendix B. In the experiments with the 1 mm aluminium plate type samples the sensing system was affected by strong nonlinear modulation caused by fatigue loading. 140

A.1 Displacement and stress of the A_0 and the S_0 Lamb mode inside an solid plate. The length of the x-axis is equal to one wavelength and the length of the z-axis is equal to the plate thickness. The displacement and stress are normalised. The overlaying grid plots are an indicator of the direction and the amplitude is arbitrary. 149

B.1 Transmission amplitude at the minimum load in a fatigue cycle compared with its threshold value for all samples. . . . 151

B.2 Transmission amplitude at the maximum load in a fatigue cycle compared with its threshold value for all samples. . . . 152

B.3 Correlation analysis quantifier compared with its threshold value for all samples. 153

B.4 Modulation coefficient analysis quantifier compared with its threshold value for all samples. 154

B.5 Modulation depth analysis quantifier compared with its threshold value for all samples. 155

B.6 High transmission load analysis quantifier compared with its threshold value for all samples. 156

B.7 Median transmission analysis quantifier compared with its threshold value for all samples. 157

List of Tables

3.1 Physical properties of steel, air, and rubber at atmospheric conditions. 29

3.2 Fitted values of the proportionality coefficient a between the coupling and cut-off frequency for the non-isolated, the isothermal and the adiabatic case. 46

3.3 Acoustical impedance matching conditions for $f = 600$ kHz. . 50

4.1 Amplitudes of the S_0 and A_0 wave packets and their ratio for different types of detection and excitation using wavelength based mode selection. 70

4.2 Amplitudes of the S_0 and A_0 wave packets and their ratio for S_0 and A_0 detection, using velocity based mode selection. . . 73

5.1 Observed fatigue durations for 5%, 10% and 20% decrease in transmission quantifiers, for a 1 mm aluminium plate 107

5.2 Observed fatigue durations for 5%, 10% and 20% decrease in transmission quantifiers, for a 6 mm aluminium bar with a 1 mm thick crack susceptible region 120

5.3 Overview of the features of the different diagnostic algorithms. 142

Chapter 1

Introduction

1.1 Background and state of the art

1.1.1 Introduction to structural health monitoring

Structural health monitoring (SHM) is a protective measure, that is implemented in order to timely detect and halt deterioration of the state of materials or objects. It involves sensor networks for the application of damage detection and monitoring techniques into engineering structures. Damage comes along with changes of the material, of its geometric properties, of the boundary conditions, and to the structure connectivity, which deteriorates the structure's performance [1]. SHM is driven by a need for higher safety and increased efficiency. The application of damage detection implemented into critical structures, opens the door for improved component design and condition-based maintenance. The transition from planned maintenance to condition based-maintenance is one of the biggest achievements of SHM and has several advantages. It reduces down-time costs, decreases maintenance costs and improves reliability [2, 3]. Improvements in component design are mostly related to weight reduction, but by analysing data collected by SHM systems, other properties of the structure can be optimised as well. The main disadvantages of SHM implementation are the development cost, which are often increased by the need to develop and certify new electronics, and the need to check the SHM devices themselves.

Most SHM systems make use of one or more non-destructive testing (NDT) techniques. Often the SHM systems extend the scope of individual NDT techniques by implementing more elaborate ways of damage monitoring.

The development of a successful SHM technique depends on a number of 'winning factors'. Cheap, durable, and sturdy parts are preferred. To min-

imise training cost of the personnel operating these devices, clear and unambiguous read-out of the damage state and fast, cheap, and reliable inspection of the system should be achieved.

Historically two main fields of SHM applications exist: civil infrastructure and aerospace applications [4]. The term civil infrastructure groups all the physical and organisational structures and facilities needed for the operation of a society or enterprise [5]. Some examples are buildings, factories, tunnels, bridges, power plants, port facilities and petroleum installations. Aerospace applications include all type of airplanes, helicopters and other aircraft. The major difference between both fields lies in the (none-)uniqueness of the structure that is monitored. In the field of aerospace, mass produced parts are used and a normal or healthy-state baseline behaviour can be obtained by testing these parts. In civil infrastructures almost all systems are unique and SHM has to be oriented towards a long-term evaluation of what is 'normal' structural performance [6]. Nowadays the separation between both fields is being blurred by 'small' mass-produced civil infrastructures. These are mainly wind turbines, but pipe lines, chemical storage tanks, etc. as well. These structures are still relatively large in size, compared to aircraft components, and exhibit the same issues with sensing technologies as large civil structures. On the other hand, their components are often produced in similar quantities as components of large aircrafts and testing of baseline behaviour becomes feasible and more profitable. Development of health monitoring strategies can thus be done on the same fundamentals as for aerospace applications. In the context of the development of signal analysis and interpretation algorithms a classification into *'traditional' civil engineering applications*, considering individually designed structures, and *mass-produced applications* is more adequate.

In traditional civil engineering SHM occurs mostly on bridges and on dams. Expensive and elaborate systems are applied to monitor the state of several well-known long span bridges e.g. the Normandy Bridge (France) and the George Washington Bridge (NY, USA) [7]. The uniqueness, complexity and dimensions of long span bridges are limiting the applicability of SHM and oblige manual inspection and periodical large-scale inspections. On the other hand, SHM could play a more significant role on shorter bridges with less complex geometries and a more standard design. For specific bridge types, statistical sampling and clustering concepts could be applied. A SHM system that is closer related to those used in aircraft structures could be developed, allowing more cost effective and efficient maintenance of the public facilities [7]. Dams are a second field in civil engineering where SHM

plays an important role in the maintenance and monitoring schedule. Here again, first steps have been taken to evolve to a more general SHM system. The Italian electricity utility ENEL [8] monitors structural (displacements, strains, seepage rates) and environmental (water level, structural temperature, meteorological conditions) properties of the dams under their surveillance, using a number of different sensors. The data are analysed by a central monitoring system, allowing statistical analysis and the application of artificial intelligence to detect failures or unsafe behaviour [6]. Lower in number, but not in importance, are the SHM systems on nuclear power plants. Here again, SHM has numerous benefits while the site is in operation and is complemented by regular inspection techniques and non-destructive testing techniques during regular maintenance. The actuality and importance of these civil SHM applications is illustrated by the large number of articles that can be found on this topic [1, 2, 4, 6, 7, 9–16].

In aerospace applications, implementation of SHM systems could be very advantageous. Considering that aircrafts are built up of different parts, where some parts are more critical and others less, it is easier to take apart the SHM system and to focus on the SHM of a specific part [17]. There is a large number of parts that are systematically being monitored. Some parts (engine, flaps, steering system, etc.) are checked before every take off, while other parts (fuel lines, static wing parts, floor beams, helicopter tails, etc.) are checked on a time-based maintenance schedule. Moments of inspection of other mass-produced structures are for most cases entirely time based. The cost of unscheduled repairs is many times that of of regular maintenance. In particular when spare parts and man-hours are not readily available, as is often the case for remote wind turbines, this results in expensive down-time [2].

There is a general need for SHM in civil and mass-produced applications as almost all private and government industries want to detect damage at an early stage [13]. Often there is a certain damage tolerance which determines when a component has to be replaced and detection of damage before this critical size is reached is necessary. Reliable integrated damage detection by SHM can result in large economic advantages and increase potential life and environmental safety. Recent technological improvements in the field of lightweight (composite) materials have reduced the weight of numerous constructions and traditional materials in several non-critical components, especially but not exclusively in aeronautical applications, have been replaced by advanced lightweight alternatives [18]. In order to maintain this progress, structural components have to be reduced in weight, by changing

design and construction materials, without compromising the reliability of the application and while keeping safety an absolute priority. On the other hand, for economic reasons civil infrastructure and aerospace vehicles are being kept in operation for much longer times than originally designed. This results in accumulated damage due to ageing [19]. For these structures SHM is becoming increasingly important, while implementation of SHM during the production of new structures could reduce this problem in the future.

1.1.2 State of the art

Structural health monitoring has been studied for over thirty years and for several applications a damage detection or monitoring technique is available. As perviously mentioned most SHM methods are based on one or more non-destructive testing techniques to detect damage. The implemented NDT techniques can be considered as the beating heart of SHM. The difference between both is the extent of the SHM method. A NDT technique is considered to detect damage and, depending on the specific technique, provide information about the type, its geometry, its location, etc. An SHM method is considered to inspect for damage, monitor the evolution of the damage, and sometimes provide a prediction on the remainder of the lifetime of the component. Typically, it uses information provided by one or more NDT techniques, combined with (preprogrammed) knowledge of the component (previous state, geometry, reference measurements, etc.) and additional information from other sources (temperature, pressure, operational status, etc.). Consequently, the development of a SHM method is more application-specific than the development of a NDT technique. Most damage detecting and monitoring techniques described in literature are thus considered NDT due to their general applicability. The work presented in this dissertation is focussing on NDT applications, but with practical implementation in SHM methods in mind.

Common non-destructive testing techniques

A number of non-destructive testing techniques have been successfully implemented into SHM applications. In the following, the most common NDT techniques available for mass-produced applications and their main characteristics are briefly discussed. A detailed lecture on different NDT techniques can be found in 'Introduction to Nondestructive Testing: A Training Guide' by Paul E. Mix [11].

- Visual inspection: Inspection of the components by human eye. This is the oldest and most used NDT technique. It requires that the monitored component is accessible and clean. The sensitivity of visual inspection is limited to surface damage. During-operation, monitoring is often impossible. Several techniques were developed to increase the performance of visual inspection, including liquid penetrants and magnetic particles [11].

- Radiographic testing: Detection of damage by evaluating X-ray images of the inspected material is predominantly applied as quality test in production processes. The sensitivity of this technique in composite materials, which are typically low absorbers of X-rays, can be increased by introducing detectable penetrants [20]. Radiographic testing is successful to detect internal damage in production environments and for off-line detection.

- Eddy current inspection can be applied on electrically conducting materials by detecting variations in induced electrical currents in the tested component. This technique is widely used to detect near surface-cracks, delamination, and corrosion. Furthermore compact standalone detectors are commercially available. One option, is to scan the component with a probe, which requires accessibility of the structure and is often not feasible in operating conditions. Implementation of coils onto the structure offers a solution for on-line damage detection on small hotspots in simple geometries [21].

- Ultrasonic methods: Ultrasonic non-destructive testing (US-NDT) methods are based on the interaction of ultrasonic acoustic waves with defects [22]. Ultrasonic waves experience mode conversion when they enter a region with a different acoustic impedance, as in the case of a defect [23]. A typical setup consist of an actuator emitting ultrasonic waves into the component and a sensor detecting ultrasonic waves. In a conventional transmission setup, the transducers are placed on either side of the component and an anomalous loss of transmitted energy indicates a defect. Alternatively damage can be found in a pulse/echo mode by detection of unexpected reflections. US-NDT is widely applied in diverse conditions and different approaches and algorithms have been developed to estimate the size, location, orientation... of defects in the inner structure of solid components [24]. Embedding the sensing system into the component allows on-line detection. Other, non-embedded, ultrasonic techniques include acoustic

emission/resonance analysis, as well as grating-, thermal-, and speckle-interferometry.

- Thermal wave interferometry: Thermal waves penetrate the material and reflect at interfaces of different effusivities. Abnormal temperature differences, observed at the surface indicate the presence of a defect [25]. Continuous, modulated, and pulsed heating can be applied by natural heating, or external light-, electromagnetic-, or ultrasound-sources. More enhancements, such as lock-in thermography, are available and provide higher sensitivity than traditional thermography. In most thermography applications only the defects are visualised in final stage images, allowing detection in complex structures [25]. Thermography is very effective in internal damage detection on easily accessible components, but of limited use in confined spaces or during operation.

- Speckle interferometry: The difference between images of the component under different loads creates a fringe pattern. This pattern can be compared with a reference and the differences between both can be attributed to internal defects. As for thermography, speckle interferometry can be improved by using pulsed light sources, to improve the sensitivity and the signal-to-noise ratio [26]. Due to the need to illuminate the surface and install a camera, speckle interferometry is only suitable for off-line detection.

- Acoustic emission analysis: By 'listening' to sounds produced by a structure while under load, the initiation and propagation of defects can be observed. Historical examples of NDT by acoustic emission are procedures performed by pottery makers who understood the cracking sounds made by clay pots, that they were cooling down too quickly, or (Belgian) mineworkers being warned by the cracking noises of pine beams that a tunnel became unstable. In nowadays applications, sonic or ultrasonic acoustic emission of defect-related movements can be detected, such as snapping fibres, fibre pull-out, clapping of a delamination, dislocations moving through the material's crystal lattice structure,... This detection requires advanced noise reduction and detected signal discrimination. Additionally quantitative measurements of damage properties are unavailable. Although multiple successful implementations have been presented in recent literature [27], implementations in noisy and complex environments are still limited.

- Acoustic resonance analysis: In this approach, the investigated component is excited and the generated sound is compared with a (refer-

ence) recording of an undamaged component. Damage causes changes in the vibration modes and thus differences in resonance between both (reference and current) recordings are sought [28]. The sensitivity decreases with crack size and reference measurements are of utmost importance. On-line detection is possible when ambient excitation can be used. Acoustic resonance analysis has proven useful in several applications, e.g. detection of a loose bolt joint in an aluminium structure, damage detection in various materials including composites...

- Optical fibre monitoring: The transmission of light through a fibre depends on the internal strain. Changes in the properties (wavelength, polarisation) of a transmitted light source, indicate changed loads on the monitored component [29]. This method does not directly detect defects, but it can be used in SHM to provide additional information, e.g. when only a maximum load is allowed on a component.

- Implemented fuses: Optical fibres or electrical resistance wires can be implemented into laminated composites or placed on top of a structure [30, 31]. Breakage or reduced electrical conductance of the fibres indicates the presence of damage. On-line and off-line detection can be implemented to detect surface and internal damage.

All NDT techniques mentioned above have been studied thoroughly over the last decades and substantial enhancements were accomplished. Optical full field detection allows rapid quality assessment of surfaces during production and scheduled maintenance. Acoustic emission and resonance analysis have been implemented and proved their success. However, they are not applicable in complex noisy environments. Implemented crack detection with eddy currents or fibre-based methods is restricted to the direct vicinity of the sensors and can be difficult to incorporate inside solid components. Ultrasonic detection has excellent sensitivity to a wide range of damage, including damage inside solid components, and uses basic sensing technology. Hence, for on-line inspection of critical components, US-NDT is the most promising choice.

Linear ultrasonic non-destructive testing

To facilitate in-operation testing on components that are a part of a larger structure, the use of embedded sensors is necessary. In order to monitor larger areas, compared to the limited reach of early-age local bulk wave based ultrasonic techniques, guided waves are used. Rayleigh waves and

Lamb waves, both named after their discoverer, travel along elongated structures and can propagate over considerable distances. Rayleigh waves are confined to the surface of solid structures and penetrate for only one or two wavelengths. Therefore detection of cracks in solid objects, using Rayleigh waves, is only sensitive to surface cracks. Due to their limited penetration depth they are strongly attenuated by absorptive material, such as dirt or grease, on the surface. Consequently, the use of Rayleigh waves requires that the inspected surfaces are clean.

Lamb waves exist in plate-like structures and produce stresses over the entire plate thickness. They are dispersive and their properties depend on the elastic properties of the medium that guides them. (Theory on Lamb waves is explained in section 2.1.) In plate-like objects, Lamb waves are sensitive for different types of defects including delaminations, cracks, corrosion, etc.

Over the past decades numerous linear US-NDT techniques have been developed detecting the aforesaid types of open defects in a variety of components: solid [32–44] or composite [20, 24, 35, 45, 46, 46–51] plates, at rivets and joints [52–54], railway axles [55], pipes [56–59], helicopter rotors [60], wind turbine components [27, 61],...

The detection algorithms of different approaches vary substantially. One approach is to analyse the effects of mode conversion at the defect [62]. The easiest method is to analyse the total transmission and compare the results with a reference measurement of an intact sample. More advanced techniques use features of the mode conversion between the Lamb modes [37, 48]. Another widespread approach is based on time-of-flight (TOF) measurements, often using multiple transmitter or receiver transducers [32, 34–48, 50, 51, 63]. Probe wave packages of limited duration are excited and detected by different transducers. The received signal is decomposed into different wave packages, differentiating between a wave package that followed the direct trajectory, and reflections from the defect or boundaries. Using the positions of the transducers and the TOF of the different wave packages, the different sources (probe wave-transmitters or scatters such as defects and boundaries) of the wave packages are triangulated. Continuous wavelet transform [64] is the most common technique to process the wave packages and to calculate the TOF, but numerous alternatives are available.

The use of transducer arrays or networks does not only allow defect localisation but also mode-selective transmission and reception of Lamb waves becomes possible. The interaction of a Lamb-mode with a defect is strongly dependent on the type (mode symmetry, mode order) of mode on the probe frequency, and on the geometrical characteristics of the defect [62, 65]. Con-

sequently, the properties (transducer-design, -placement, -coupling, probe wave characteristics) of the sensing systems, which often make use of Lead Zirconate Titanate (PZT) transducers, play an important role in defect detection. Experimental and theoretical studies [66–73] emphasise the complex relation between the different variables, however illustrate the powerful possibilities of a dedicated sensor system.

In summary, modern linear US-NDT techniques provide mature solutions to detect different types of open defects, while providing additional information about the geometry and location. In contrast, in real life situations, in particular when not under load, defects can 'close' and return to a state of homogeneous surrounding. Linear US-NDT, but equally well other NDT techniques, are based on a detectable change of material conditions at the defect boundaries, which makes closed defects invisible for most NDT techniques, including conventional US-NDT.

Nonlinear ultrasonic testing

Techniques based on nonlinear ultrasonics were developed to resolve the problem of closed cracks. Acoustic nonlinearity arises when acoustic waves propagate through regions with wave dependent material parameters, such as nonlinear elastic properties or nonlinear effects at a defect. In general four types of nonlinear ultrasonic effects are used for defect detection. The most common form is detection of higher harmonics [74–89], these arise when a probe wave provokes a nonlinear elastic response of the medium, which, in turn, modulates the probe wave. The non-elastic response of the medium can arise from non-Hookean elasticity or from contact acoustic nonlinearity (CAN). Higher harmonic analysis is very sensitive to fatigue damage and allows the detection of early-stage crack formation, however it is very sensitive to other not-defect related inhomogeneities in the sample or in the sensing system. Sub-harmonic detection, where lower harmonics resulting from the vibration of the defect are analysed, is similar to higher harmonic detection, but it is only sensitive to closed cracks and thus more robust [86, 90]. Nonlinear resonant ultrasound spectroscopy measures changes in resonance frequency, due to nonlinear effects [91–93]. As previously discussed, it is not adequate for online monitoring in noisy environments. Amplitude modulation, the fourth nonlinear effect, is generated by dynamically opening and closing of a defect by vibrations in the sample. The corresponding changes in mode conversion at the defect result in a modulated transmission of the probe waves. Waves probing in an intact sample are not modulated. Detecting features induced by vibro-acoustic modulation reveal the presence

of a defect [93–97]. A detailed review on nonlinear techniques for non-destructive testing was published by K.-Y. Jhang [98], who focussed on the detection of micro damage.

Insight in the physics of nonlinear acoustic effects has been improved by numerous theoretical studies [23, 78, 79, 86, 93, 99–107], often combined with experimental verification. An excellent in-depth review on crack-wave interactions in solids by D. Broda et al. [108] concludes that multi-scale modelling is required since nonlinear effects vary depending on the length scale, multiple non-classical models couple strain and temperature fields and hence require multi-physical tools for numerical simulations, and multiple models are able to simulate the nonlinear effects during crack-wave interaction. Nonlinear interactions between delaminations and waves have also been studied as delaminations form a second common type of closed defects. Simulations of delaminations are often based on bi-linear stiffness. This approach assumes that modulated delaminations undergo clapping, opening when under tension and closing when compressed. Simulations of these effects have gradually improved over the last decade, coming from a basic prefect-coupling/no-contact model to models incorporating different types of layers and more realistic clapping behaviour [108].

1.2 Motivation and objectives of research

Despite the number of nonlinear detection methods available, practical SHM systems implemented in complex structures are still missing. One reason is that non-destructive inspection techniques which do not differentiate between nonlinear contributions coming from a targeted defect susceptible area and other locations, are not suitable for on-line detection. Mechanical contacts in vibrating/operational structures interact with probe waves, thereby making the signal response undistinguishable to the one of a crack. Localisation of defects combined with dedicated signal processing filtering out reflections can resolve this. A general problem of currently available NDT techniques is their sensitivity to environmental conditions of the monitored component. Due to changes in temperature, dirt buildup, or different operational conditions, severe changes in wave propagation and wave-defect interaction of a component can take place [94, 109, 110]. Interpretation algorithms based on calibration or reference measurements are heavily affected by environmental changes and ask for complex sensor calibration and alike measures [111]. Hence, defect detection and monitoring during operation using nonlinear ultrasonics requires dedicated sensing systems, signal

analysis and interpretation algorithms.

The general objective of this work is to develop an on-line non-destructive testing technique, based on nonlinear ultrasonics, to detect and locate cracks in a vibrating structure in operation. The focus is on the early detection of cracks in complex components of larger structures by ultrasonic monitoring during operation. When (HF) ultrasonic waves interact with defects that are modulated (at low frequencies) by large periodically varying mechanical loads, induced by the operating structure, they are dynamically opened. This results in nonlinear elastic behaviour of the cracks or delaminations and in detectable amplitude and phase cross-modulation of the probe waves. In this work, advanced probing, sensing, signal processing/analysis, and interpretation algorithms are developed to differentiate different sources of nonlinearity and provide early defect detection in a well demarcated area.

The individual objectives can be listed as follows:

- Development of a sensing system that allows to discriminate between defect-related nonlinearity and other sources of nonlinearity.
- Study of Lamb mode enhancement using phased array transducers to produce directed probe waves to allow development of mode-selective and location-selective diagnostic algorithms.
- Theoretical study of nonlinearity in vibrating structures to improve understanding of the underlying physics, necessary to develop delamination detection algorithms.
- Practical implementation of the sensing system into a laboratory setup capable of collecting data in an operational environment in order to test the real-world applicability and sensitivity of the sensing system and defect detection algorithm.
- Development of diagnostic algorithms with focus on unambiguous results, on-line applicability, and reference-free defect detection.

1.3 Outline of the dissertation

In Chapter 1 an introduction on structural health monitoring illuminates the role of non-destructive testing techniques. The review of the common NDT methods is focussing on recent nonlinear ultrasonic NDT techniques. In conclusion, the motivations and objectives of this work are outlined.

In Chapter 2 the necessary theoretical background of Lamb waves and mode conversion at interfaces is presented. The Lamb-matrix for a single layer is calculated and the solution is extended to a multi-layer system. The boundary conditions for different types of interfaces or cracks, which are necessary to calculate the effect of the interaction in terms of reflected and transmitted Lamb waves, are stated.

Delaminations represent an important class of defects, which can interact with ultrasonic probe waves. Mode conversion around an air-filled delamination in an absorptive bilayer is studied in Chapter 3. The influence of the thermodynamic properties of an air layer on the nonlinear interaction between Lamb waves and the delamination will be presented. The aim is to predict the probing conditions (probe wave frequency and degree of compression of the sample) at which the modulation of the probe waves by the vibrating delamination is optimum, and hence facilitate practical detection.

Due to the existence of Lamb waves propagation modes, probe waves often consist of multiple modes which can not be separated by a single sensor-transducer. Single mode transmission and detection by transducer arrays can provide an outcome. A number of approaches to mode selection are explored in Chapter 4.

In Chapter 5 crack detection in vibrating solid plate structures is developed and validated. In the first section (5.1), a detailed description of the specific circumstances in which the proposed NDT technique is expected to be applied, are provided. In the following two sections (5.2, 5.3), the methodology of the proposed NDT technique are be explained and illustrated by a simulation of the transmission of probe waves through a modulated crack. The objective is to detect cracks by analysis of the relation between the vibration of the inspected component and the nonlinear modulation of the transmission of probe waves through a defect region in the component. In section 5.4 and 5.5, experimental equipment and procedures to acquire experimental data are described, together with the results of preliminary tests on aluminium plates. In section 5.6, different diagnostic algorithms, using nonlinear features of the probe wave - crack interaction are proposed and validated. The performance of the different proposed diagnostic algorithms are compared and a conclusion of the experimental work is presented in section 5.7.

The major conclusions and a further outlook of this work are presented in Chapter 6.

Chapter 2

Theoretical background

In 1917 Sir H. Lamb examined the two dimensional problem of elastic waves confined in a plate. He calculated the displacement and stress equations for the most important modes of vibration of an infinite plane [112]. A brief recapitulation of his outstanding work is presented in this chapter, in order to illustrate how the displacements and stresses of Lamb modes can be calculated and how a Lamb mode basis for a plate-like structure can be constructed. Subsequently, a procedure to semi-analytically calculate the mode conversion between Lamb waves at an interface is explained. Mode conversion coefficients allow simulation of ultrasonic effects at crack interfaces and are used in Chapter 4 and Chapter 5.

2.1 Lamb modes

2.1.1 The elastic wave equation in a solid

Let $\mathbf{u}(\mathbf{x},t)$ be the displacement vector at time t of a point with three-dimensional coordinates $\mathbf{x} = (x, y, z) = (x_1, x_2, x_3)$ in an isotropic, continuous solid material. The displacements in the material are assumed to be relatively small, hence they fall in the restrictions of the linear theory of elasticity [113]. deformation in different directions can by described by the strain tensor ϵ [114]:

$$\epsilon_{ij} = \frac{1}{2}\left(\frac{\partial u_i}{\partial x_j} + \frac{\partial u_j}{\partial x_i}\right) \quad \text{with} \quad i, j = 1, 2, 3 \tag{2.1}$$

The linear relation between the stress and the strain tensor can be described using Hooke's law. For a linear elastic solid the stress tensor σ_{ij} is

$$\sigma_{ij} = \lambda\epsilon_{ij}\delta_{ij} + 2\mu\epsilon_{ij} \quad \text{with} \quad i, j = 1, 2, 3 \tag{2.2}$$

with λ and μ the Lamé constants and δ_{ij} Kronecker's delta.

The displacement equations of motion can be obtained using Newton's second law:

$$\mu \sum_j u_{i,jj} + (\lambda + \mu) \sum_j u_{j,ij} + \rho f_i = \rho \ddot{u}_i \tag{2.3}$$

with $u_{i,ij} = \frac{\partial^2 u_i}{\partial x_i \partial x_j}$,$\ddot{u}_i = \frac{\partial^2 u_i}{\partial t^2}$, ρ the density, and $f_i = f(x_i, t)$ the body force per unit mass working on this point. With the elastic displacement-equation of wave propagation in solids can be described.

2.1.2 Longitudinal and transversal waves

In vector notation the elastic displacement equation can be written as

$$\mu \nabla^2 \mathbf{u} + (\lambda + \mu) \nabla (\nabla \cdot \mathbf{u}) = \rho \ddot{\mathbf{u}} \tag{2.4}$$

A general solution to this differential equation is the harmonic wave:

$$\mathbf{u} = A \mathbf{P} e^{i(\omega t - \mathbf{k} \cdot \mathbf{x})} \tag{2.5}$$

with A the amplitude of the wave, $\mathbf{P}$ the (unity) polarisation vector, ω the angular frequency and $\mathbf{k}$ the wave vector, directed along the propagation direction. Substitution of the harmonic wave (2.5) solution in the displacement equation (2.4) yields

$$\rho \omega^2 \mathbf{P} = (\lambda + 2\mu) \mathbf{k} (\mathbf{k} \cdot \mathbf{P}) + \mu (\mathbf{k} \times (\mathbf{k} \times \mathbf{P})) \tag{2.6}$$

This equation satisfies the equation of motion if

$$\mathbf{k} \times \mathbf{P} = 0 \quad \text{and} \quad \mathbf{k} \cdot \mathbf{k} = \frac{\rho \omega^2}{\lambda + 2\mu} \tag{2.7}$$

or if

$$\mathbf{k} \cdot \mathbf{P} = 0 \quad \text{and} \quad \mathbf{k} \cdot \mathbf{k} = \frac{\rho \omega^2}{\lambda} \tag{2.8}$$

To meet the first condition (equation 2.7), the polarisation vector has to be parallel to the propagation direction. The resulting type of waves are called longitudinal waves or P-waves (pressure) and propagate with a longitudinal wave velocity c_L:

$$c_L = \sqrt{\frac{\lambda + 2\mu}{\rho}} \tag{2.9}$$

The second condition (equation 2.8) yields that the polarisation vector is perpendicular to the propagation direction, resulting in so-called transversal waves or S-waves (shear). The transversal wave velocity c_T is:

$$c_T = \sqrt{\frac{\lambda}{\rho}} \tag{2.10}$$

These two harmonic waves are unique solutions for the isotropic, homogeneous wave equation [114].

2.1.3 Displacement potentials

The system of equations given by the elastic displacement equation in (2.4) couples the three displacement components which is unpractical while evaluating its solutions in a confined medium. Expressing the components of the displacement vector in terms of potentials results in far more convenient expressions. A so-called Helmholtz decomposition has been suggested [114]:

$$\mathbf{u} = \nabla\varphi + \nabla \times \boldsymbol{\psi} \tag{2.11}$$

with

$$\nabla \cdot \boldsymbol{\psi} = 0 \tag{2.12}$$

According to the Helmholtz decomposition theorem, any well-behaved vector field can be decomposed into a sum of an irrotational scalar potential φ and a divergence-free vector potential $\boldsymbol{\psi}$ [115]. Substitution of the decomposed displacement vector into equation (2.4) results in two separate wave equations

$$\Delta\varphi = \frac{1}{c_L}\ddot{\varphi} \tag{2.13}$$

and

$$\Delta\boldsymbol{\psi} = \frac{1}{c_T}\ddot{\boldsymbol{\psi}} \tag{2.14}$$

Two independent relations result, the first one (2.13) is only related to the longitudinal waves, while the second potential (2.14) accounts for the transversal waves. This decomposition greatly simplifies the analysis of solutions for the elastic displacement equation (2.4).

2.1.4 Construction of a Lamb mode basis in a plate

Calculations are greatly simplified if plates are modelled as two-dimensional objects. For waves propagating in the x-direction, the physical quantities have no y-dependence and consequently displacements and stresses only have components in the x- and z-direction. Under this assumption, the vector $\boldsymbol{\psi}$ reduces to a one dimensional scalar, hence denoted by ψ. The decoupled wave equations (2.13) and (2.14) can be expressed as

$$\frac{\partial^2 \varphi}{\partial x^2} + \frac{\partial^2 \varphi}{\partial z^2} = \frac{1}{c_L^2} \frac{\partial^2 \varphi}{\partial t^2} \tag{2.15}$$

and

$$\frac{\partial^2 \psi}{\partial x^2} + \frac{\partial^2 \psi}{\partial z^2} = \frac{1}{c_T^2} \frac{\partial^2 \psi}{\partial t^2} \tag{2.16}$$

Standard solutions for φ and ψ are

$$\varphi = \varphi_1 \, e^{-p_L z} e^{ikx - iwt} + \varphi_2 \, e^{p_L z} e^{ikx - iwt} \tag{2.17}$$

$$\psi = \psi_1 \, e^{-p_T z} e^{ikx - iwt} + \psi_2 \, e^{p_T z} e^{ikx - iwt} \tag{2.18}$$

with $p_{L,T}^2 = k^2 - \omega^2 / c_{L,T}^2$ and φ_1, φ_2, ψ_1, and ψ_2 integration constants which have to be determined by the boundary conditions.

With the solutions of the potentials φ and ψ the displacements can be calculated using equation 2.11. This gives:

$$u_x = \frac{\partial \varphi}{\partial x} - \frac{\partial \psi}{\partial z} \tag{2.19}$$

$$u_z = \frac{\partial \varphi}{\partial z} + \frac{\partial \psi}{\partial x} \tag{2.20}$$

With these expression the stress in the different directions, given in equation 2.2 can can be calculated:

$$\begin{aligned}
\sigma_{xx} &= \rho c_L^2 \left(\frac{\partial^2 \varphi}{\partial x^2} + \frac{\partial^2 \varphi}{\partial z^2} \right) - 2\rho c_T^2 \left(\frac{\partial^2 \varphi}{\partial z^2} - \frac{\partial^2 \psi}{\partial x \partial z} \right) \\
\sigma_{zz} &= \rho c_L^2 \left(\frac{\partial^2 \varphi}{\partial x^2} + \frac{\partial^2 \varphi}{\partial z^2} \right) - 2\rho c_T^2 \left(\frac{\partial^2 \varphi}{\partial x^2} - \frac{\partial^2 \psi}{\partial x \partial z} \right) \\
\sigma_{xz} &= \rho c_T^2 \left(\frac{\partial^2 \psi}{\partial x^2} + 2 \frac{\partial^2 \varphi}{\partial x \partial z} - \frac{\partial^2 \psi}{\partial z^2} \right)
\end{aligned} \tag{2.21}$$

The boundary conditions (BC) in a plate of infinite length along the x-direction are illustrated in Figure 2.1. The plate consists of a solid homogeneous material surrounded by vacuum. It has thickness d and stress-free

interfaces at $z = 0$ and $z = d$:

Stress-free BC at the top surface ($z = 0$) : (2.22)

$$\begin{cases} \sigma_{xz} = 0 \\ \sigma_{zz} = 0 \end{cases}$$

Stress-free BC at the bottom surface ($z = d$) : (2.23)

$$\begin{cases} \sigma_{xz} = 0 \\ \sigma_{zz} = 0 \end{cases} \quad (2.24)$$

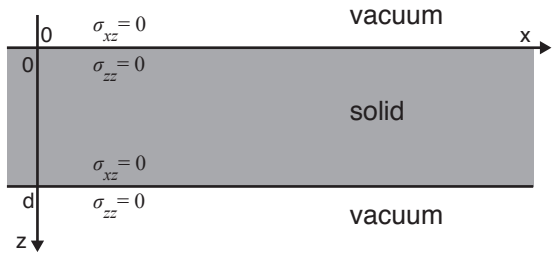

Figure 2.1 Boundary conditions for Lamb waves in a plate surrounded by vacuum.

The boundary equations are applied on the general solutions for φ and ψ (equations 2.13 and 2.14):

$$L \cdot \begin{pmatrix} \varphi_1 \\ \varphi_2 \\ \psi_1 \\ \psi_2 \end{pmatrix} = 0 \quad (2.25)$$

with the Lamb matrix L:

$$L = \begin{pmatrix} k^2 + p_T^2 & k^2 + p_T^2 & -2ikp_T & 2ikp_T \\ -2ikp_L & 2ikp_L & -k^2 - p_T^2 & -k^2 - p_T^2 \\ \left(k^2 + p_T^2\right) e^{-p_L L} & \left(k^2 + p_T^2\right) e^{p_L d} & -2ikp_T e^{-p_T L} & 2ikp_T e^{p_T L} \\ -2ikp_L e^{-p_L L} & 2ikp_L e^{p_L L} & -\left(k^2 + p_T^2\right) e^{-p_T L} & -\left(k^2 + p_T^2\right) e^{p_T L} \end{pmatrix} \quad (2.26)$$

The integration constants φ_1, φ_2, ψ_1, and ψ_2 must be linear in order for the solutions φ and ψ to be general. This requires that the determinant of the Lamb matrix is zero:

$$|L(k, \omega)| = 0 \quad (2.27)$$

Equation 2.27 is a non-analytical equation describing the relation between the wave vector k and the angular frequency ω. Numerically solving equation (2.27) yields that the Lamb wave phase velocity $v = \omega/k$ is frequency dependent and thus dispersive. Curves showing the relation between the different parameters depending on ω, such as wavenumber k, wavelength λ, phase velocity v, and group velocity are referred to as dispersion curves. In Figure 2.2 the 'first' five dispersion curves of the wavenumber k as a function of the frequency-thickness product $f\,d$ are shown. Lamb modes can be classified in symmetric and anti-symmetric modes, based on their symmetry with respect to the central horizontal axis of the plate. The corresponding particle motion of a S_0- and an A_0-mode wave (multiplied with a Gaussian window) is illustrated in Figure 2.3. (In appendix A detailed plots of the displacement and stress of the A_0 and S_0 modes in a plate are presented.) The A_0 and S_0 modes are the only modes starting at $f = 0$, higher modes start at a fixed frequency, called the cut-off frequency. The dispersion curves of Lamb waves are scalable for the frequency-thickness relation, which was used on the x-axis in Figure 2.2. This means that if a mode with wavenumber k is found for a given f_1 and d_1, the same mode with wavenumber k is found for any frequency f and plate thickness d of which the product is equal to $(f_1 \cdot d_1)$.

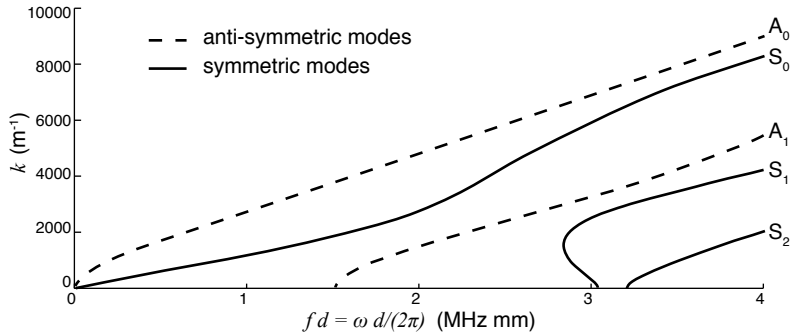

Figure 2.2 Dispersive Lamb modes of a 1 mm aluminium plate: wavenumber versus frequency-thickness product.

The basis of solutions of the wave-equations does not only consist of real solutions for k and also complex wave numbers exist. Purely imaginary wavenumbers exist only locally as they do not propagate and quickly attenuate. For inhomogeneous modes the imaginary part of the wave number defines the attenuation of the wave. In absorbing materials, where longitudinal and transversal velocities have a non-zero imaginary component, decaying modes that propagate over longer distances are found instead of

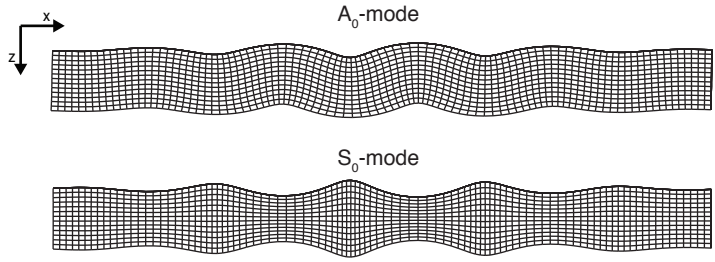

Figure 2.3 Grid plot of the displacement field of an A_0- and a S_0-mode wave packet.

infinitely running modes. The dispersion curves of these absorbing materials can be depicted in two subfigures: one giving a real property, for example phase velocity or wavelength, and a second plot showing the corresponding attenuation.

2.1.5 Lamb modes in layered systems

The calculation of Lamb modes in plates consisting of multiple layers is very similar to the problem in a single plate. The proposed standard solutions in equations 2.17 and 2.18 can be expanded to a set of $2 \times n$ solutions, with n the number of layers, to provide two displacement potentials for every layer l:

$$\begin{aligned} \varphi_l &= \varphi_{1,l}\, e^{-p_{L,l}z} e^{ikx-iwt} + \varphi_{2,l}\, e^{p_{L,l}z} e^{ikx-iwt} \\ \psi_l &= \psi_{1,l}\, e^{-p_{T,l}z} e^{ikx-iwt} + \psi_{2,l}\, e^{p_{T,l}z} e^{ikx-iwt} \qquad (2.28) \\ &\quad \text{for } l = 1, 2, ..., n \qquad (2.29) \end{aligned}$$

The subscript l denotes to which layer the variable corresponds, hence $4 \times n$ unknown integration constants are sought. The thickness of each layer is given by d_l and the top coordinate of the multilayer is set at $z = 0$, therefore the bottom is at $z = \sum_l d_l$. The top and bottom surface are again expected to be in contact with vacuum and hence stress-free conditions apply. Boundary conditions can be implied on the interfaces between the different layers. At these interfaces two types of boundary conditions on stress and displacement can typically be assumed. Perfect-coupling boundary conditions, which normally apply in bonded layers, demand continuity of stress σ_{zz} and σ_{xz} and of the displacement vectors u_x and u_z. Slip boundary conditions simulate conditions in which mechanical contact between two

layers is lost for tangential stresses and displacements, hence the stress vector σ_{xz} is zero (stress-free), the stress vector σ_{zz} is continuous while only the displacements u_z are matched.

For a triple layer surrounded by vacuum with slip boundary conditions at the first interface and perfect-coupling boundary conditions at the second interface the boundary conditions look as follows:

Stress-free BC at the top surface ($z = 0$) :

$$\begin{cases} \sigma_{xz,1} = 0 \\ \sigma_{zz,1} = 0 \end{cases}$$

Slip BC at interface 1 ($z = d_1$) :

$$\begin{cases} \sigma_{xz,1} = 0 \\ 0 = \sigma_{xz,2} \\ \sigma_{zz,1} = \sigma_{zz,2} \\ u_{z,1} = u_{z,2} \end{cases}$$

Perfect-coupling BC at interface 2 ($z = d_1 + d_2$) :

$$\begin{cases} \sigma_{xz,2} = \sigma_{xz,3} \\ \sigma_{zz,2} = \sigma_{zz,3} \\ u_{x,2} = u_{x,3} \\ u_{z,2} = u_{z,3} \end{cases}$$

Stress-free BC at the bottom surface ($z = d_1 + d_2 + d_3$) :

$$\begin{cases} \sigma_{xz,3} = 0 \\ \sigma_{zz,3} = 0 \end{cases}$$

Substituting the proposed solutions for the six displacement potentials into these 12 boundary conditions yields a 12×12 Lamb matrix equation analog to the one in equations 2.25 and 2.26. Again general solutions of the displacement potentials can only be found if the determinant of the Lamb matrix is zero.

The calculation of displacement and stress fields of Lamb modes in a triple layer structure is described in detail in Appendix C. In the presented structure the middle layer is considered to be shear-free. These calculations were used to obtain the results presented in section 3.4.

2.2 Mode conversion

Mode conversion takes place at any point where wave propagation properties change. This can be at a crack, a slit, a delamination,... In the following, in order to calculate the mode conversion coefficients, a modal decomposition method is applied as described by Castaings et al. in *Modal decomposition method for modelling the interaction of Lamb waves with cracks* [23]. Modal decomposition is based on the mathematical principle that any allowed wave in a medium can be constructed by a linear sum of the elements of the wave basis. To simplify matters, mode conversion is typically calculated for a single, monochromatic incoming Lamb mode and linear acoustic defect-wave interaction for a given state of the defect is assumed. First a Lamb mode basis for this frequency can be constructed for both sides of the interface. (Refer to sections 2.1.4 and 2.1.5 for this procedure.) This basis consists of a finite number of modes with real (not attenuating modes) and purely imaginary wavenumbers (non-propagating modes) and an infinite number complex wavenumbers (inhomogeneous modes). A sufficiently large basis of modes is necessary for boundary conditions to be satisfied. Next, the boundary conditions at the interface have to be defined. In the following, two cases of interfaces are given and the details of the boundary conditions are presented.

Boundary conditions at a vertical crack

In the considered two dimensional case vertical cracks lay along the z-direction, horizontal defects are considered in the following section. To simplify matters, the crack is modelled as a part of the material with stress-free boundary conditions for displacement and stress in the x-direction. The geometry of such a crack is shown in Figure 2.4

The boundary conditions for a crack starting at the top surface and with

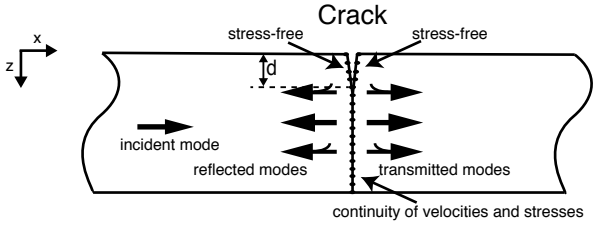

Figure 2.4 Schematic of mode reflection at opened crack calculated with modal decomposition. (Source figure: [23].)

depth d are as follows:

Stress-free BC inside the crack ($z < d$) :

$$\begin{cases} a_I \sigma_{ij,k_I} + \sum_{-k} b_{-k} \sigma_{ij,-k} = 0 & \text{for } ij = xx, xz \\ 0 = \sum_{k} b_k \sigma_{ij,k} & \text{for } ij = xx, xz \end{cases}$$

Perfect-coupling BC outside the crack ($z \geq 0$) :

$$\begin{cases} a_I \sigma_{ij,k_I} + \sum_{-k} b_{-k} \sigma_{ij,-k} = \sum_{k} b_k \sigma_{ij,k} & \text{for } ij = xx, xz, zz \\ a_I u_{i,k_I} + \sum_{-k} b_{-k} u_{i,-k} = \sum_{k} b_k u_{i,k} & \text{for } i = x, z \end{cases} \tag{2.30}$$

where k and $-k$ denote modes of respectively right and left traveling modes, a_I and k_I denote the amplitude and mode of the incident mode, and b_i denotes the unknown complex amplitude that have to be found.

Boundary conditions between different media

When mode conversion takes place at the interface between two perfectly coupled media, then different Lamb mode bases apply. Typical examples are a horizontal defect modelled with slip boundary conditions or the transition from one material to another.

Since perfect coupling in the x-direction is assumed the boundary conditions are simple:

Perfect coupling BC:

$$\begin{cases} a_I \sigma_{ij,k_{1I}} + \sum_{-k_1} b_{-k_1} \sigma_{ij,-k_1} = \sum_{k_2} b_{k_2} \sigma_{ij,k_2} & \text{for } ij = xx, xz, zz \\ a_I u_{i,k_{1I}} + \sum_{-k_1} b_{-k_1} u_{i,-k_1} = \sum_{k_2} b_{k_2} u_{i,k_2} & \text{for } i = x, z \end{cases} \tag{2.31}$$

with a_I and k_{1I} characterising the incident wave; and k_1 and k_2 the modes corresponding to respectively medium 1 and medium 2, where a negative k denotes a left traveling mode. The boundary conditions state that stresses and displacements should be continuous across the interface between the two media.

Calculation of mode conversion coefficients

In order to numerically calculate the mode conversion coefficients, the necessary Lamb bases should be constructed, containing a sufficient amount of

inhomogeneous Lamb modes. The number of necessary Lamb modes depends on the specific system. For a fixed frequency a limited number of real modes and purely imaginary modes exist and they should all be included. An infinite amount of complex modes can be found. The first modes found at 600 kHz in a 1 mm aluminium plate are depicted in Figure 2.5. In general the use of around 20 to 30 complex modes shows to be sufficient.

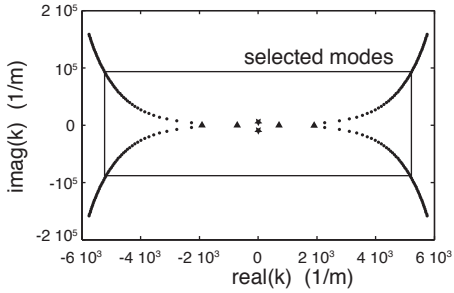

Figure 2.5 Real and imaginary modes at 600 kHz in a 1 mm thick aluminium plate. In most simulations, a Lamb mode basis of 20 to 30 modes is sufficient. The ▲ represent real modes, the ★ represent purely imaginary modes.

The interface of the plate is considered at a selected set of points along the interface, indicated by dots in Figure 2.4. The number of points should be larger then the number of modes in the Lamb basis in order to obtain an overdetermined system. The stress and displacement at every point are calculated for all modes of the Lamb basis and the corresponding boundary conditions are applied. This gives an overdetermined system of equations, which can e.g. be solved by singular value decomposition [23, 89, 116]. This results in a vector which consist of conversion coefficients b_k. The energy e of a normalised mode, i.e. with amplitude 1, can be calculated by

$$e = \int_0^{d_{total}} (\sigma_{xz} u_z^* + \sigma_{xx} u_x^* - \sigma_{xz}^* u_z - \sigma_{xx}^* u_x)\, \mathrm{d}z \tag{2.32}$$

with d_{total} the total depth of structure. The mode conversion coefficient C_I^k is defined as the ratio of the not-normalised energy of mode k ($|E_k|$) and the not-normalised energy of the incident mode k_I ($|E_I|$):

$$C_I^k = \frac{|E_k|}{|E_I|} = \frac{|b_k|^2}{|a_I|^2} \frac{|e_k|}{|e_I|} \tag{2.33}$$

This process can be applied to any kind of incident mode.

As a measure to verify the quality of the mode conversion coefficients, the boundary conditions and conservation of energy can be checked. When these are not satisfied, a number of adaptations can be made. The number of included modes can be increased or decreased, the wavenumbers can be calculated more precise, or the number of points in the discretisation can be changed. Using a different, more advanced, method to solve the overdetermined sample could be anther option to obtain qualitative mode conversion coefficients.

The mode conversion coefficients used in Chapter 3 and Chapter 5 were calculated following this procedure.

Chapter 3

Modulation of Lamb modes by an air-filled delamination

3.1 Introduction

Delaminations form an important class of defects in materials and devices. They are likely to grow in mechanically strained or chemically hostile structures, and the resulting deterioration of the structural strength finally leads to global malfunctioning or even failure. Therefore, understanding their nature and being able to detect their presence in a non-destructive way are of great interest in the field of quality control and safety preservation. Ultrasonic testing is an excellent non-destructive testing (NDT) technique for delamination detection and investigation. Ultrasonic waves can probe both surface and bulk regions in a material and they are sensitive to any kind of usually significant defect-induced acoustic impedance mismatch. In particular the interaction of Lamb modes in plate-like samples with different kinds of defects including delaminations has already been extensively studied [23, 99–105]. B. A. Auld and M. Tan [99, 100] predicted the reflection of Lamb modes from vertical delaminations normal to plate surfaces and this effect was revisited by many authors (see e.g. references [23, 104, 105]). S. Rokhlin studied Lamb mode diffraction on horizontal delaminations situated exactly in the middle of the plate [101–103].

Horizontal delaminations typically appear in composite layered plates where the existence of stresses or chemical degradation could lead to a deterioration of the coupling between layers and thus to the development of delaminations. Also, the effect of mode conversion by a horizontal delamination in absorbing bilayers was theoretically studied and it was shown that depending on the delamination length a considerable part of an incident Lamb

mode energy is converted into transmitted Lamb modes [117]. The spatial evolution of the normal displacement amplitude of a Lamb wave at the plate interfaces, a quantity which can typically be easily assessed in practical situations [118, 119], was theoretically analysed for plates coated with highly absorptive materials [120]. Both stress-free and slip delaminations (mechanical contact between slip delamination surfaces is only lost for tangential displacement components) were taken into consideration and it was shown that both types of delaminations could be detected for different types of incident modes. In practice, such measurements could provide information about the presence of delaminations and allow characterising their nature, which is important for non-destructive testing of composite materials.

In a typical ultrasonic test setup, probe waves are sent through the region of interest, and the transmitted or reflected waves, whose spectral and temporal features are affected by defects, are analysed and interpreted. An important disadvantage of this approach is that not only acoustic impedance changes due to defects are influencing the probe signal, but also acoustic impedance changes due to structural features (material edges, steps, connections, etc.), which makes it difficult to distinguish harmful defect-induced features from harmless structure-induced features.

In the framework of NDT it is desirable that defects induce a different probe signal signature. In the case of cracks and delaminations this can be achieved by exploiting the fact that acoustic waves of a moderate to high power can considerably modulate the crack or delamination width, leading to the so-called 'clapping' effect. The accompanying time dependent wave induced response of the material via the dynamically changing boundary conditions then leads to nonlinear acoustic effects [121], higher harmonic generation and cross-modulation between pump and probe frequencies. Since the nonlinear effect is exclusively and locally induced by the defect, it offers an interesting possibility for the detection of defects with high spatial resolution and contrast [86, 87, 122–124]. The propagation of a high frequency probing Lamb mode through an initially either open [89] or closed [116] delamination whose width was modulated by a low frequency pump Lamb mode was analysed using a quasi-stationary approach. In those works, the delamination was suggested to be internally empty when the boundary conditions at open delamination surfaces are stress-free. It was shown that the spectrum of the transmitted probing Lamb mode includes the fundamental probing frequency as well as considerable cross-modulation induced sum and difference combinations between the probing frequency

and modulating frequency and its harmonics. Cross-modulation harmonics were found to be strongly localised in the delamination region for an absorptive bilayer.

Considerable modulation of the transmitted probing Lamb mode spectrum is caused by the clapping effect [89, 116], leading to a significant modulation of the boundary conditions between delamination surfaces, and thus of their effect on the probing wave velocity, damping and mode conversion.

Real life delaminations are typically filled with a gas or a liquid, which is compressed and expanded as the pump wave or vibration is closing or opening the delamination width. In this work, we investigate how and to what extent the elastic response of the air layer is playing a role in the modulation of the delamination gap width, in the resulting modulation of the probe wave velocity and damping, and in the associated modulation of mode conversion coefficients. Inspired by practical situations of rubber layer protected steel pipelines and containers, containing possible delaminations between the rubber and steel layer, a three-layer model system consisting of a steel/air/rubber-structure, in which the steel plate (negligible wave damping) and rubber slab (high wave damping) are separated by an air layer with modulated thickness, is considered.

Figure 3.1 summarises the key features of the nonlinear interaction between a high frequency probe wave and a low frequency thickness-modulated air-filled layer in a steel plate covered by an absorptive layer. A low frequency pump wave (1) periodically compresses and expands the air layer, modulating its thickness (d_{air}). The attenuation and velocity of the probe wave (4) propagating along the steel side of the triple-layer structure depend on the degree of mechanical coupling between the steel layer and the highly damping rubber layer, and thus on the thickness and stiffness of the air layer. Due to the compression dependent probe wave attenuation (2), modulation of the compression leads to modulation of the amplitude and phase of the propagating probe wave (5) trespassing the delaminated zone.

The attenuation of the probing wave, and therefore the modulation depth of the nonlinear modulation of the probe wave, is not only depending on the air layer compression, but it also strongly depends on the probe wave frequency. In section 3.3.1 the frequency dependent Lamb mode dispersion curves of the triple layer are numerically calculated for different air layer thicknesses. The key properties of the different Lamb modes are compared and illustrated. Arguments are given why the LM_S-Lamb mode – which is a Lamb mode in the steel/air/rubber system, roughly following the dispersion curve of the S_0 mode in the bare steel layer – is the most suitable mode to detect

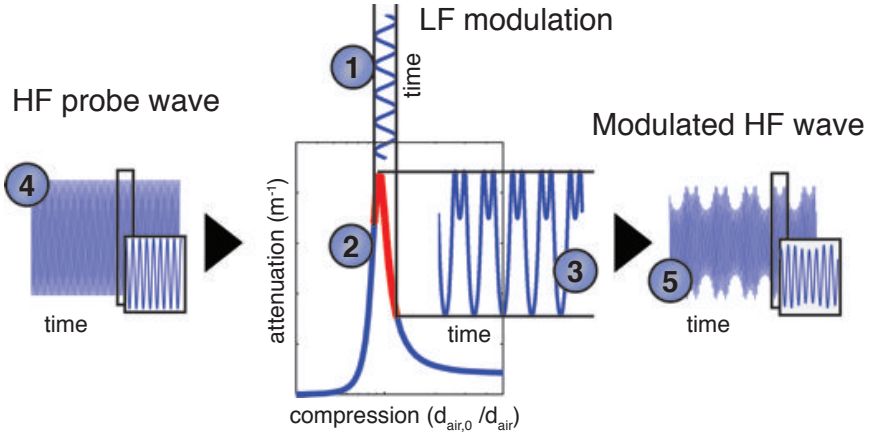

Figure 3.1 Schematic overview of the modulation of a high frequency (HF) probe wave by a modulated air layer between a steel plate and an absorptive rubber layer. (1), (2), and (3) depict how low frequency (LF) modulation of the air layer is transformed in a modulated attenuation of the incoming probe wave (4) resulting in a modulated transmitted wave (5) leaving the delaminated area.

modulated delaminations. In section 3.3.2, a general expression is sought to predict the sensitivity of the probe waves to the modulation of the delamination. An analytical estimate of the optimum modulation parameters is sought, with the goal to circumvent the calculation intensive determination of dispersion curves. It is investigated how acoustical impedance-like properties of the entire structure are linked to those of the air layer. Finally, the obtained expression is compared with the numerical results. In section 3.4 specific examples of the cross modulation of probe waves by a compressed air filled delamination are calculated using a quasi-stationary approach and the results are compared with a clapping delamination.

3.2 Description of the structure and its properties

3.2.1 Physical properties

The geometry of the considered rubber-coated (0.5 mm) steel plate (0.5 mm) structure is illustrated in Figure 3.2. An incident Lamb wave propagates along the y-direction in an isotropic bilayer of steel and rubber. The outer

surfaces are considered stress-free. Outside the delamination region the steel and rubber form two parallel layers with thicknesses d_{st} and d_r, and are in perfect mechanical contact (i.e. all displacement components and normal and shear stress are continuous everywhere at the interface). Inside the delamination region ($0 < y < L$) the air layer separates the steel and rubber layer. The steel and rubber layer are modelled as if they were pushed outward by the air layer without altering of their physical properties. Air was considered to have zero viscosity, resulting in the absence of shear coupling between the layers of the delamination. The shear wave attenuation coefficient of rubber ($\alpha_{T,r}$) is chosen so that the wave would propagate about one wavelength. Table 3.1 presents all relevant physical properties of steel, rubber and air.

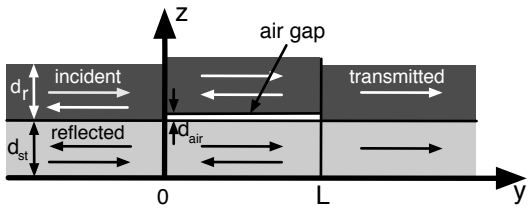

Figure 3.2 Geometry of the modelled structure: a bilayer composed of steel and rubber with an air-filled delamination.

Layer	Steel	Rubber	Air
d (m)	$0.5\ 10^{-3}$	$0.5\ 10^{-3}$	d_{air}
c_L ($\mathrm{m\,s^{-1}}$)	5720	1800	340
α_L ($\mathrm{m^{-1}}$)	-	230	-
c_T ($\mathrm{m\,s^{-1}}$)	3160	200	-
α_T ($\mathrm{m^{-1}}$)	-	$1/\lambda_{T,r}$	-
ρ ($\mathrm{kg\,m^{-3}}$)	7800	1100	1.3

Table 3.1 Physical properties at atmospheric conditions. $\alpha_{T,r} = f/c_{T,r} = 1/\lambda_{T,r}$ where $\lambda_{T,r}$ is the wavelength of a shear wave in rubber.

3.2.2 Influence of modulating d_{air} on the physical properties of the air layer

Introducing large varying mechanical stresses on the structure described in the previous paragraph (3.2.1), modulates the delamination, resulting in compression or expansion of the air layer. Before the behaviour of the triple layer can be modelled, the effects of thickness modulation of the air layer on its physical properties need to be defined.

We first consider the relaxed state (from hereon suffix '0') of the air layer in the delamination, in which all properties are equal to the properties of air at atmospheric pressure (e.g. $\rho_{air,0}$) (Table 3.1) and room temperature. In practice the thickness of the air-gap in the relaxed state ($d_{air,0}$) depends on how the delamination was formed. For the remainder of this thesis, this thickness ($d_{air,0}$) is always assumed to be 1 µm. For modelling cross-modulation, the actual air gap thickness is influenced by the modulating pump wave, corresponding to a non-unity compression factor

$$C = \frac{d_{air,0}}{d_{air}} \tag{3.1}$$

The elastic behaviour of the air gap, and therefore of the whole plate, not only depends on the geometrical gap thickness as such, but also on the corresponding thermodynamic state of compression. We consider three different thermodynamic scenarios.

In the first, 'non-isolated' case (NI), the air layer is not isolated from the surrounding atmosphere. This case mimics a system where air in the gap can 'instantaneously' escape to the outside fluid when the rubber and steel layer are compressed, or flow in during expansion, e.g. through a perforation of the rubber layer. This condition can be translated to the acoustic wavelength associated with the pressure changes being longer than the distances of locations in the air gap to the nearest opening. In the case of air gaps in crack openings in components subject to loads induced by motion in vehicles, the bandwidth of the modulations is typically limited to frequencies below 100 Hz. The corresponding wavelengths in air are of about c_L/f=340/100=3.4 m. The pressure equilibration within the air gap can thus be considered as quasi instantaneous. This implies that the only obstacle to pressure equilibration is the rate of pressure transfer through the narrowest channel on the way between the inside of the air gap and the outer world. With the Hagen-Poiseuille equation [125]:

$$r^4 = \frac{8\mu d_{layer}\Delta Q}{\pi \Delta P} \tag{3.2}$$

an estimate of the radius of the exit channel can be made. The length of the channel d_{layer} is assumed to be 1 mm, the modulation frequency $f = 100$ Hz, the dynamic viscosity of air $\mu = 0.2\ 10^{-2}$ cP, and the maximum allowed pressure difference between inside and outside $\Delta P = 1$ Pa. With these parameters, all the air within a delamination with an air layer thickness of 1 µm and a surface of 1 cm^2 can escape in time, when the exit channel has a radius r of more than 0.15 mm. When the radius of the exit channel is

smaller, the pressure difference increases dramatically, and the assumption of atmospheric pressure becomes invalid. When the conditions for a non-isolated air gap are fulfilled, the relaxed air gap thickness equals the effective thickness, $d_{air,0} = d_{air}$, at all times, and by the given definitions of $d_{air,0}$ and C (Expression 3.1), the compression factor is always unity: $C = 1$. However, to simplify comparison between the non-isolated case and the other thermodynamical models, $d_{air,0} = 1\,\mu\text{m}$ is interpreted as an initial state. When discussing the non-isolated state, term compression does not refer to the actual compression – which is always 1 – but to the ratio between the initial air layer thickness $d_{air,0}$ and the actual air layer thickness d_{air}. Hence, C is calculated by expression 3.1, with $d_{air,0}$ equal to the initial thickness.

One can also envisage a scenario in which the air layer is isolated from the surrounding, then the compressibility of the air depends on the degree of heat transfer between the compressed/expanded air and the material forming the air gap. The distance over which the temperature can be equilibrated on the time scale of the pressure modulations is given by the thermal diffusion length, which for sinusoidal modulations equals $\sqrt{\alpha/(\pi f)}$, with $\alpha = 2\ 10^{-5}\ \text{m}^2\,\text{s}^{-1}$ the thermal diffusivity of air. For 100 Hz modulations, the thermal diffusion length is of the order of 250 microns. The temperature in the air gap can thus be considered to be uniform at all times. However, there is a large the thermal impedance (i.e. thermal effusivity) mismatch between the different layers. Due to this large thermal effusivity mismatch can be expected that the efficiency of heat transfer between the air gap and its surroundings is rather poor. Nevertheless, the case for efficient heat transfer, leading to an isothermal system, and the case of inefficient heat transfer, leading to adiabatic conditions, are considered in this work.

When the air layer is isolated from the surrounding atmosphere while the physical properties behave isothermally, e.g. in case when the compression induced heat has sufficient time to dissipate during a compression-expansion modulation cycle of the delamination. The longitudinal velocity of waves in the air gap in this 'isolated isothermal' case (IT) in an ideal gas approximation is given by [126]

$$c_{air} = \sqrt{\gamma R T_{air}/M}, \tag{3.3}$$

where T_{air} is the air temperature in Kelvin, R is the molar gas constant, M is the gas molar mass and $\gamma = C_P/C_V$, the adiabatic gas constant, is the ratio between the specific heats of the gas at constant-pressure and at constant volume, roughly 7/5 for air at room temperature [127]. Neglecting

the weak temperature dependence of γ, the speed of sound in air for the isothermal case can thus be assumed constant:

$$c_{air}^{IT} = \text{CST} \tag{3.4}$$

However, contrary to the open air-gap (NI), the air density (ρ_{air}) does change depending on d_{air} according to:

$$\rho_{air}^{IT} = \rho_{air,0} \frac{d_{air,0}}{d_{air}} = \rho_{air,0} C. \tag{3.5}$$

In a third, 'isolated adiabatic' scenario (AD), the air layer is isolated from the environment both in terms of mass flow and heat flow. Heat flow can be neglected in cases where the compression rate of the delaminated area is higher while the rate of heat diffusion to the surroundings is low. In this case both the air density and air velocity vary with changing compression. Approximating air again as an ideal gas, temperature (T_{air}) and volume (V_{air}) are related as follows

$$T_{air} V_{air}^{\gamma-1} = \text{CST}. \tag{3.6}$$

As in the isothermal case, the air density is given by

$$\rho_{air}^{AD} = \rho_{air,0} C, \tag{3.7}$$

while the velocity was obtained combining (3.3) and (3.6)

$$c_{air}^{AD} = c_{air,0} (d_{air,0}/d_{air})^{\frac{\gamma-1}{2}} = c_{air,0} C^{\frac{\gamma-1}{2}}. \tag{3.8}$$

The dependences of the air density, longitudinal wave velocity, temperature and acoustical impedance are depicted in Figure 3.3. For the non-isolated case the parameters are invariant under compression. In the isothermal case the density changes with varying compression, while the longitudinal wave velocity remains constant. As a result, the acoustic impedance is compression dependent. In the adiabatic scenario all three critical quantities depend on the thickness of the air layer. Consequently, the air layer behaves different, when out of the relaxed state, depending on the air tightness of the gap and on the rate of heat transfer to the surroundings.

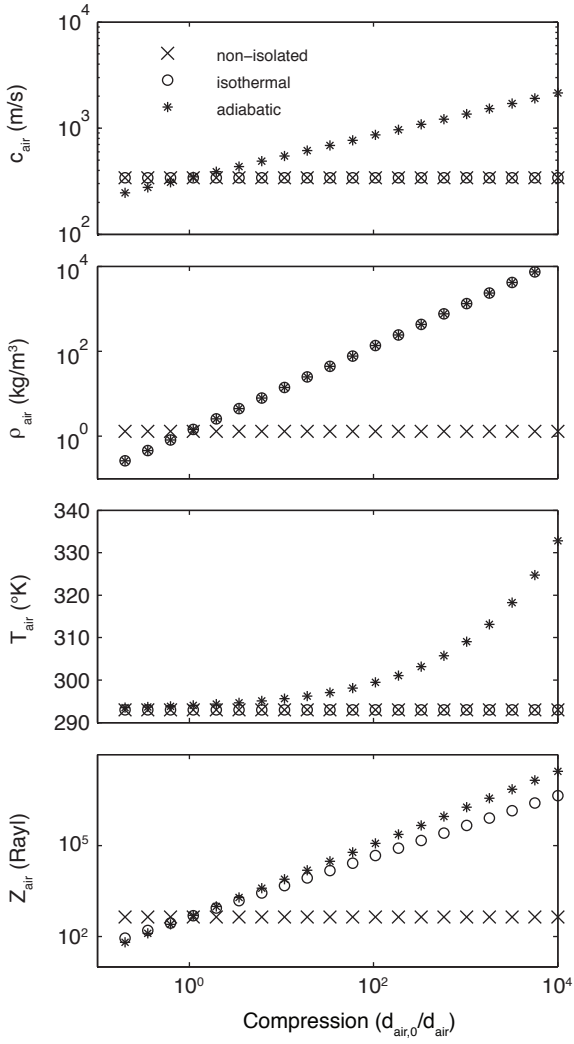

Figure 3.3 Compression dependence of, from top to bottom, longitudinal wave velocity, density, temperature, and acoustic bulk impedance in the air layer for non-isolated, isolated isothermal, and isolated adiabatic modulation conditions.

3.3 Lamb mode dispersion characteristics in an absorptive bilayer plate structure containing a delamination layer

The main application of non-destructive testing targeted by this thesis concerns the control of the quality of the mechanical contact between a chemically protective rubber layer and a steel plate, an assembly that is often used in pipelines and containers containing chemically corrosive liquids. Delaminations between rubber and steel are known to rapidly lead to leaks in the rubber, and soon after chemical corrosion of the steel around. The propagation of Lamb waves excited and detected at the outside surface of the steel plate is strongly dependent on the mechanical contact between the steel and the rubber. Essentially, the better the contact, the more the damping character of rubber induces Lamb wave attenuation. Inversely, the lack of mechanical contact induced by a growing delamination can lead to a reduction of the attenuation. The mechanical contact quality is known to also strongly affect the Lamb wave velocity, and, in case of a local delamination, the transmission, reflection, and conversion of a probing Lamb wave trespassing the transition between an intact region and a delaminated region. Due to their wavelength typically being comparable with the thickness of the plates, Lamb waves are highly dispersive, and their attenuation and velocity depend in a quite complex and frequency dependent way on the delamination properties. Since the rubber/steel-contact also affects the coupling between different modes of propagation, decreased mechanical contact between rubber and steel can in some cases even lead to an increase of attenuation of some wave modes. In view of the strong frequency dependence of the coupling strength, and thus of the Lamb wave propagation characteristics, it is worth to look for optimum probing frequencies in terms of sensitivity of the coupling to changes in the delamination air-gap thickness/compression. In the following, by studying the frequency dependence of the velocity and attenuation of different Lamb wave modes, we tackle this challenge, taking into account that the (coupling) response of the delamination air gap to pump wave induced compression depends not only on the air gap thickness, but also on the thermodynamic nature (non-isolated NI, isolated isothermal IT, isolated adiabatic AD) of the compression scenario, which affects the mechanical impedance of the air in the gap. In section 3.3.1, we investigate the dependence of the velocity and attenuation of Lamb modes in a steel/air gap/rubber plate on the state of compression of the air gap having an uncompressed thickness of 1 micron. In section 3.3.2

we interpret the found dependences with focus on particular frequencies, where the sensitivity of the propagation features to the state of the air gap is maximum. In part 3.4 we implement the found relation between the air gap state and the propagation parameters to model the modulation of the mode conversion coefficients of a high frequency probe wave encountering a transition between an intact and a delaminated region, whose state of compression is quasi-uniformly modulated by a low frequency pump wave.

3.3.1 Influence of the air layer compression on the Lamb modes of the system

In view of finding the Lamb wave modes and frequencies with a high sensitivity to modulations of the air gap thickness, in the following, we have calculated the Lamb mode dispersion curves for different air gap thicknesses, typically starting from a 1 micron gap in rest, and taking into account that the compressibility of the air gap depends on the compression scenario (air-gap isolated or not from the environment/isothermic or adiabatic compression).

The dispersion curves were found by a numerical search for solutions of the Lamb equations in a 3-layer model steel/air/rubber surrounded by vacuum, for frequencies between 10 kHz and 3 MHz and geometry and material parameters of the structure are described in section 3.2.1.

Figure 3.4 depicts the effect of the presence of a delamination on Lamb wave dispersion curves, in a delaminated region containing a non-isolated air layer of five nanometer thickness. An air layer of five nanometer is representative for a triple layer with an intermediate air layer thickness, it does not behave as the slip-boundary limit (dashed in Figure 3.4), nor does it behave as separated layers limit. Wave propagation in the case of separated layers is only effective in the non-absorptive steel layer (circles in Figure 3.4). Four main Lamb modes can be distinguished in the delamination and in the slip-boundary model: the LM_{A_1} and LM_{A_2} mode, whose velocities partially follow the A_0 mode that would propagate in a half a millimeter thick free standing steel plate, and the LM_S mode, which follows quite well the corresponding S_0 mode in the steel.

In the parts of the spectrum where the mode velocities LM_{A_1}, LM_{A_2} and LM_{A_3} are close to the ones of the A_0 mode in a steel plate, their attenuation is low. In this regime the energy of the waves is mostly confined within the steel plates [120]. In the frequency ranges where the LM_A steel modes diverge from the A_0 mode of steel, the steel dominated wave strongly couples

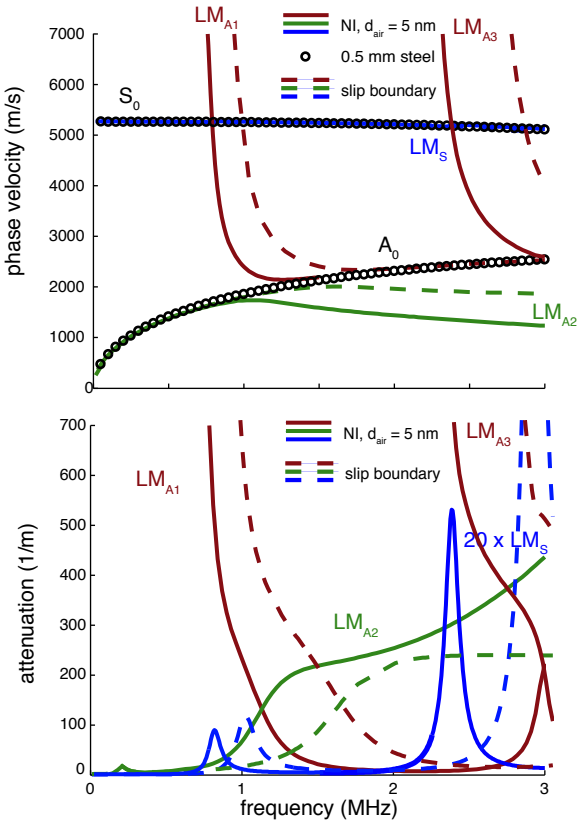

Figure 3.4 Four dispersion curves of the phase velocity and the attenuation coefficient for three different models. Solid: steel/air/rubber with 5 nm delamination; dashed: steel/rubber with slip boundary conditions; circles: 0.5 mm steel plate. (The attenuation of the LM_S modes has been multiplied with a factor 20.)

to the rubber. As a result, the velocities of the LM_{A_1}, LM_{A_2} and LM_{A_3} strongly diverge from the steel A_0 curve, and their attenuations sharply increase. A small change in frequency can in these cases induce a transition from steel-borne-like propagation to a highly attenuated regime or vice versa. It can be expected that in those frequency ranges the attenuation of the mode propagation is also highly sensitive to the quality of the mechanical contact between rubber and steel, and thus to the delamination. The attenuation of the LM_S mode shows two sharp peaks in the depicted frequency range. The peaks indicate an enhanced coupling between the steel and the rubber layer, leading to increased absorption. The peak at 0.8 MHz reflects coupling with the LM_{A_1} mode, and the peak at 2.5 MHz with the LM_{A_3} mode. Note that in Figure 3.4 the attenuation of the LM_S mode has been multiplied with a factor 20. At its local maximum around 0.8 MHz, the LM_S attenuation is around 125 times smaller than the attenuation of the LM_{A_1} at the same frequency. We have verified that a decrease in the thickness of the air layer shifts the dispersion curves to higher frequencies until the limit of the slip boundary case is reached. Also, the attenuation peaks of the LM_S mode shift until a limit is reached, as given in Figure 3.5. An increasing thickness shifts the curves down, where eventually the LM_{A_2} mode disappears and the LM_{A_1} mode mimics the A_0 mode of free steel, until it reaches the LM_{A_3} mode. From that point on the LM_{A_2} and LM_{A_3} relate as the LM_{A_1} and LM_{A_2} did, and the whole process repeats itself. The LM_S mode reaches a limit for the frequency of its attenuation peaks while the attenuation of these peaks go to zero.

To further study the effect of the air layer properties on the coupling between the steel and rubber layer, and thus to assess the feasibility of exploiting Lamb wave velocity and attenuation probing to get information on the de-

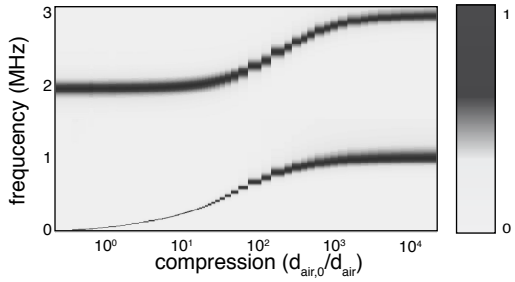

Figure 3.5 Attenuation of the LM_S mode for the triple layer in the NI model normalised to the attenuation peak in their range (below or above 1.5 MHz), with $d_{air,0} = 1\,\mu\text{m}$.

lamination, dispersion curves were calculated for a wide range of different air layer thicknesses for the three main modes (LM_{A_1}, LM_{A_2}, LM_S) and the three thermodynamic scenarios (NI, IT, AD). Figure 3.5 shows the normalised attenuation of the LM_S mode for the triple layer under non-isolated conditions. The figure reflects the two sharp attenuation peaks found earlier in Figure 3.4 and illustrates that these peaks show dispersive behaviour. The corresponding phase velocities approach the values of the S_0 mode in steel with a small change around the attenuation peaks, as was depicted for a single compression value in Figure 3.4. Naturally the change in phase velocity mimics the attenuation peak for changing compression. The LM_{A_1} and LM_{A_2} modes show similar dispersive behaviour as could be expected from Figure 3.4. For these modes the attenuation or phase velocity goes from a region of high values to a region of low values with a convergence line very similar to the line of attenuation peaks of the LM_S mode. To get a detailed understanding of the relation between the air layer thickness and the attenuation and phase velocity, results for a fixed frequency and as function of the air layer thickness are given. Combining the results for fixed frequency with the results for fixed air layer thickness (Figure 3.4) provides good insight in how changes in frequency and thickness influence the probe waves. Figures 3.6 and 3.7 illustrate the behaviour of the LM_{A_1} and LM_S modes for a fixed frequency. For this example, a frequency of 600 kHz was chosen since it is an intermediate case (Figure 3.5), this frequency was also used in the examples in section 3.4.

At low compression levels the attenuation of the LM_{A_1} mode, in Figure 3.6, is very low. The attenuation drastically increases at compression levels around 10 for an airtight air gap under adiabatic (AD) and isotropic (IS) conditions. When the air gap is open (NI) the attenuation only starts to increase for compression levels exceeding a factor of around 100. Along with the attenuation, the phase velocity sharply increases from $1532\,\mathrm{m\,s^{-1}}$ (the phase velocity of the bare steel plate for 600 kHz) to above $10\,000\,\mathrm{m\,s^{-1}}$. Once the compression is high enough to induce mechanical coupling between the steel and rubber layers, both the attenuation and phase velocity saturate at high levels. The difference in compression range where the transition between low and high attenuation or the attenuation peak takes place results from the difference in stiffness of the air layer coupling the steel and rubber for the different models, combined with the effect of the thicker air layer compared to the wavelength. A more detailed description of the dependence of the LM_S mode on the thermodynamic conditions and the size of the delamination is given in section 3.3.2.

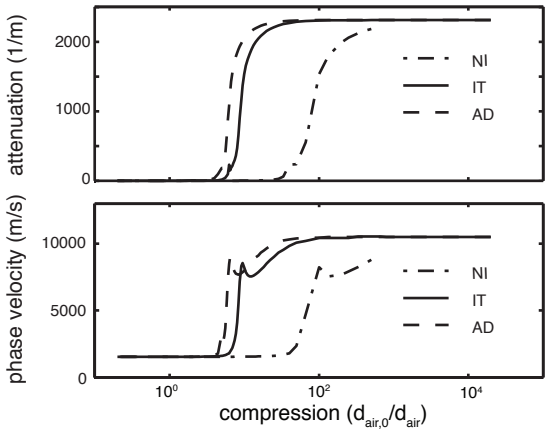

Figure 3.6 Dependence of the phase velocity and the attenuation of LM_{A_1} mode on the compression of the air layer (1 µm thickness in uncompressed conditions) for $f = 600$ kHz, in three scenarios: for an airtight delamination zone in isothermal (IT) and adiabatic (AD) conditions, and for a not-isolated delamination layer (NI).

We have verified that the attenuation and phase velocity of the LM_{A_2} modes behave as a mirror images of the LM_{A_1} mode, which is in correspondence with the observations made from Figure 3.4. For increasing compression, they tend to the values of the A_0 mode in bare steel (low absorption and phase velocity around $1532\,\mathrm{m\,s^{-1}}$). When a probe wave enters the delamination, then dynamic changes of compression across the transition region lead to large changes in acoustic impedance mismatch between the intact and delaminated zone, resulting in strongly modulated mode conversion coefficients of the LM_{A_1} and the LM_{A_2} modes, suggesting favourable possibilities for exploitation for detection the delamination.

The LM_S mode, depicted in Figure 3.7 for a probe wave frequency of 600 kHz, behaves differently. For most frequencies, a sharp deviation from the 'steel-confined' regime to a regime of increased attenuation takes place in a narrow compression range. Exceptions are the high and low compression limits of the attenuation peak frequency. At these frequencies the LM_S modes undergo a conversion from a low to a high attenuation regime (cfr. Figure 3.5). For 600 kHz the LM_S mode shows a sharp peak in its attenuation curve. Around this peak the phase velocity slightly changes.

Using the knowledge of phase velocity and attenuation at 600 kHz as a function of the compression ratio, it is possible to determine which order of modulation of the compression has to be applied to a delamination of a

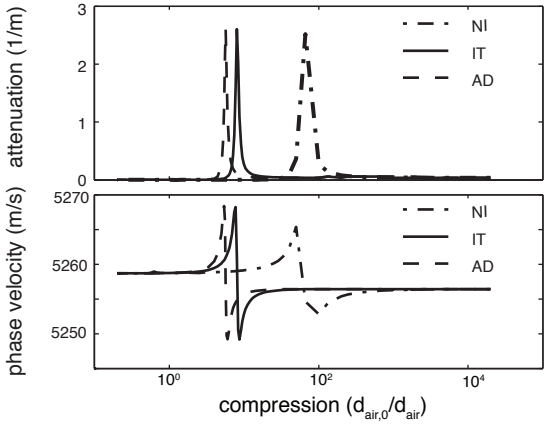

Figure 3.7 Dependence of the phase velocity and attenuation of the LM_S mode on the compression of the air layer (1 µm thickness in uncompressed conditions) for a probe wave frequency of 600 kHz, in three scenarios: for an airtight delamination zone in isothermal (IT) and adiabatic (AD) conditions, and for a not-isolated delamination layer (NI).

given size, to induce and optimise cross-modulation using a 600 kHz probe wave. Similar dispersion curves were numerically obtained for frequencies up to 3 MHz. This process was very computationally demanding and a number of key features of the dispersion curves would be sufficient to indicate the suitable compression range. The most straightforward candidates are the peak frequencies of the attenuation of the LM_S modes. Another potential candidate would be the steep increase of the phase velocity of the LM_{A_1} mode for increasing compression. However, the attenuation of the LM_{A_1} mode in an intact rubber/steel structure is rather high, more than 500 m^{-1} at frequencies below 1 MHz. In this frequency range, the rubber layer would absorb the probe waves in a matter of centimeters, making it impossible to inspect larger surfaces for defects. The LM_{A_2} mode has the same disadvantage as the LM_{A_1} mode. Therefore, the LM_S mode can be considered the optimum choice for cross-modulation based defect detection in the given system.

Figure 3.8 depicts the behaviour of the attenuation peaks of the LM_S modes in detail. The two lowest frequencies at which the coupling between the steel plate and the rubber layer is most efficient (from hereon called coupling frequencies: f_{coupl})(left) as well as the peak attenuation values are shown (right). Due to the damping of rubber increasing with frequency, the peak

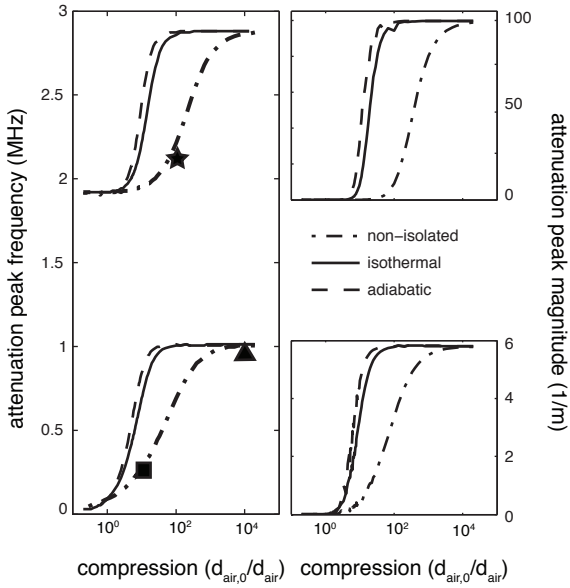

Figure 3.8 Detailed view of the behaviour of the LM_S coupling frequencies as a function of the compression ratio for the three different thermodynamic models. Left: attenuation peak frequencies. Top right: magnitude of the attenuation peak for $f_{coupling} > 1.5$ MHz. Bottom right: magnitude of the attenuation peak for $f_{coupling} < 1.5$ MHz. The air layer thickness was assumed to be 1 µm in rest. The symbols ■ ▲ ★ are analytically predicted cut-off frequencies corresponding with Figure 3.10.

attenuation also increases with increasing coupling frequency.

In earlier work [120], C. Glorieux and G. Shkerdin compared the dispersion curves of a non-absorptive rubber steel bilayer with those of an absorptive rubber steel bilayer. The introduction of finite absorption in rubber turned out to have a significant influence on the wave propagation behaviour around the cut-off frequencies. Cut-off frequencies are the frequencies where the wavenumber becomes zero and thus the phase velocity and the wavelength become infinite. The cut-off frequency and mode-repulsion effects of the rubber-like modes on the A_0 and S_0 steel-like modes are smoothed out and moderate absorption in the steel-like modes is introduced. The attenuation peaks of the LM_S mode follow this behaviour for the presented triple layer configuration. Moderate absorption is found and a strong relation of the coupling frequencies to the cut-off frequencies of a non-absorptive steel/air/rubber triple layer can be expected. Since cut-off frequencies do not exist in an absorptive structure, like in Ref. [120], we have calculated the cut-off frequencies by neglecting the absorptive properties of the triple layer, by using the real components of the longitudinal and transversal velocity of rubber. Searching for the roots of the determinant of the Lamb equation matrix for wavenumber $k = 0$ yields the cut-off frequencies. The results for a steel/air/rubber system with a non-isolated air layer are shown in Figure 3.9.

A number of compression-independent cut-off frequencies (horizontal light blue curves) were found. They correspond to the cut-off frequencies of the shear modes in a free rubber layer and, starting around 3 MHz, in a free steel plate. In addition, two dispersive branches of cut-off frequencies were found. These turn out to follow the behaviour of the coupling frequencies (black dots in Figure 3.9), except for a factor close to one, which can be attributed to the absence of attenuation assumed in the calculation of the cut-off frequencies.

3.3.2 Analytical study of the relation between effective coupling and air layer compression

The detection of delaminations by monitoring compression induced modulations of a probe wave passing along them can be optimised by looking for the conditions in which the probe wave attenuation has maximum sensitivity to variations of the delamination air gap thickness. This sensitivity goes along with the sensitivity of the coupling frequency to those variations. As the compression dependence of the coupling frequencies turns out to be very

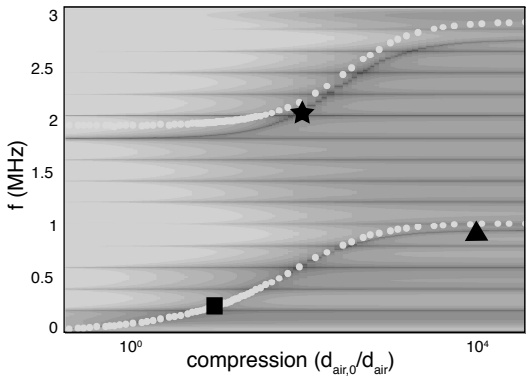

Figure 3.9 Dependence of numerically calculated LM_S cut-off frequencies (light blue constant and sigmoidal curves), on the delamination layer compression ratio, together with the corresponding coupling frequencies (black dots), in the non-isolated model, for $d_{air,0} = 1\,\mu\text{m}$. The symbols ■ ▲ ★ are analytically predicted cut-off frequencies corresponding with Figure 3.10.

similar to the one of the cut-off frequencies, in the following, an analytical study of the dependence of the cut-off frequencies on the air gap parameters is done, with the aim of getting more insight in the underlying physics.

The cut-off frequencies ($f_{c,T,L}$) of the transversal (T) and longitudinal (L) waves were calculated for the non-absorbing steel/air/rubber structure described in section 3.2.1. Since the air layer does not support shear stress, the cut-off frequencies of the shear waves only depend on the steel and rubber layer, not on the air gap parameters. They are easily found by calculating the transverse resonances (in the z-direction) of the transversal waves in the free-standing rubber and steel layer, and are given by

$$f_{c,T} = \frac{c_{T,layer}}{2d_{layer}} N \tag{3.9}$$

with $N \in \mathbb{N}^*$, $c_{T,layer}$ the shear wave velocity of the layer and d_{layer} the thickness of the layer. These cut-off frequencies correspond with the horizontal lines in Figure 3.9.

The dependence of the longitudinal cut-off frequencies on the air layer thickness can be obtained by looking for zeroes of the Lamb determinant, with

the wavenumber k set equal to zero [120]:

$$\begin{aligned} 0 &= \rho_{st} c_{L,st} \tan \frac{2\pi f_{c,L} d_{st}}{c_{L,st}} \\ &+ \rho_{air} c_{air} \tan \frac{2\pi f_{c,L} d_{air}}{c_{air}} \\ &+ \rho_r c_{L,r} \tan \frac{2\pi f_{c,L} d_r}{c_{L,r}} \\ &- \frac{\rho_{st} c_{L,st} \rho_r c_{L,r}}{\rho_{air} c_{air}} \tan \frac{2\pi f_{c,L} d_{st}}{c_{L,st}} \tan \frac{2\pi f_{c,L} d_{air}}{c_{air}} \tan \frac{2\pi f_{c,L} d_r}{c_{L,r}} \end{aligned} \tag{3.10}$$

with d_{st}, d_{air}, and d_r the thickness of the steel, air, and rubber layer, and $c_{L,st}$, c_{air}, and $c_{L,r}$ the longitudinal wave velocities of steel, air, and rubber. As each of the terms in this equations has the dimension of a specific acoustic impedance Z, we introduce the following effective impedances:

$$Z'_{L,st} = \rho_{st} c_{L,st} \tan \tfrac{2\pi f_{c,L} d_{st}}{c_{L,st}} = Z_{L,st} \tan \tfrac{2\pi d_{st}}{\lambda_{L,st}} \tag{3.11}$$

$$Z'_{air} = \rho_{air} c_{air} / \tan \tfrac{2\pi f_{c,L} d_{air}}{c_{air}} = Z_{air} / \tan \tfrac{2\pi d_{air}}{\lambda_{air}} \tag{3.12}$$

$$Z'_{L,r} = \rho_r c_{L,r} \tan \tfrac{2\pi f_{c,L} d_r}{c_{L,r}} = Z_{L,r} \tan \tfrac{2\pi d_r}{\lambda_{L,r}} \tag{3.13}$$

where $Z'_{L,st}$, Z'_{air}, and $Z'_{L,r}$ are effective impedances of the respective layers and $\lambda_{L,st}$, λ_{air}, and $\lambda_{L,r}$ the wavelengths of the longitudinal waves in steel, air, and rubber, respectively. Introducing these substitutions in Expression 3.10 yields

$$Z'_{L,st} + Z_{air} \tan \frac{2\pi d_{air}}{\lambda_{air}} + Z'_{L,r} - \frac{Z'_{L,st} Z'_{L,r}}{Z'_{air}} = 0. \tag{3.14}$$

Reordering of this expression gives:

$$\frac{Z_{air} \tan \frac{2\pi d_{air}}{\lambda_{air}}}{Z'_{L,st} Z'_{L,r}} + \frac{1}{Z'_{L,st}} + \frac{1}{Z'_{L,r}} = \frac{1}{Z'_{air}}. \tag{3.15}$$

For small air layer thicknesses:

$$Z_{air} \tan(2\pi d_{air}/\lambda_{air}) \ll \min(Z'_{L,st}, Z'_{L,r}),$$

so that the first term of Expression 3.15 can be neglected, resulting in

$$\frac{1}{Z'_{L,st}} + \frac{1}{Z'_{L,r}} = \frac{1}{Z'_{air}}. \tag{3.16}$$

Since both $Z'_{L,st}$ and $Z'_{L,r}$ contain all invariant properties of the structure, their combination can be associated with the effective impedance of the delamination-free, intact bilayer:

$$(Z'_{L,bilayer})^{-1} = (Z'_{L,st})^{-1} + (Z'_{L,r})^{-1}. \tag{3.17}$$

As a result of these associations, the condition for having a cut-off frequency can be expressed as:

$$Z'_{L,bilayer} = Z'_{air} \tag{3.18}$$

i.e. at the cut-off frequency, the effective impedance of the air layer matches the effective impedance of the intact steel/rubber bilayer. To study this requirement in more detail Z'_{air} can be approximated using a Taylor expansion under the assumption of a small air layer thickness $2\pi d_{air}/\lambda_{air} \ll 1$:

$$Z'_{air} = Z_{air}\frac{\lambda_{air}}{2\pi d_{air}} = Z'_{L,bilayer}. \tag{3.19}$$

The longitudinal wavelength and the bulk impedance of the air layer in this expression depend on the delamination properties. For a non-isolated air layer at a given frequency, since the air layer is always at atmospheric pressure, the only variable changing the effective impedance Z'_{air} is the thickness of the air layer. In the isolated models, changes in the compression, at a fixed frequency, affect the effective impedance Z'_{air} through a changing acoustical impedance of the air layer Z_{air}, through the air layer thickness/compression itself, and for the adiabatic case also through the wavelength in air λ_{air}. All these dependencies can be written as functions of compression, using Expression 3.1. For the properties of the non-isolated case this yields $\lambda_{air} = \lambda_{air,0}$ and $Z_{air} = Z_{air,0}$ since they are compression independent. (As described in section 3.2.2 the suffix '0' indicates that these are the quantities in the relaxed, and thus uncompressed, state.) For the isothermal and adiabatic case equations 3.4, 3.5, 3.7, and 3.8 can be used to express Z_{air} and $\lambda_{air} = c_{air}/f_{c,L}$ as functions of the compression ratio. Introducing these results into Expression 3.19, a global matching condition for the cut-off frequencies can be written as:

$$\begin{aligned} Z'_{air}(\Gamma, f_{c,L}) &= \Gamma\frac{\lambda_{air,0}(f_{c,L})}{2\pi d_{air,0}}Z_{air,0} \\ &= \Gamma Z'_{air,0}(f_{c,L}) = Z'_{L,bilayer}(f_{c,L}) \end{aligned} \tag{3.20}$$

where the adaptation coefficient $\Gamma = C$ for the non-isolated case, $\Gamma = C^2$ for the isolated isothermal case and $\Gamma = C^{\gamma+1}$ for the isolated adiabatic case.

The effective impedance of the bilayer $Z'_{L,bilayer}(f)$ and of the air layer $Z'_{air}(\Gamma, f)$ are given for different Γ and f in Figure 3.10. For the non-isolated case, where $\Gamma = C$, the points of intersection are the values $(C, f_{c,L})$ of maximum impedance. For the isolated cases, the points $(C, f_{c,L})$ are found after conversion from Γ to C. Since the equilibrium condition in equation 3.20 holds for non-absorptive rubber, the intersections, of which three

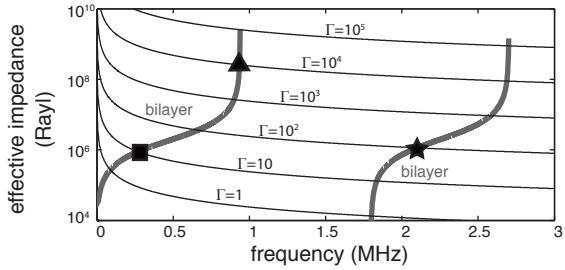

Figure 3.10 Effective impedance of the bilayer ($Z'_{L,bilayer}$) (thick gray) and of the air layer in the non-isolated case ($Z'_{air} = CZ'_{air,0}$) as a function of frequency. The symbols ■ ▲ ★ indicate intersection points where the impedance condition of equation 3.20 is met and correspond to the symbols in Figure 3.8 and 3.9.

are highlighted by symbols in Figures 3.8, 3.9 and 3.10, are in agreement with the cut-off frequencies for the non-isolated case, given in Figure 3.9, and consequently a small deviation from the numerically calculated coupling frequencies, in Figure 3.8, is found.

As discussed in section 3.3.1 and illustrated in Figure 3.9, the compression dependence of the coupling frequency is quasi identical to the one of the cut-off frequency: $f_{c,L} = af_{coupl}$. Table 3.2 summarises the fitted values for the proportionality coefficient a, for the two lowest coupling frequencies, and for each of the three thermodynamic models.

In summary, these results illustrate the similarity between the cut-off frequencies of the non-absorptive triple layer and the coupling frequencies in the absorptive triple layer and provide a rapid method to evaluate at which compression ratio the coupling between the layers of the triple layer, for a given delamination and probe frequency, is highest. Alternatively, the curves allow to determine the optimum probe wave frequency for detecting

a	0.1 MHz to 1.5 MHz	1.5 MHz to 3 MHz
NI	0.932±0.003	0.938±0.002
IT	0.92827±0.00002	0.93771±0.00004
AD	0.9352±0.0006	0.937717±0.000005

Table 3.2 Fitted values of the proportionality coefficient a between the coupling and cut-off frequency for the non-isolated, the isothermal and the adiabatic case.

delamination modulations. Differences between the three thermodynamic scenarios can be explained by the compressibility of the air layer being highest in the non-isolated case (the air can easily escape from or flow into the gap), and slightly higher in the isothermal than in the adiabatic case.

3.4 Cross modulation between wave modes due to delamination compression

When a probe wave is travelling from an intact zone in a rubber coated steel plate into a delaminated zone, then due to the mismatch in acoustic properties, mode conversion occurs, which goes along with the distribution of energy to different reflected and transmitted wave modes. In case the delaminated zone properties are modulated due to a pump vibration or wave, then the mode conversion coefficients are modulated. In this section, based on the results of section 3.3 for the sensitivity of the acoustic properties of the delamination zone, i.e. the degree of coupling and resulting attenuation, to air gap compression, we calculate the modulation of the mode conversion coefficients as a result of a low frequency pump wave, and the associated effects on the normal displacement amplitude of the probing wave at the free side of the steel layer, a quantity which is experimentally accessible in most situations (e.g. by vibrometry measurements on the outside of a storage container or transportation pipeline). For the sake of comparison, results are also shown for the normal displacement on the free rubber surface.

We start from the calculation of amplitudes of reflected and transmitted modes at the boundaries of a delamination, which is trespassed by a probe wave and which is under static compression. The geometrical properties are those described in section 3.2.1 and represent a bilayer of steel and rubber with an air filled delamination with a relaxed air layer thickness $d_{air,0}$ =1 µm. The incident probe wave is considered to have a frequency of 600 kHz, and to propagate as an LM_S mode, for which the energy flow is mainly concentrated in the steel layer (99.97%), resulting in only small absorption by the rubber layer [120]. The wavenumber in the coupled rubber/steel bilayer is $k_{LM_S}(600\ kHz) \approx (717.3 + 5.1i)\mathrm{m}^{-1}$.

Calculations of the normal mechanical displacement evolution in the neighbourhood of delamination were performed on the basis of the mode method described in detail in Ref. [120]. 31 modes were taken into account in each part of the structure under study.

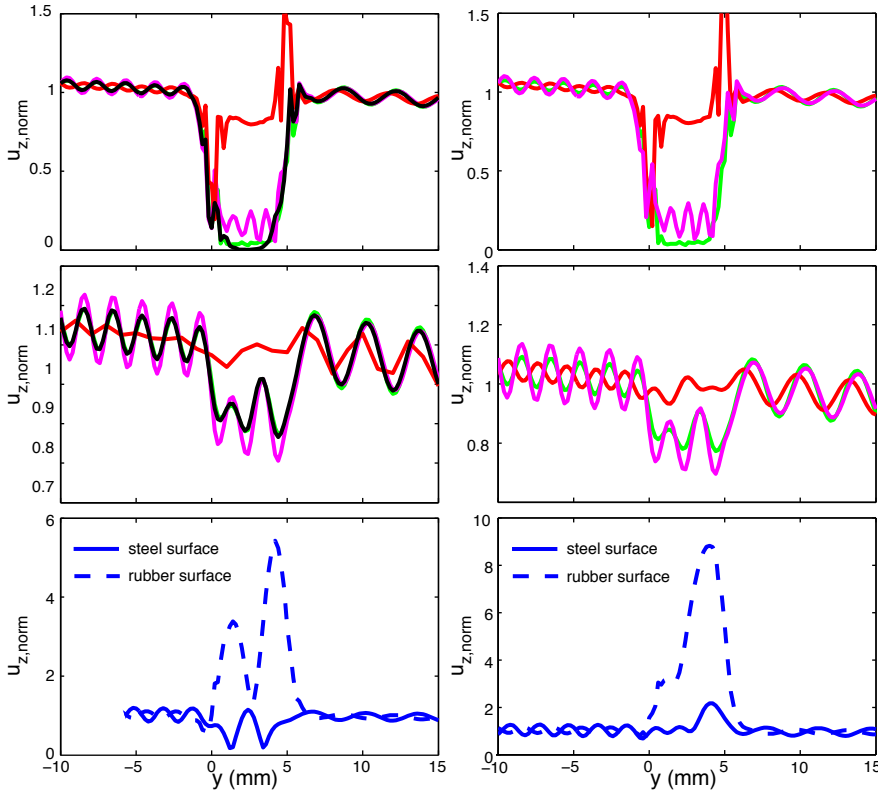

(a) Results for different non-isolated air layer thicknesses and for the extreme cases of slip and stress-free boundary conditions.
Red: slip boundary conditions
Black: stress-free boundary conditions;
Magenta: $d_{air} = 0.1\,\mu m$, $C = 10$, $Z'_{air} = 0.43E6$ Rayl ;
Green: $d_{air} = 1\,\mu m$, $C = 1$, $Z'_{air} = 0.04E6$ Rayl ;
Blue: $d_{air} = 0.02\,\mu m$, $C = 50$, $Z'_{air} = 2.13E6$ Rayl.

(b) Results for different isolated isothermal air layer thicknesses ($d_{air,0} = 1\,\mu m$).
Red: $d_{air} = 0.01\,\mu m$, $C = 100$, $Z'_{air} = 429E6$ Rayl ;
Magenta: $d_{air} = 0.3\,\mu m$, $C = 3.3$, $Z'_{air} = 0.48E6$ Rayl;
Green: $d_{air} = 1\,\mu m$, $C = 1$, $Z'_{air} = 0.04E6$ Rayl ;
Blue: $d_{air} = 0.125\,\mu m$, $C = 8$, $Z'_{air} = 2.75E6$ Rayl.

Figure 3.11 Tangential evolutions of the normalised normal displacement magnitude at the free surfaces, for an incident LM_S mode, for different different isolated and non-isolated air layer thicknesses and for the extreme cases of slip and stress-free boundary conditions. Top: results at the free rubber surface. Middle: results at the free steel surface. Bottom: results at both surfaces for $C \approx C(f_{coupl})$.

The tangential profiles of the (experimentally accessible) normal displacement components in Figure 3.11 were normalised to the incident mode amplitudes at the free steel and rubber surfaces. In order to highlight the effect of the air layer, five different static coupling situations where chosen and applied to the non-isolated (Figure 3.11a) and isolated isothermal (Figure 3.11b) case: the tangential evolutions for stress-free boundary conditions (black in Figure 3.11a) are compared with those of the relaxed state/nearly separate layers (green in Figure 3.11), results at the start of coupling/decoupling (magenta in Figure 3.11) and close to the impedance match conditions (blue in Figure 3.11) are given, and the results for slip boundary conditions (red in Figure 3.11a) are compared with the results for high compression (red in Figure 3.11b). For the sake of conciseness, the results for the isolated adiabatic case, which are quite similar to the isothermal case, are not presented.

In the uncompressed, relaxed state ($d_{air,0}$ =1 µm, green in Figures 3.11a and 3.11b), there is almost complete decoupling of the steel and rubber layers. Consequently the tangential evolutions of the normal displacement magnitude are very close to those for the steel/rubber bilayer with a stress-free delamination between the layers (black in Figure 3.11a). The degree of compression at which the steel and rubber layers start to couple/decouple depends, on the thickness of the air gap, the longitudinal wavelength in the air gap, and on the effective bulk impedance of the air. Considerable changes of the coupling between the steel and rubber layers takes place around C=10 for a non-isolated air gap where $Z'_{air} = 0.43E6$ Rayl, and at $C = 3.3$ for an isolated isothermal air gap where $Z'_{air} = 0.48E6$ Rayl (magenta in respectively Figures 3.11a and 3.11b). At very high compression the delamination behaves as a steel/rubber bilayer with slip delamination between the layers. In this regime the layers of the delamination are coupled in a similar fashion as for the case of slip boundary conditions. It is observed that the displacement of the individual surfaces within the delamination, becomes of the same order as the displacement in the intact part of the sample. At the edges of the delamination large displacement are observed, but these are assumed to result from discretisation in the simulations and not to have a physical relevance. For the non-isolated air gap this slip boundary conditions-like regime is reached for C-values above 1000, while the isolated isothermal air gap already behaves as a slip contact at $C \geq 100$. In Figure 3.11b the tangential evolutions of the normalised normal displacement magnitude for $C = 100$ in isothermal conditions is presented and are of the same order as those in the case of a slip delamination example, depicted in Figure 3.11a. Especially within the delamination much smaller

displacements are observed.

Strong coupling takes place when the probe wave frequency is chosen around the analytically and numerically predicted coupling frequencies, corresponding with the effective acoustic impedance of the air gap matching the one of the steel/rubber bilayer. For the non-isolated case the optimum is reached around $C \approx 65$ and for the isothermal case around $C \approx 8.4$. (Table 3.3 summarises the bulk impedance match conditions for $f = 600$ kHz.) In the examples in Figures 3.11a and 3.11b strong coupling in the delaminated region is illustrated in the bottom plot of the Figures, approaching the optimum compression with respectively $C \approx 50$ and $C \approx 8$. Considerable penetration of the LM_S mode of the triple layer structure into the rubber layer is seen, resulting in high attenuation of the LM_S mode.

In order to illustrate the modulation of the probe wave displacement components by dynamic compression, as presented in section 3.1 and in Figure 3.1, we consider the simplest case of uniform normal compression of the air gap along the whole length L. In practice, this is the case when the wavelength of the modulating high intensity pump wave is much larger than L. As illustrated in point (1) in Figure 3.1, we assume compression by a sinusoidal artificial external modulation force with period T large enough so that a quasi-stationary approach can be used, i.e. the modulating force is independent of the state of the air gap, and the air gap thickness simply follows the sinusoidal variations of the force between d_{max} and d_{min}, the maximum and minimum air gap thicknesses.

The normal mechanical displacement around the delamination region was calculated for a static value of the air gap thickness d_{air}, which was afterwards substituted by the time dependent function $d_{air}(t)$.

To obtain large harmonic amplitudes, the modulation of the compression ratio should be around the impedance match condition (Expression 3.20), in Figure 3.1 this is the peak frequency of the attenuation indicated by (2). When a wider compression interval is chosen mechanical displacement components hardly change in the upper and lower end of the interval. At high

	steel/rubber bilayer	NI	IT	AD
Z' (Rayl)	$2.84E6$	2.84e6	2.84e6	2.84e6
C		66.7	8.4	5.9
d_{air} (µm)		0.015	0.12	0.17

Table 3.3 Acoustical impedance matching conditions for $f = 600$ kHz.

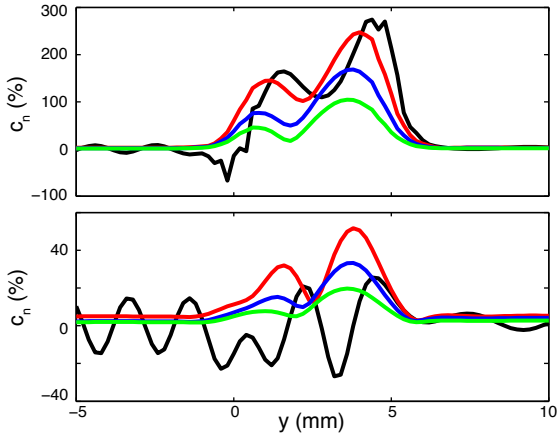

Figure 3.12 Tangential profile of different harmonic components (fundamental frequency (black line), first (red line), second (blue line) and third (green line) harmonic) of the normal displacement pattern of a probing LM_S Lamb wave at the free steel (bottom) and rubber (top) interface for non-isolated air gap thicknesses between $d_{min} = 0.01\,\mu\text{m}$ and $d_{max} = 0.02\,\mu\text{m}$.

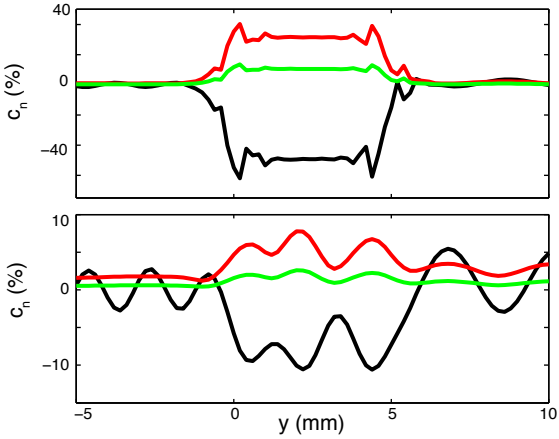

Figure 3.13 Tangential profile of different harmonic components (fundamental frequency (black line), first (red line) and third (green line) harmonics) of a probing LM_S Lamb mode at the free steel (bottom) and rubber (top) interface in the neighbourhood of an L=0.5 cm stress-free/perfect clapping delamination. Calculations were performed for a probing wave frequency and clapping duty cycle equal to 50%.

compression slip-boundary conditions are reached, while at low compression significant decoupling of the steel and rubber layers takes place. To illustrate the modulation affected time evolution of the normal displacement probe wave amplitude, the air gap thickness modulation limits ($d_{min} = 0.01\,\mu m$, $d_{max} = 0.02\,\mu m$) were chosen with $d_{air} = 0.015\,\mu m$ matching the impedance condition for $f = 600$ kHz. A conceptual representation of the underlying modulation of the attenuation is shown in (3) of Figure 3.1.

The cross-modulation harmonic amplitudes $u_{z,n}(y)$ (first,second and third harmonic) in Figure 3.12, with angular frequencies $\omega_n = \omega + n\Omega$ (ω is the angular frequency of incident wave, $\Omega = 2\pi/T$ and $n = 1, 2, 3$ is the order of cross-modulation harmonics) for the incident LM_S mode are normalised by the magnitude of the incident mode amplitudes at $y = 0 : |u_{z,inc}(y = 0)|$. The fundamental component amplitude $u_{z,n=0}(y)$ is represented by the normalised difference: $\dfrac{|u_{z,n=0}(y)| - |u_{z,inc}(y)|}{|u_{z,inc}(y = 0)|}$.

The cross-modulation harmonic amplitudes reach values up to 150-250% at the free rubber surface and about 50% at the free steel surface. In the, (not depicted) case of modulation between 0.5 µm and 0.015 µm the cross-modulation harmonic amplitudes reached 100% at the free rubber surface and about 50% at the free steel surface. This illustrates that cross-modulation harmonic amplitudes can achieve large values even for small amplitudes of the air gap thickness modulation.

An important question is to what extent cross-modulation harmonic amplitudes created in structures containing compressible layers, as in this work, differ from the ones in a simplified model consisting of a bilayer with a clapping delamination [86, 87, 89, 124]. The modulation harmonics are the largest for the delamination clapping between perfect and stress-free boundary conditions [89]. Calculation results for this kind of uniformly clapping delamination are presented in Figure 3.13 for the bilayer with aforesaid material and geometrical parameters, for a probing wave frequency $f = 600$ kHz and a clapping duty cycle equal to 50%.

Assume that the modulation of the air gap thickness takes place in the vicinity of compression required to satisfy the impedance matching condition 3.20 for the applied probe wave. In these circumstances, the cross-modulation harmonic amplitudes calculated with the three layered structure containing a compressible air gap, can be considerably larger than those created by the clapping delamination. This can be verified by comparing the results in Figure 3.12 and 3.13.

Because the compression of the air layer is well chosen, the tangential evo-

lutions of the normal displacement at the steel and rubber surfaces are significantly larger than those corresponding to stress-free boundary conditions or perfectly coupled layers. The blue curves in the bottom plots of Figure 3.11a and 3.11b illustrate the order magnitude of the generated displacements when the impedance matching condition is nearly satisfied. Consequently, modulation of these high displacements generates much larger higher harmonic components, than modulation of the displacements which correspond to stress-free and perfectly coupled boundary conditions.

In can be concluded, that cross-modulation of probe waves by a vibrating delamination is strongly influenced by the acoustic coupling between the layers. The presence of a compressible intermediate layer can result in a better acoustic matching between the outer layers. As a result, the probe waves induce much larger displacements of the structure's surfaces. This large displacements open options for the generation of large cross-modulation.

3.5 Conclusions

The nonlinear interaction between a probing Lamb wave and a locally delaminated attenuating bilayer containing an air filled delamination, whose geometrical and material parameters (the air layer thickness, the air density, and the longitudinal wave velocity of air) are periodically changing due to an artificial uniform source, was modelled using a quasi-stationary approach. Two extreme thermodynamic cases of the air layer thickness modulation were taken into consideration: the air layer was suggested to be either non-isolated or isolated from the surrounding atmosphere. The latter case was subdivided into isothermal and adiabatic modulation of the air gap thickness. The dispersion characteristics of Lamb modes for three-layered steel/air/rubber structure were analysed for a wide compression range and for the three thermodynamic conditions. Different dispersion curves were compared and the steel-like LM_S mode turned out to be the most adequate Lamb mode for practical applications. It was shown that the steel and rubber layers become strongly coupled near cut-off frequencies for longitudinal waves of the three-layered structure. The conditions for strong coupling were analytically described in a global impedance match condition and fitted to the numerical results. The compression at which the equilibrium is met is strongly influenced by the ratio of the longitudinal wavelength to the air layer thickness and by the thermodynamic conditions of the modulation through their influence on the bulk impedance of the air layer and the longitudinal velocity. A smooth transition between slip and stress-free boundary

conditions at the delamination surfaces of the rubber/steel bilayer was realised by changing the compression ratio. The transition takes place in the neighbourhood of the compression ratio at which the cut-off condition for longitudinal waves of the three layered structure is fulfilled.

The reflection, transmission and mode conversion coefficients for the incident probing wave were calculated, using a modal decomposition method. As a result of the dynamically changing interaction, cross-modulation occurred, leading to a frequency mixing process and enrichment of the frequency spectrum of the normal displacement signal evaluated at the free surfaces of the bilayer.

The cross-modulation harmonic amplitudes of the normal displacement for the three-layered structure containing a compressible air gap are largest on the free rubber surface for the incident S_0-like bilayer the LM_S mode. In this case the harmonic relative amplitudes reach the values of about 150%-250% at the free rubber surface and of about 50% at the free steel surface when the compression range is chosen in the vicinity of the cut-off condition matching compression and with an appropriate choice of its modulation amplitude. When the efficient acoustic coupling between the different layers in the delamination is achieved, the generated cross-modulation harmonic amplitudes turn out to be considerably larger compared to those created by a clapping delamination.

When extrapolating this study to more general cases a number of elements have to be considered. In the presented case the compression necessary to achieve significant coupling at 600 kHz, was in the order of 5 to 10 in the case of an isolated air layer. These compressibility's can easily be obtained when e.g. in a vessel filled with liquid. In the non-isolated case no compression of the air takes place. As expressed by the impedance matching condition in equation 3.20, the compression at which a given cut-off frequency is reached is proportional to the thickness of the air layer in the relaxed state. Consequently this parameter has a large influence on when the cross modulation is maximum. In practical applications the attenuation of the probe waves in the intact steel/rubber bilayer must be small. This can be achieved by using higher frequencies. The upper limit of this increase in frequency is obtained when the LM_S mode wave becomes a Rayleigh wave. The roughness of the steel and rubber layers also influence the behaviour of the system. The slip boundary conditions are only a theoretical limit of this system. In real life the surfaces start to though when the distance between rubber and steel is small. However, this is only a restriction to the applicability at high compression ratios.

Chapter 4

Lamb waves optimised sensing systems

4.1 Introduction

The main function of the sensing system incorporated in the investigated SHM technique, is to quantify the transmitted wave energy of the part of an emitted probe wave that follows the direct trajectory between an actuator and a sensor, without interference of late arrivals of reflected echoes of the probe wave and of environmental vibrations. The measured transmission amplitudes are processed by a diagnostic algorithm, to asses if damage is present. Measuring transmission amplitudes of ultrasonic waves seems a simple task, but in a dispersive structure with a difficult geometry it can be complicated.

In a plate, ultrasonic waves are dispersive and multiple Lamb modes can exist at a fixed frequency, as calculated in section 2.1. The probe wave – defect interaction is affected by the Lamb mode of the probe wave. These differences can be exploited when probing for cracks. However, the coexistence of different Lamb modes can also make analysis of the transducer response difficult. When a transducer is excited by a burst of a single frequency, multiple modes of different wavelengths, phase velocities and group velocities are generated. The response of the sensor, measuring the generated wave packets, strongly depends on the distance between the actuator and the sensor. Due to the different phase and group velocities of the modes, not only the time-of-flight depends on the distance, but also their mutual interference.

In order to select one mode from a burst consisting of two simultaneously excited wave packets of different modes, the following requirements have to

be met: the travel distance must be longer than the length of one burst multiplied by the group velocity of the fastest mode, and the absence of reflections during the detection period.

The complex signal that is measured when different Lamb modes coincide at a sensor transducer is illustrated in Figure 4.1. The depicted waves were constructed using experimental data which was altered in order to increase the exemplary value. The virtual response of a sensor to a situation where two modes of an probe wave (direct wave packet - dashed line) and a reflection corresponding to an earlier probe wave (dotted line) interfere, is presented by the 'transducer response' (solid line). The envelope of the transducer response is calculated by taking the absolute values of the Hilbert transform of the original data. This procedure has been used to calculate all signal envelopes depicted or discussed in this work. The direct S_0 mode interferes with the reflected A_0 wave packet and hence it is impossible to extract the features of the S_0 mode using a sensing system with a single detection transducer.

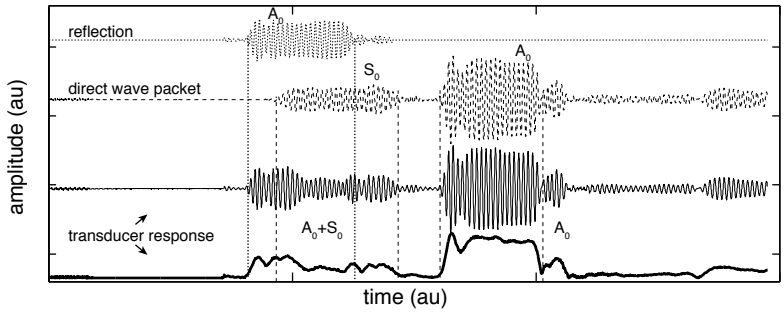

Figure 4.1 A reflected wave packet of an A_0 mode (from earlier excitation), an S_0 and an A_0 mode, which followed the direct trajectory between transducer and receiver, and the total response as it would be measured by a transducer (with the envelope in bold).

Lamb mode selection was defined as the amplification, during excitation or detection, of one single Lamb mode, while all other modes are not amplified and preferably diminish. In a perfect case of Lamb mode selection the resulting excited or detected wave is monochromatic and consist of a single mode.

The benefits of Lamb mode selective transmission and sensing are numerous. The advantage of increasing the transmission energy and amplifying the signal response in any ultrasonic sensor system of this nature are self-evident. High contrast Lamb mode selection, results in amplification without in-

creasing the amount of unwanted signal, i.e. reflections, interfering modes, while simultaneously operating as a filter, filtering out all signal except the Lamb mode of interest. Besides sensitive transmission amplitude measurements, this also allows mode conversion based detection algorithms. E.g. most types of defects cause mode conversion from one mode into another mode, and not only in reflection of the same mode. Transmission of a probe wave consisting of a single mode and detection of a different mode, would in that case indicate the existence of a crack. Detection of this type of unambiguous defect related features can only be done when adequate mode selection is available.

To differentiate between modes with the same frequency, their spatial differences, i.e. wavelength, phase velocity or group velocity, need to be exploited. Temporal selection of specific wave packets, time gating, was already suggested as one approach to select a specific mode and is based on the difference in group velocity. When using time gating, the choice of the number of periods in one wave packet is defined by the path length, the probe frequency and the difference in group velocity. This approach is very simple and effective, but it does not filter out synchronously arriving, interfering reflections and it is limited to short probe wave packages. When multiple transducers are used, Lamb modes can be selected, based on the wavelength, group- and phase-velocity, and displacement symmetry. While mode selection by time gating can only be performed by the detection sensor, wavelength-, velocity-, and displacement symmetry-selection can all be applied by an actuator and by a sensor when they consist of multiple elements.

The use of transducer arrays, not only allows mode selection but also direction selection [35, 51]. Directed transmission of probe waves into the direction of the sensor reduces the amount of unwanted reflections. In addition, directional probing can be used for defect localisation. Another option is to place multiple transducers on the sample and to use triangulation-like processing for defect detection [32, 37, 38, 41–45, 48, 50, 63]. The latter, very interesting and promising opportunities, were not studied in this work, which is focussed on arrays for selection of particular Lamb modes.

4.2 Basics of piezoelectricity

The SHM method developed in this work is based on the use of piezoelectric transducers. In view of this, a brief review of the basis of the direct and indirect piezoelectric effect is presented.

When a piezoelectric material is under mechanical stress, the dipoles inside the material are displaced. If this results in a net dipole moment, an electrical field is generated. This effect is called the direct piezoelectric effect. Similarly, in the indirect piezoelectric effect, an electric field induces displacement of the dipoles of the material and a mechanical stress is generated. A detailed description of the properties of piezoelectric materials is presented in 'Electroceramics: Materials, Properties, Applications, Second Edition' by Moulson and Herbert [128]. Some of the most important features are summarised in this section in order to provide a basic knowledge, necessary to understand the functioning of piezoelectric transducers.

A straightforward method to describe the piezoelectric effect is to investigate the underlying mathematical description. The direct piezoelectric effect can be expressed as [128]:

$$\{E\} = -[g]\{\sigma\} + \{D\}/[\varepsilon^{\sigma}] \tag{4.1}$$

and the converse piezoelectric effect can be written as follows [128]:

$$\{\epsilon\} = [s^{E}]\{\sigma\} + [d]^{\intercal}\{E\} \tag{4.2}$$

In these expressions,

$\{E\} = \{E_{xx}\, E_{yy}\, E_{zz}\, E_{yz}\, E_{xz}\, E_{xy}\}^{\intercal}$ is the electric field tensor,

$\{\sigma\}$ is the stress vector,

$\{\epsilon\}$ is the strain vector,

$\{D\}$ is the electric charge density displacement vector,

$[s^{E}]$ is the elasticity tensor,

$[d]$ and $[g]$ are the piezoelectric tensors and

$[\varepsilon^{\sigma}]$ is the electric permittivity tensor measured at constant stress.

The piezoelectric coefficients g_{ij} and d_{ij} are connected via the electric permittivity [129]:

$$[d] = [\varepsilon^{\sigma}][g] \tag{4.3}$$

The dielectric constants and electric permittivity are parameters whose values are specific for a given piezoelectric material. The most commonly used piezoelectric material is lead zirconium titanate (PZT). For PZT material, many of the piezoelectric tensor elements are zero and the piezoelectric tensor $[d]$ looks as follows:

$$[d] = \begin{bmatrix} 0 & 0 & 0 & 0 & d_{15} & 0 \\ 0 & 0 & 0 & d_{24} & 0 & 0 \\ d_{31} & d_{32} & d_{33} & 0 & 0 & 0 \end{bmatrix} \tag{4.4}$$

where the polarisation (P) of the material is chosen the z-direction. This matrix can even further be simplified since $d_{32} = d_{31}$ and $d_{24} = d_{15}$ for PZT.

When the electric charge density displacement is zero, expression 4.1 reduces to

$$E_x = \frac{d_{15}}{\varepsilon_1}\sigma_{xz} \tag{4.5}$$

$$E_y = \frac{d_{15}}{\varepsilon_2}\sigma_{yz} \tag{4.6}$$

$$E_z = \frac{d_{31}}{\varepsilon_3}\sigma_{xx} + \frac{d_{31}}{\varepsilon_3}\sigma_{yy} + \frac{d_{33}}{\varepsilon_3}\sigma_{zz} \tag{4.7}$$

For simple geometries and stresses, these expressions can be further simplified. E.g. the displacement in the z-direction (u_z) of a piezoelectric transducer with a potential difference U_z over its top and bottom electrodes, in the absence of other electrical fields, as depicted in Figure 4.2, can be expressed by an simple linear relation

$$u_z = d_{33}U_z \tag{4.8}$$

Similar expressions for the displacements in other directions and conversion from parallel compression to electric potentials can easily be obtained. The displacements induced by a potential difference over the top and bottom of a piezoelectric material are illustrated in Figure 4.2.

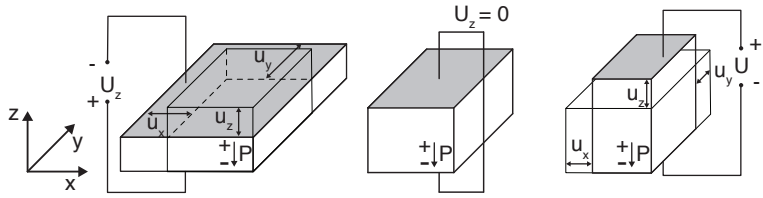

Figure 4.2 The response of a piezoelectric material to a potential difference U over its top and bottom. P denotes the polarisation vector.

Two types of PZT materials are commonly used. Soft PZT materials have a higher sensitivity and higher displacements, and a lower mechanical Q value (which determines the resonance decay time of the material) than hard PZT materials. This makes soft PZT transducers an excellent choice as a sensor, where hard PZT transducers are better fit as actuators, especially when high energy transmission is required.

Being pyroelectric, PZT materials are also sensitive to changes in temperature. These effects can typically be ignored in the laboratory circumstances. Nevertheless, they result in changed operational behaviour when under different temperature circumstances.

4.3 Transducer arrays

As in many applications, it was chosen to use lead zirconium titanate (PZT) transducers as actuators and sensors for the probe waves. PZT transducers allow sensitive detection of acoustical waves, they are easy to actuate, and to read out. Additionally, they are cheap, long-lived, sturdy, and widely available. Two different types of PZT arrays were constructed. One type consisted of individual commercially available 'Pz27 soft' PZT transducers [130] manually glued onto aluminium samples, using a template to provide regular spacing. The second type was a custom designed InSensor TF2100 linear array, provided by Meggitt Sensing Systems [131].

4.3.1 Thick transducers

In order to determine which frequencies were suitable as probe waves, the spectra of the signal response of the transducer - receiver couples were measured for the Pz27 soft transducers. A Panametrics 5052PR pulse generator was used to excite the transmitter PZT transducer, producing pulses with a duration on the order of nanoseconds and with an amplitude on the order of 100 V. The relative intensity of the loaded response between 0 MHz and 5 MHz is illustrated in Figure 4.3c. On the receiving end the direct response was measured with a PZT transducer identical to the transmission transducer. Two size's of transducers were used, a 0.5 mm × 1 mm × 50 mm transducer and a 1.3 mm × 2 mm × 50 mm transducer (h × w × l).

The sensing system based on 0.5 mm thick transducers, Figure 4.3a, was most efficient at frequencies between (0.80±0.05) MHz and (1.75±0.05) MHz and the maximum intensity was measured around (1.70 ± 0.05) MHz.

The range of high efficiency of the thicker transducer couple was shifted to lower frequencies as could be expected. The efficient transmission range lies between (0.30 ± 0.05) MHz and (0.80 ± 0.05) MHz and around (1.45 ± 0.05) MHz. The most prominent peaks were found around (0.55±0.05) MHz and (0.70 ± 0.05) MHz.

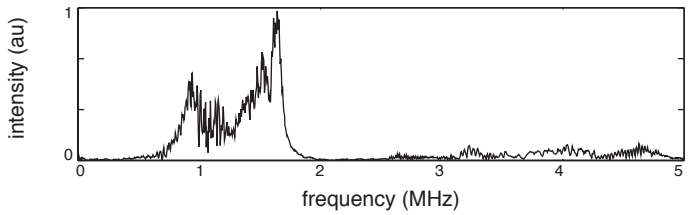

(a) Piezoelectric response when using two 0.5 mm × 1 mm × 50 mm Pz27 soft PZT transducers.

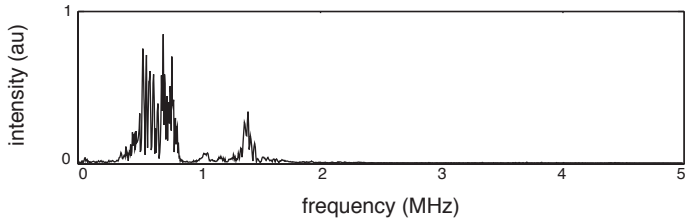

(b) Piezoelectric response when using two 1.3 mm × 2 mm × 50 mm Pz27 soft PZT transducers.

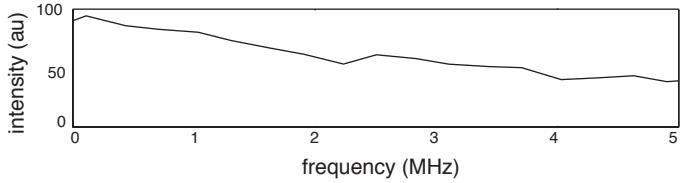

(c) Relative signal response in frequency domain of the Panametrics 5052PR pulse generator which was used to actuate the PZT transducer

Figure 4.3 Signal response in a transmitter-receiver system of two PZT transducers. The transmitter was excited by a short high voltage pulse of a Panametrics 5052PR pulse generator.

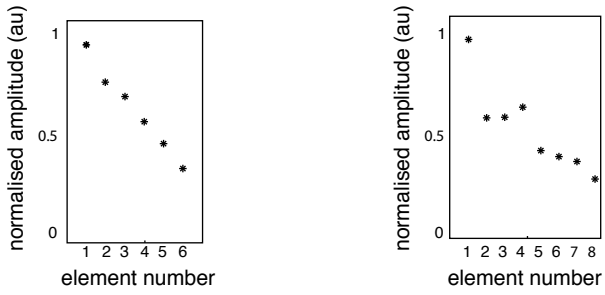

(a) Array based on 0.5 mm thick PZT transducers. **(b)** Array based on 1.3 mm thick PZT transducers.

Figure 4.4 Normalised amplitude of a wave packet measured by an individual element of the transducers array for two arrays based on PZT transducers of two different PZT element geometries.

The transfer spectrum between two transducers was measured with an 'empty' pathway, i.e. no transducers, changes in the sample geometry, mechanical contacts, or other interfaces were situated on the trajectory between the transducers. The waves emitted or detected by the inner elements of an array have to pass the outer elements. This results in reduced transmission energy. The decrease in transmission was measured for an array of 6 elements of 0.5 mm thickness, shown in Figure 4.4a, and for an array of 8 elements of 1.3 mm thickness, shown in Figure 4.4b, and a steep decrease in transmitted amplitude was observed. This limits the number of useful elements in an array of this type of PZT transducers.

The use of thinner PZT transducers (e.g. InSensor TF2100 array), which reduces reflections and mode conversion at the boundaries between the bilayer structure (PZT–sample) and single layer (sample), is the most promising and flexible solution. A second solution would be, to simulate for which Lamb modes a high transmission efficiency through the piezo array is expected. This could also be tested experimentally but that would require the construction of a large number of different geometries of PZT transducers and arrays, and is therefore difficult to achieve in practice.

In order to find a well transmitting mode, a PZT assembly consisting of an infinite array was simulated. The array was considered to consist of two building blocks: a single layer of aluminium, and a bilayer of PZT on aluminium. The boundary conditions request that the stress and displacement in the direction along the substrate are continuous at the boundaries in the substrate and that stresses are zero at the free surfaces of the PZT material.

In order to simulate an infinite array, the left boundary of PZT substrate bilayer, in the schematic representation in Figure 4.5, was matched with the right boundary of the substrate layer.

A basis of complex Lamb modes was calculated and the boundary conditions were solved, as explained in section 2.2. The calculation yielded the eigenmodes of the system. These results confirmed expectations that the optimum modes are those of which the wavelength and frequency of the bilayer and the single layer match. Further quantitative analysis of the optimum modes when an external force, such as a Lamb wave, was present, turned out to be too difficult to calculate. A detailed description of these results is presented in the Master's thesis 'Mode-selection of Lamb waves by multiplexed piezoelectric transducer' by Niels Bosman [132].

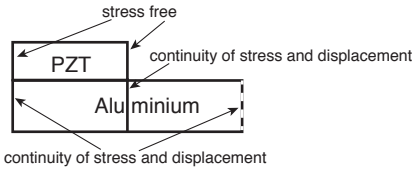

Figure 4.5 Boundary conditions for an infinite transducer array.

4.3.2 InSensor TF2100 piezoceramic array

The second investigated array, i.e. the InSensor TF2100 linear array [131], was constructed by depositing a 40 µm PZT based thick film directly onto a 1 mm stainless steel, AISI 304, plate. A gold layer was used as bottom electrode and 24 silver top-electrodes divided the thick film up into 24 transducers. Each electrode has a width of 0.5 mm and the transducer spacing is 1 mm. Pictures and a schematic representation are presented in Figure 4.6.

Due to the small thickness of the PZT layer, the excitation amplitudes of this array are rather small. Transfer measurements between two individual elements, as in the previous section, gave a low signal to noise ratio. Therefore a line scan with a Doppler vibrometer was performed on the sample. One PZT strip was excited by a Panametrics PR5052 pulse generator. The frequency - wavenumber spectrum is presented in Figure 4.7. Most energy is converted into A_0 mode waves with frequencies below 1 MHz.

In analogy with the latter tested thick transducers, the attenuation of waves trespassing the array region was measured. The normalised amplitudes, measured by the different elements of the transducers, of a wave packet of

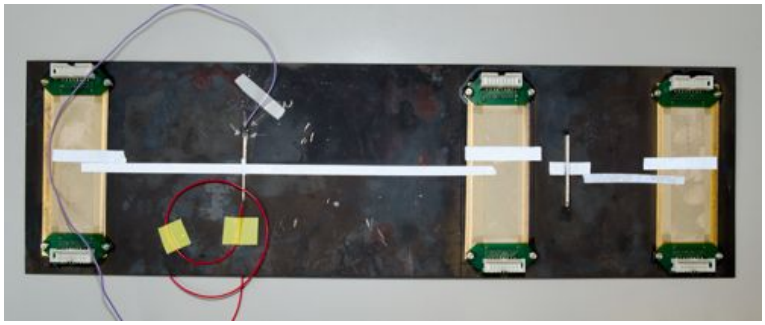

(a) Stainless steel sample with three InSensor TF2100 linear arrays and two commercially available PZT transducers.

(b) One InSensor TF2100 linear array of 24 elements.

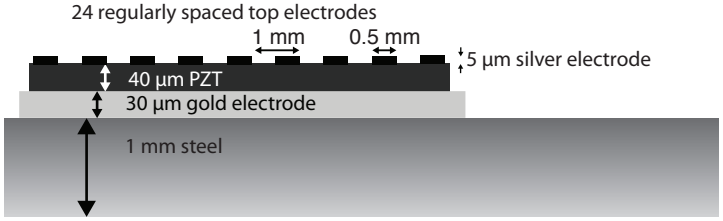

(c) Schematic view of the InSensor TF2100 linear array.

Figure 4.6 Meggitt InSensor TF2100 transducer arrays on a 1 mm stainless steel plate.

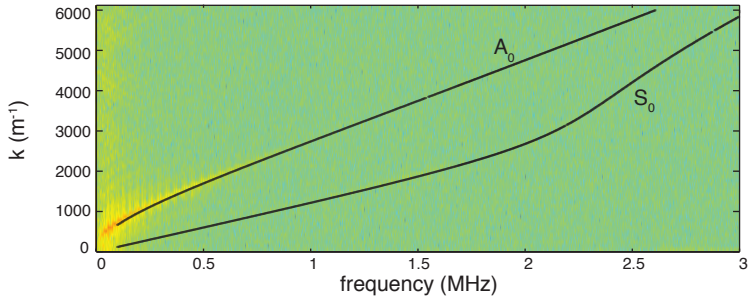

Figure 4.7 Logarithmic intensities (a.u.) of the wavenumber - frequency spectrum for one element in a InSensor TF2100 piezoceramic array excited by a nanosecond pulse.

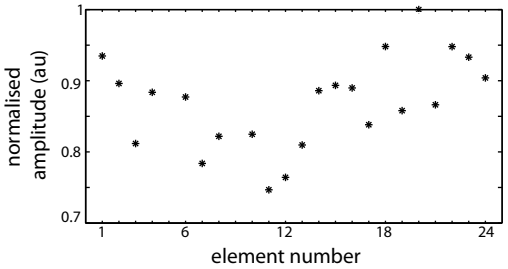

Figure 4.8 Normalised amplitude of a wave packet measured by individual elements of the InSensor TF2100 array.

1200 kHz generated by a commercial 0.5 mm thick PZT transducer, are depicted in Figure 4.8. As expected, due to the electrode array thickness (5 µm) being much smaller than the acoustic wavelength, the influence of the array on the propagation of the probe waves is marked by sensitivity variations of the individual elements.

4.4 Experimental implementation of Lamb mode selection

The Lamb waves of interest for this work are short burst of a single frequency, as is described in Chapter 5. Therefore, in this section only monochromatic bursts were used, when validating the different approaches to Lamb mode selection.

4.4.1 Wavelength selection

For guided waves in a plate, at each frequency minimum two modes with different wavelengths exist, while at each wavelength (λ), an infinite number of modes exist, as marked in Figure 4.9. Lamb mode selective detection of wave packets can be done by filtering the propagating wave packets based on their wavelength. In Figure 4.9, the frequencies of a Lamb mode with a wavelength of 2 mm in a 1 mm thick aluminium plate, are marked for $f = 1.2$ MHz and $f = 2.3$ MHz. For the $f = 1.2$ MHz two modes exist. If the frequency and wavelength are fixed only one mode can exist. In order to achieve wavelength selection, the transducers can be spaced with the preferred wavelength. The phase of the preferred Lamb waves passing by is then identical for all elements in the array. This allows in-phase excitation and detection using multiple elements. Lamb modes with other wavelengths are not in phase when passing the array elements, making their excitation and detection less efficient. Using these principles, Lamb mode selection for a single excitation frequency can be performed. Only, the propagation direction of the waves is not specified.

In practice, the spacing and dimensions of the transducers in the array define for which wavelengths optimum detection or transmission can be performed. The simplest form of selection is to excite or measure all PZT transducer elements simultaneously. In Figure 4.10 the individual response of 6 PZT transducers (D1 to D6) is shown. Waves of a mode with a wavelength corresponding to the spacing of the transducers are in phase with the excitation or detection by the transducers. In this example the spacing was 2 mm and the probe frequency 1.2MHz, the corresponding wavelengths were 4.32 mm for the S_0 mode and 2 mm for the A_0 mode. The wave packet of the mode which has a wavelength corresponding to the array spacing, here the A_0 mode, has a constant phase at every transducer. The phase of the non-matching wave packet is different at every transducer. When summing the responses of the transducers the amplitude of the 'in phase'-mode is much higher than the amplitude of the 'non matching' mode. In the example in Figure 4.10 the S_0 mode is almost 180° out of phase. The combination of a 1.2 MHz probe wave packet and a 2 mm spacing of the transducers in the detection array resulted in a strong enhancement of the A_0 mode and negligible enhancement of the S_0 mode when the output of the different elements was summed.

Although the wave packets of the preferred mode are in phase, there are still differences in time-of-flight (TOF), which results in broadening and amplitude reduction of the detected signal. The difference in TOF between

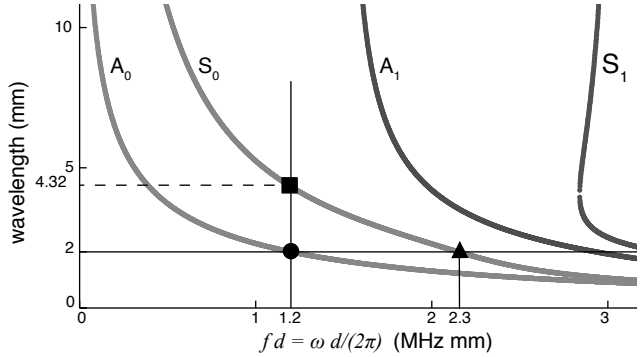

Figure 4.9 Wavelength versus frequency-thickness product. The symbols • and ■ indicate the wavelengths of a 1.2 MHz wave for respectively the A_0 and S_0 Lamb mode. The ▲ symbol indicates the frequency where the wavelength of the S_0 mode is 2 mm.

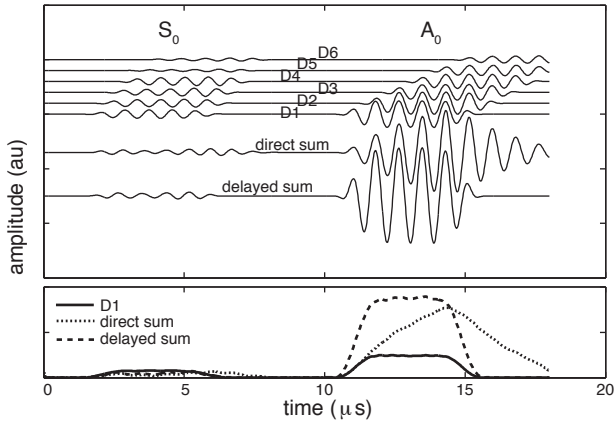

Figure 4.10 Top: responses of 6 individual transducer (D1 to D6), the (direct) sum of the responses of the 6 transducers, and the sum of the individual responses corrected for the difference in TOF (delayed sum, which is shifted 5 periods).
Bottom: corresponding envelopes of D1, the direct sum, and the delayed sum.
The transmitted wave packet had a frequency of 1.2 MHz and the spacing of the transducers was 2 mm, which corresponds with the wavelength of the A_0 mode ($\lambda = 2\ mm$).

two consecutive elements is one period (T), since the spacing corresponds to one wavelength (λ). By delaying the different responses before they are summed, the differences in TOF are corrected, and a faster rise of the envelope is observed. In Figure 4.10 the delayed sum and its envelope (dashed line) are shifted back in time (with 5 periods) for the sake of clear comparison with the signal of the first transducer (D1, solid line) and with the direct sum (dotted line). Technically, correction for the difference in TOF can be considered a phase velocity v based selection criterium since $v = \lambda/T$.

As a quantitative example, wavelength-based mode selection in transmission and reception was performed with a number of different approaches. An array of six 0.5 mm thick PZT transducers with a width of 1 mm and a spacing of 2 mm, as described in section 4.3.1, was used. The transmitting transducers were excited by a 1.2 MHz burst of 20 periods. The wavelengths corresponding to 1.2 MHz are marked by symbols (• and ■) in Figure 4.9. The number of periods was chosen so that the arrival of the S_0 and A_0 does not overlap.

To test the performance of mode selective detection, wave packets were emitted by a single PZT transducer and detected individually by all elements of the array. Summation, and other processing, of the signals was done in MATLAB®.

A number of different mode selective detection options were tested and the envelope of the wave packets is depicted in Figure 4.11a. As a reference, the direct trajectory between the first element of the array and the transmitter transducer (solid curve) was used. The amplitudes of the wave packets was quantified by taking the average amplitude of the envelope for a 4 µs interval and were then normalised by the amplitude of the A_0 wave packet of the first element. The resulting normalised amplitudes are listed in Table 4.1, together with the ratio of the A_0 and the S_0 mode.

First, the amplification of the A_0 mode, for which the array was designed, is discussed. The sum of the first three (long-dashed curve) and of all six (short-dashed curved) elements was made. The amplitude of the A_0 for both methods is around two times the amplitude of the not-enhanced A_0 wave packet. This rather poor performance – with respect to the theoretically expected amplification factors of 3 and 6 – is due to two factors. First, as described in section 4.3.1, the amplitude of the transmitted wave packets was strongly attenuated by the array. In this array, the expected amplification factor for all six elements was 3.5 ± 0.5, which is the sum of the amplitudes of the individually measured wave packages. Second, the ac-

tual responses of the different elements were not perfectly in phase. Phase differences between 5° and 10° were observed, resulting from an imperfect match between the actual wavelength of the probe waves and the actual spacing of the array elements. When delayed summation is possible, the phase mismatch can be corrected together with the difference in TOF. This phase matching (6 elements delayed, dotted curve in Figure 4.11a) results in an amplification factor of 3.25 ± 0.16 which is close to the estimated limit of 3.5 ± 0.5.

The corresponding amplitude of the S_0 mode was inherently lower and the A_0/S_0 ratio for the wave packets measured with a single element was 3.3 ± 0.2. This ratio largely varies depending on the method used to combine the individual responses. A prediction of the amplitude of the S_0 mode is hard to make. Theoretically, the more elements in the array, the better this mode should be filtered out. The random combination of phase shifts of the S_0 mode eventually lead to an average of zero. Again, the attenuation in the transducer array, due to the internal reflections and thickness heterogeneities, limits the number of useful elements in the current design. Overall, an significant increase in the A_0/S_0 ratio was found, in most cases combined with a decrease in S_0 amplitude.

In order to validate mode selective excitation, the same setup was used. The probe waves were excited by a transducer array and detected by a single element. Besides the single element to single element reference measurement, only two other options were tried, namely excitation by three elements (those closest to the receiver) and excitation by all elements. Because all elements were connected in parallel to the amplifier, the resulting excitation amplitude can not be compared to individual excitation. Therefore all results were normalised to the amplitude of the corresponding A_0 mode. The results, presented in Figure 4.11b and Table 4.1, are comparable to those of wavelength based detection, where especially excitation with all six elements turned out very effective in reducing the S_0 mode.

An array can also be used to select modes with frequencies which are multiples of its spacing. This can be either done by reducing the array to a smaller array, or by selecting elements in order to match the new wavelength. If the elements can be added and subtracted, mode selection of modes with a wavelength doubling the array spacing can be done. In this case the responses of consecutive elements are 180° out of phase. Adding and subtracting the response of consecutive elements actively selects modes with a wavelength to twice the array spacing, while the 'single wavelength mode' is being filtered out.

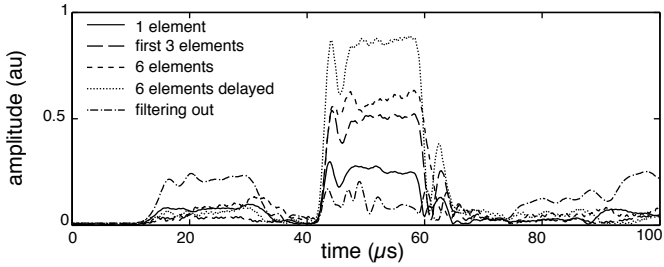

(a) Receiver array

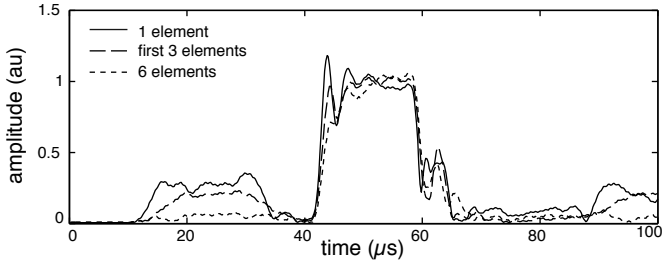

(b) Transmitter array

Figure 4.11 Envelopes of transducer responses for different approaches of wavelength based mode selection.

Detection	S_0	A_0	A_0/S_0	contrast increase
1 element	0.30 ± 0.02	1.00 ± 0.05	3.3 ± 0.2	
first 3 elements	0.14 ± 0.02	1.95 ± 0.10	14.1 ± 1.5	4.3 ± 0.2
6 elements	0.36 ± 0.03	2.22 ± 0.11	6.2 ± 0.5	1.88 ± 0.19
6 elements delayed	0.27 ± 0.04	3.3 ± 0.2	12.2 ± 1.6	3.7 ± 0.5
filtering out	0.83 ± 0.05	0.3 ± 0.1	0.38 ± 0.12	0.12 ± 0.04
Excitation	S_0	A_0	A_0/S_0	contrast increase
1 element	0.28 ± 0.02	1.00 ± 0.04	3.6 ± 0.3	
first 3 elements	0.22 ± 0.01	1.00 ± 0.02	4.6 ± 0.2	1.28 ± 0.12
6 elements	0.07 ± 0.01	1.00 ± 0.04	15 ± 2	4.2 ± 0.7

Table 4.1 Amplitudes of the S_0 and A_0 wave packets, their ratio and the increase in contrast for different types of detection and excitation, using wavelength based mode selection. For every approach, the detection- and the excitation-amplitudes have been normalised to the amplitude of respectively the A_0 mode for a single element, and to the amplitude of the A_0 mode. Contrast increase was defined as the factor with which the ratio A_0/S_0 was increased by mode selection.
$\left(* \dfrac{S_0/A_0(3 \text{ elements})}{S_0/A_0(1 \text{ element})} = \dfrac{14.1}{3.3} = 4.3\right)$

In this experiment the wavelength of the S_0 mode was 4.32 mm – marked as ■ in Figure 4.9 – which is close to twice the array spacing. The resulting envelope (dot-dashed curve in Figure 4.11a) and amplitudes (Table 4.1) of consecutive addition and subtraction illustrate that the A_0 mode is reduced to one third of its non-amplified amplitude while the S_0 mode is increased to almost three times the non-amplified amplitude.

The parameter 'contrast increase' was defined in order to illustrate the effectiveness of a mode selection approach. It is the factor by which the ratio between the preferred and non-preferred mode increased due to mode selection. In Table 4.1 the results are listed. For mode selective detection a maximum contrast increase of 4.3 was obtained when using the first three elements. For mode selective excitation a factor 4.2 was obtained when using the maximum number of elements in the array. This result suggests that increasing the array would increase the contrast of mode selection.

A single array can thus be used to select multiple modes based on the relation between their wavelength and the spacing of the array. High amplification magnitudes were observed, especially with flexible (delayed, inverted) summation. An array with narrowly spaced transducers, such as the In-Sensor TF2100 array, combined with selective addition and/or subtraction, results in a flexible tool which is capable of selecting a wide range of Lamb modes.

4.4.2 Velocity selection

Since the group and phase velocities of different modes are different, the respective probe wave packets propagate at different speeds through the arrays. If the elements of the array can transmit signals individually or add the responses with an individual delay, then the transmission and detection can be timed in such a way that the elements are in phase with the selected Lamb mode.

Individual measurements of the response of the elements of the receiver array can easily be done and mode selection, by delaying the signals before summing them, can than be done in MATLAB®. On the other hand, for realistic measurements with delayed emission, dedicated hardware is necessary. An attempt was made to develop a 24 channel amplifier in which delays between the different elements could be programmed. A 24 channel binary function generator was constructed and works well. It is programmable by LabVIEW and gives an output of -1 V or 1 V. The production of a 24 channel amplifier is the necessary next step and remains to be achieved.

Therefor, mode selective amplification using delayed signals could not be performed.

When using velocity selection in an array of transducers, the spacing of the transducer is not important, but good knowledge of the position of the transducers is required. In this technique, the phase difference of the wave packets between the transducers is corrected by delaying the received signal. The necessary delay (Δt_{ij}) that has to be applied to the response of element D_i for it to match with the response of element D_j, can easily be calculated using the phase velocity v and the distances x_{D_i} and x_{D_j} between the transducers and the source.

$$\Delta t_{ij} = \frac{x_{D_j} - x_{D_i}}{v(f)}. \tag{4.9}$$

The phase velocity, and thus also the delay, depends on the preferred mode and frequency. In practice the transducer arrays can be calibrated for different modes and frequencies, by phase matching probe waves without knowledge of the phase velocity. In the case of large differences between the group velocity and the phase velocity of large transducers, a correction for the group velocity can be included in order to minimise broadening of the original wave packet.

The envelopes of probe waves detected using velocity selection are depicted in Figure 4.12 and the corresponding amplitudes are listed in Table 4.2. The same measurements as in the previous section were used, where a 600 kHz burst of 20 periods was measured by an array of six transducers. The amplitudes in Table 4.2 were normalised to the amplitude of first the S_0, second the A_0 mode of the direct signal between the transducer and the first element of the transducer array. The amplification factor of both modes is comparable and close to the experimentally defined limit of 3.5 (argued in the previous section). The increase in contrast was also above three for both selection methods, which is of the same order as for wavelength selection.

A very useful feature of this method of mode selection is that a velocity has a direction, in contrast to wavelength, and thus not only a specific mode is selected but also its propagation in one direction. In particular, when the distance between the transducers is not matched, or random, reflections traveling in the 'opposite' direction are still out of phase after the delays are applied. Naturally this does not account for the selection of modes with a wavelength matching the spacing of a regularly spaced array. A wave with matching wavelength but opposite phase velocity is largely smeared out, but if it contains a large enough number of periods the maximum amplification is reached. In theory, without attenuation in the array, it takes $2 \times n - 1$

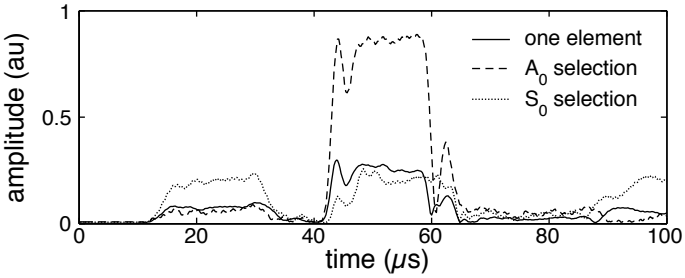

Figure 4.12 Amplitude of wave packets for not amplified signal (solid), A_0 selection (dashed), and S_0 selection (dotted)

	direct signal	A_0 selection	S_0 selection
S_0	1.00 ± 0.05	0.88 ± 0.12	2.63 ± 0.15
A_0	3.28 ± 0.05	10.8 ± 0.6	2.58 ± 0.05
S_0	0.30 ± 0.05	0.27 ± 0.04	0.8 ± 0.05
A_0	1.00 ± 0.07	3.28 ± 0.16	0.79 ± 0.09
S_0/A_0	0.3 ± 0.2	0.08 ± 0.01	1.02 ± 0.11
A_0/S_0	3.3 ± 0.2	12.3 ± 1.6	0.98 ± 0.11
contrast increase S_0/A_0		0.27 ± 0.04*	3.3 ± 0.4
contrast increase A_0/S_0		3.7 ± 0.5	0.3 ± 0.04

Table 4.2 Amplitudes of the S_0 and A_0 wave packets and their ratio for S_0 and A_0 detection, using velocity based mode selection. The amplitudes have been normalised to the amplitude of consecutively the S_0 and A_0 mode for a single element. Contrast increase was defined as the factor with which the ratio between both modes was increased by mode selective detection.
$\left(* \dfrac{S_0/A_0(A_0 \text{ selection})}{S_0/A_0(\text{direct signal})} = \dfrac{0.08}{0.3} = 0.27 \right)$

periods, with n the number of elements in the array, before the maximum amplification is reached.

Velocity selection proves to be a much more powerful, but technically more difficult approach, compared to wavelength selection. Besides its high contrast and wide range in selectable modes it also filters out reflected wave packets of opposite direction. The downside is that for individual excitation a large number of amplifiers are necessary which is costly and impractical.

4.4.3 Displacement symmetry-based selection

The displacement in the thickness of the plate is symmetrical for the S-modes and anti-symmetrical for the A-modes, as depicted in Figure 2.3. Measuring the perpendicular displacement component on both sides of the plate, and adding or subtracting the results, removes, corresponding to the operation, the symmetric or the anti-symmetric mode. This elegant and technically simple method of filtering was tested for a 1 mm plate with one transmission transducer and two reception transducers, all 1 mm thick, as represented in Figure 4.13.

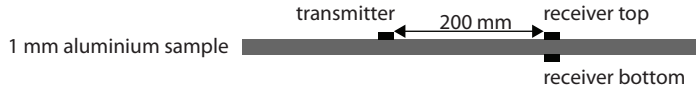

Figure 4.13 Placement of the transmitter transducer and the two receiver transducers on the sample

A wave packet of 8 periods at a frequency of 600 kHz was transmitted by a 1.3 mm thick transducer and measured by both receiver transducers which were 0.5 mm thick. The responses of the top (T) and bottom (B) transducers are shown in Figure 4.14, together with their difference (T-B) and sum (T+B). In the top plot, it is striking that the S_0 and A_0 of the top and bottom transducer are both in phase. Besides this, the S_0 mode detected by the top transducer is three to four times larger than when measured by the bottom transducer. This was not the case for the A_0 mode, where the difference was in the order of $10 \pm 5\%$. Therefore, when the difference between the responses was calculated, the A_0 mode almost completely vanished, while the maximum amplitude of the S_0 mode was still $85 \pm 5\%$ of its original value. When adding both responses, both modes are amplified to an amplitude within 5% of the sum of the amplitudes measured by the individual transducers, which is the experimental maximum.

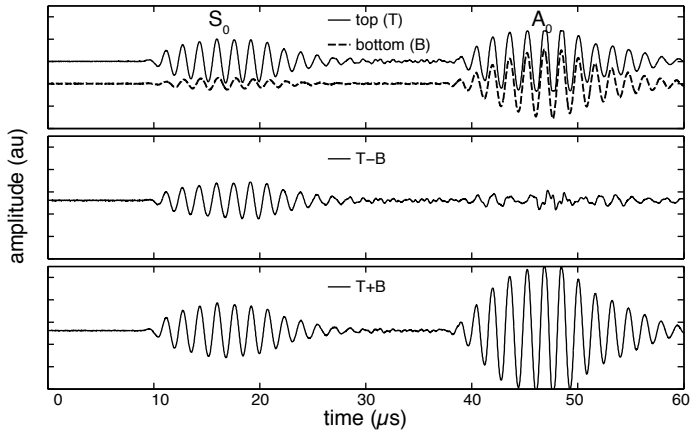

Figure 4.14 Experimental responses of the top (T, top plot - solid) and bottom (B, top plot - dashed) receiver for a transmitted wave packet of 600 kHz and 8 periods; the difference (middle plot) and sum (bottom plot) of both responses.

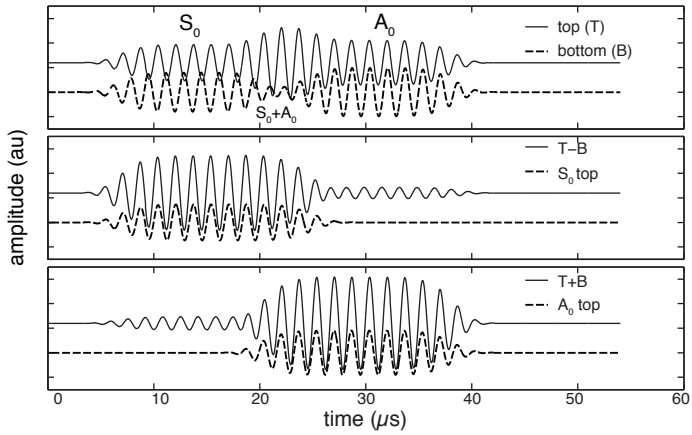

Figure 4.15 Simulated responses of the top (T, top plot - solid) and bottom (B, top plot - dashed) receiver for a wave packet of 600 kHz and 14 periods; the difference (middle plot - solid) and sum (bottom plot) of both responses, together with the pure S_0 (middle plot - dashed) and A_0 (bottom plot - dashed) wave packets.

Powerful amplification was obtained although the response of the PZT transducers did not meet the initial expectations. This unexpected behaviour will be discussed further. First an illustration of symmetry based mode selection using theoretical data is presented. In Figure 4.15 the responses of a top and a bottom PZT transducer to a wave packet are constructed. The wave packets were considered to consist of overlapping S_0 and A_0 wave packets of 600 kHz and 20 periods. The simulated transducers were expected to measure only out of plane motion of the waves (u_z). The signal of the bottom transducer was constructed so that the S_0 mode was 180° out of phase with the top transducer, while the A_0 wave packets were in phase. To increase the resemblance with experimental data small phase shifts and amplitude differences were added to the different wave packets. In the top window of Figure 4.15 positive and negative interference between the two modes can be observed in the responses of the two transducers. When subtracting both signals the symmetric S_0 mode is amplified while the A_0 mode diminishes. This is illustrated in the middle plot of Figure 4.15 by the black solid curve, the S_0 component of the top transducer is also depicted by the dashed curve. Likewise this was done for the A_0 mode in the bottom plot of Figure 4.15. In both cases very contrasting results were obtained. The amplitudes of the selected modes were close to double and the not-selected mode almost vanished.

In the simulated example of displacement symmetry based mode selection the transducer response was assumed to be proportional to the displacement of the waves in the z-direction, in accordance with expression 4.7. When measuring displacement by Lamb waves with e.g. a Doppler vibrometer, perpendicular on the surface, this assumption of mostly uniaxial displacement is valid. However, when using PZT transducers glued onto the sample this assumption becomes too simplistic, as could be observed from the experimental data (Figure 4.14). As described by expressions 4.1 and 4.7 the electric field over the top and bottom of a PZT transducer is the combined effect of the stresses along the xx-, yy-, and zz-direction. Because the transducer was mechanically coupled to the sample, it was not exclusively affected by the u_z displacement as would be most practical. According to Lamb wave theory, the σ_{zz} component is zero at the surface, introducing a transducer mechanically bounded to the surface violates this boundary condition and hence stresses in the xx-, yy- and zz-direction affect the response of the transducer. In order to provide a conceptual understanding of the displacements, and hence corresponding stresses, in the transducer, the displacements generated by a 600 kHz wave were calculated near the top and bottom of a 1 mm aluminium plate. Although this experiment illustrates

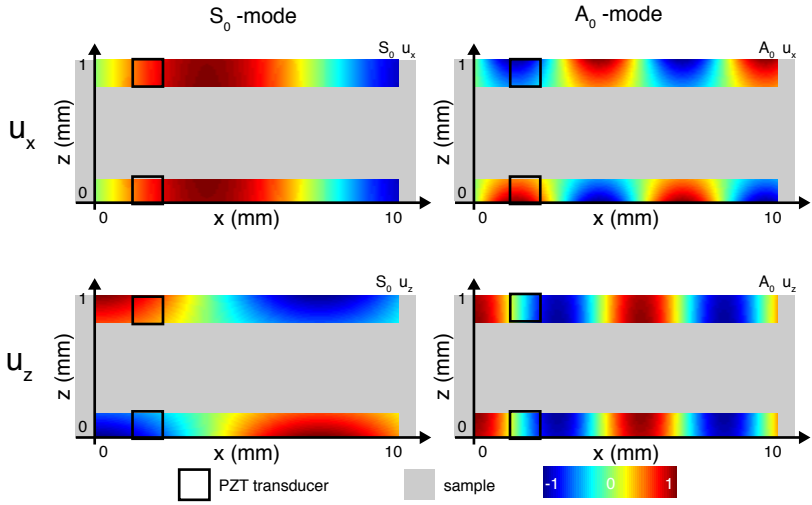

(a) Normalised displacements near the surfaces of the sample. The location of the PZT transducers is marked by black boxes.

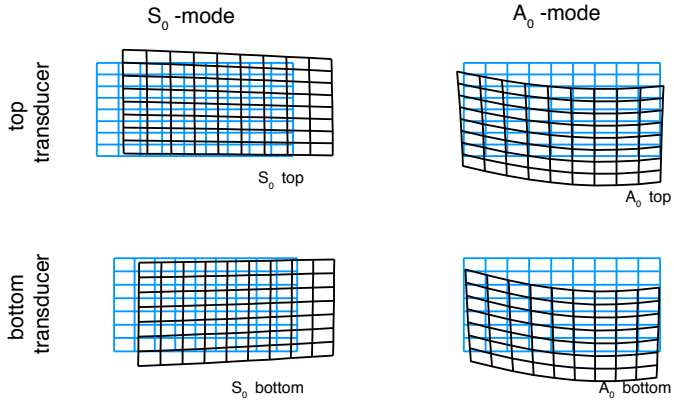

(b) Deformation of the PZT transducer corresponding to the marked windows in the figure above (Figure 4.16a). The blue grid represents the transducer in its natural state.

Figure 4.16 The displacement of PZT transducers near the top and on the bottom of a 1 mm aluminium plate for the S_0 and A_0 modes of a 600 kHz wave.

that it will not be the case in practice, the stresses in the yy-direction were ignored.

In Figure 4.16a colour-plots of the normalised displacements u_x and u_z of the S_0 and A_0 mode are presented. Virtual transducers, with a width of 1 mm, are indicated by a black squares. Although the location and characteristics of these virtual transducers are not representing a real situation, they offer qualitative insight in the complicated nature of the deformation of actual PZT transducers, which would be placed on top of the material. The regular features of Lamb modes are apparent: there is symmetry and asymmetry of the u_z displacement, with respect to the mid-plane of the plate, for respectively the S_0 and A_0 mode, a difference in wavelength between both modes. In Figure 4.16b the simulated deformation of the virtual transducers is illustrated (black grid) and compared to an undeformed transducer (blue grid). The magnitude of the displacement in the x- and z-direction was strongly enlarged, with the magnification factor of u_x equal to twice that of u_z, hence, the displacements are not proportional to the size of the transducer (in Appendix A the stress inside a plate are presented). In the Figure 4.16b, it can be observed that the stresses in the transducers are not parallel to the top and bottom surfaces, as expected in the theoretical analysis of piezoelectric behaviour which resulted in expression 4.7. In reality they take on complicated shapes. The resulting potential difference over the electrodes of the transducer is an integral of the local electric fields, while using Gauss's law. The outcome is expected to be a lot more complicated than the initially proposed linear relation. Inside the PZT transducer, the stresses strongly vary and are constantly changed by the propagating wave. This can be visualised by shifting the 'transducer box' in Figure 4.16a. Hereby, the wavelength plays a crucial role in the local change in stress inside the transducer.

In order to measure the displacement of both the S_0 and A_0 mode in a coherent manner, a transducer that has a response which strongly depends on a single direction needs to be used. With such a transducer, a very powerful and simple sensor to differentiate between symmetric and asymmetric Lamb waves can be constructed.

4.5 Conclusions

Some important properties of transducer arrays were discussed. The useful frequency range of an actuator - sensor system consisting of two single

PZT elements strongly depends on the geometry of the transducers. The two commercial available types of PZT achieved high probe wave excitation amplitudes. The transmission power of the, by Meggitt produced, InSensor TF2100 array proved to be too low to be used as actuator. This 'thick film' array could be used as sensor, and proved to have a much lower scattering, due to internal reflections and thickness heterogeneities, than the other types of arrays. The scattering due to internal reflections and thickness heterogeneities through the arrays consisting of individual elements was very high in the arrays and a decrease of transmission amplitude of $(50 \pm 10)\%$ was observed.

In wavelength-based mode selection the different elements are in phase when the selected mode, which has a wavelength equal to the spacing of the array, propagates through the array. Simultaneous excitation and summed detection resulted in amplification of the preferred mode. Amplification factors close to the experimentally obtainable limit (which incorporates the scattering through the array) were reached. The amplitude of the not-selected mode was comparable to a system without mode selection. It was shown that when the responses of consecutive elements were alternately added or subtracted, the formerly preferred mode could be filtered out, while a mode with a wavelength double the array spacing was amplified. If selection of the added or subtracted sensor elements is available, then the otherwise restricted amplification spectrum of this technique can be broadened.

When delayed excitation or summation of the transducer elements is possible, phase and group velocity based mode selection can be performed. Successful mode selective reception was experimentally realised. It was illustrated that modes with a different wavelength and identical frequency both can be amplified with a factor close to the theoretical maximum. The flexibility of this approach is much larger than for the case of wavelength selection.

Mode selection based on the displacement or stress symmetry of the Lamb modes is a very powerful tool, since it is easy to implement, and results in very high contrast mode selection [133]. However, in this work experimental validation has not been successful. The expected asymmetry between the responses to the symmetric and asymmetric Lamb waves was not observed. This was attributed to the complex relation between the wave motion stresses in the PZT transducers and their output potential. Consequently only mode amplification was performed instead of mode selection.

All three approaches hold large potential for selecting Lamb modes. The

practical implementation difficulty largely differs. Especially symmetry selection could be very performant and simple when using the proper type of sensors. Integrating it into a system that simultaneously outputs the symmetric and anti-symmetric modes would not require substantially more hardware than a simple actuator-sensor system using single element transducers. In contrast, mode selective actuators with individually delayed transducer elements require an amplifier for every applied delay and are therefore more tedious to implement.

The PZT elements with which the arrays were built have to be improved in order to achieve better results. However, using a powerful, but bulky, commercial transducer as actuator and e.g. an InSensor TF2100 array as sensor resulted in a very promising sensing system allowing almost perfect amplification with a very high sensitivity.

Chapter 5

Crack detection in practice

In this chapter, the development and validation of an on-line technique to detect dynamically opening and closing cracks based on their modulation of ultrasonic probe waves is discussed. First, the general properties of the component and the requirements, imposed on the developed NDT application, are listed. The second section describes the methodology of defect detection by analysis of vibration induced probe wave modulation. A theoretical quantification of the proposed concept, using numerical simulations, is presented in section 5.3 as a feasibility study. In the forth section of this chapter, the experimental setup, which is used to perform the measurements reported in the fifth, sixth and seventh section, is described. The results and observations of the measurements during crack development in a thin aluminium plate are presented in the fifth section. From the observations made in the first tests, it was decided that the sensing system should be placed in a region of low stress. Therefore a new type of sample was made. This sample was used to design and validate different diagnostic algorithms. The results and observations thereof are described in the sixth section. The developed diagnostic algorithms were tested on a number of samples using automated decision-making procedures, presented in section seven.

5.1 Specific problem statement

The proposed application has been developed with implementation in aeronautical applications in mind. The initial concept, developed in the scope of the EU's 'Seventh Framework Programme for Research'-project AISHA-II [134], aimed to detect cracks in a slat track. Later, the applicational field was expanded to all different types of critical components in vibrating environments, e.g. components of wind turbines, airplanes, oil pipes, chemical

product storage-tanks, etc. Figure 5.1 depicts a slat-track and its position in an airplane wing.

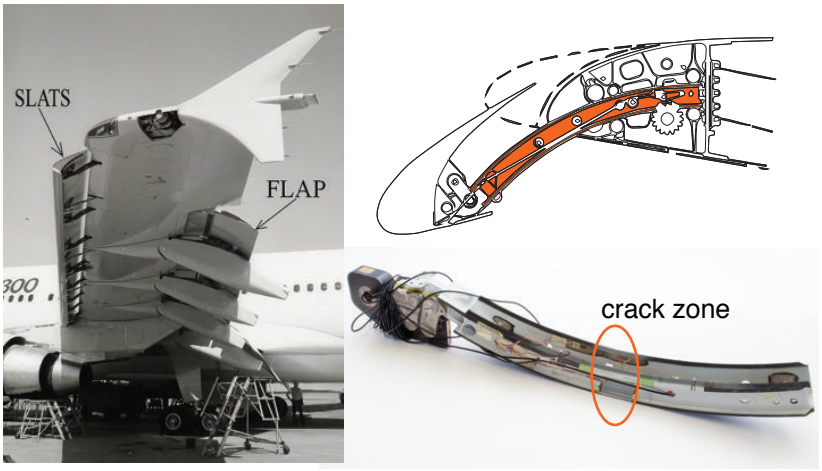

Figure 5.1 A slat track and its actual position and function in a wing. Source [135, 136]

In order to acquire experimental data and test the sensing system, a laboratory setup was build. This laboratory environment was a strong simplification of the real life environment in which the targeted components are situated. Therefore additional requirements are imposed on the application. Although these requirements are not necessary in the laboratory setting, they are indispensable for real life implementation.

The key properties of the targeted component and the settings in which SHM of the component will occur, are analysed in the following enumeration. These properties are taken in consideration during the development of this application. Although most elements are strongly connected, they are discussed individually.

- The component is of structural importance: The component is expected to be of high importance for the safety of the structure. Early-stage detection of damage is essential, in order to prevent the damage to grow out and put the whole structure at risk. When damage is detected, urgent inspection is required, followed by replacement or repair of the component. Monitoring of the remaining lifetime is therefore less important.
- The component is subject to fatigue loading: Due to variable loading of the component fatigue cracks initiate and propagate.

- The fatigue damage is closed when not under load: Detection of the crack requires nonlinear ultrasonics or on-line detection.

- The approximate location of the damage is known: From simulations, experiments or experience, the approximate location of the damage is known and hotspot monitoring is required. Damage localisation is not a priority.

- The component is a part of a vibrating structure: Dynamically varying loads on the component cause varying stresses inside the component, which modulate the state of the defect. Interaction of probe waves with a defect results in nonlinear amplitude modulation.

- The component has mechanical connections with a larger structure: Due to the vibration of the structure, probe waves are subject to nonlinear amplitude modulation at mechanical contacts. The nonlinear contributions originating from contact surfaces are very similar to nonlinear contributions of defects. Therefore, wave packets which did not follow the direct trajectory between the actuator and sensor have to be filtered out of the analysed signal.

- Vibrations induce a noisy background: Vibrations during operation create a large amount of noise sources: loose mechanical contacts, clapping sheets and wires, wind flow, etc. all add to background noise. The level of this, mostly low frequency, noise is affected by the operational conditions. The characteristics (origin, frequency, amplitude, etc.) of the noise can change significantly during operation and over the lifetime of the structure.

- Changing environmental conditions: E.g. an airplane wing is under very different stresses at rest, during take-off, during flight, and during landing, but as well temperature, humidity, etc. strongly vary. Also, changes over the life time of the component such as structural changes outside the component, changed sensitivity of the sensing transducers,etc. can change the load on the component, location of contact surfaces, sensing system efficiency,etc. And even dirt build-up can work as an absorptive layer. Consequently the amplitude/energy of the received ultrasonic waves can significantly change due to varying, defect-unrelated, environmental conditions. Hence monitoring of the amplitude of the probe wave transmission over longer periods of time is impossible. Therefore diagnostic algorithms have to be independent of the effective probe wave amplitude and reference-free. Neverthe-

less, it is expected that the environmental conditions are constant over timescales in the order of minutes.

- The component is inaccessible: The component cannot easily be dismounted or accessed for inspection. In order to ensure practical applicability of the NDT technique, durable, sturdy, and small components must be used and the NDT device should be connected to a central SHM-system. The NDT application should be able to provide the user with comprehensive and unambiguous information about the health of the component.

In summary the requirements for the developed NDT technique are: durable, sturdy, simple, unambiguous, on-line applicable, able to detect closed cracks, reference-free, unaffected by noise and vibrating contacts, robust to environmental changes.

5.2 Methodology

Consider a crack in a sample that is closed when the sample is not under load and that opens when the sample is under load. When a sufficiently large cyclic load is applied on the sample, the crack opens and closes. In this process, the degree of opening of the crack depends on the applied load. In the proposed method, during the vibrating load, a transmission measurement is performed using a high frequency (HF) probe wave. If the crack is closed, the probe wave does not encounter a region of acoustic mismatch and achieves normal transmission through the crack zone. When the load increases, the crack starts to open, resulting in mode conversion of the probe waves at the open part of the crack. Consequently the probe wave transmission depends on the magnitude of the applied load on the component. In this example of a damaged sample, the transmission amplitude cyclically changes from high transmission at low applied load to low transmission at high loads, and thus the probe wave transmission amplitude undergoes nonlinear modulation and more mode conversion. On the other hand, cyclic loading of an intact sample does not change the propagation properties in the monitored region. Hence no modulation of the probe wave transmission is expected. Therefore, monitoring the properties of the modulation can be used to differentiate between an intact and a damaged sample. In order to detect fatigue damage, while fulfilling the requirements discussed in the previous section, first, a sensing system with data processing has to be provided to measure the probe wave transmission and, second, diagnostic

algorithms have to be developed to detect damage related modulation of the transmitted probe wave.

In the proposed sensing system ultrasonic waves were used to measure the transmission in the defect region. Emission and detection of probe waves is performed by two commercially available piezoelectric transducers. Piezoelectric transducers were chosen for their simplicity in operation, general availability, low price, compact size, and long lifetimes.

Probe waves interacting mechanical contacts are modulated in a nonlinear way, since clapping of vibrating contacts induces cross-modulation and other forms of nonlinearity. These nonlinear probe wave modulations cannot be differentiated from defect-related nonlinearity and should therefore be filtered out of the analysed probe signal. Only probe waves that followed the direct path between both transducers, without encountering any (non-defect) obstacles, should be analysed.

When using a continuous monochromatic probe wave, differentiation between monochromatic contributions, e.g. direct signal and reflections, is impossible. In the case of a short burst, temporal differentiation is possible, by time gating, i.e. processing only waves arriving at the receiver transducers within a specified time window. When the probe waves are Lamb waves, different modes travel at different group velocities. The delay, with respect to the transmission of the burst wave signal and its duration time, can be chosen to include a wave package of a mode of interest. The combination of burst probe waves and time gating removes all reflections from boundaries and mechanical contacts and allows mode selective detection in plate-like structures.

The disadvantage is that diagnostic algorithms based on frequency spectrum analysis are no longer easily available. This is due to two reasons. First, in samples where the group velocity is dispersive, wave packets with different frequencies travel with different group velocities. E.g. to detect defect-generated higher harmonics, as described in section 1.1.2, a specific time window should be set over the expected arrival time of the higher frequencies. This requires detailed information about the location where they were generated, which is often not available. Additionally, if the group velocity of a harmonic frequency is lower than the group velocity of the probe frequency, its arrival might by accompanied by modulated reflections.

In another successful crack detection method, sideband frequencies are analysed. In the case of a modulated crack, the frequency spectrum of the transmitted probe waves is enriched with sideband frequencies generated

by the low frequency (LF) modulation of the transmission amplitude by the crack [93]. Here, this method cannot be applied due to the short probing time and the corresponding low resolution of the frequency spectrum.

The defect detection concept is represented schematically in Figure 5.2. The transmission amplitude is probed by short probe waves with a frequency several orders higher than the vibration frequencies and with a total length much shorter than the timescale of the vibrational changes. These short probe waves and the defect-modulating low frequency vibrations are depicted on the left. Depending on the presence of a defect, amplitude modulation takes place or is absent, as illustrated in the centre part. The time gated and demodulated measured transmission amplitudes are visualised on the right (red dots). Analysing the slow modulation of the demodulated high frequency probe waves, reveals the presence of a defect causing the modulation.

The developed diagnostic algorithms use the differences in the relation between the applied load and the measured transmission amplitudes in an intact and in a damaged sample, to determine the state of the sample.

5.3 Quantification of mode-conversion at a modulated crack

In order to test the feasibility of defect detection, based on nonlinear modulation of probe waves, the expected probe wave modulation of a propagating crack was simulated. In a typical fatigue loading process, a crack is initiated, whereafter it propagates. Initially, very slow 'stage I propagation' is observed [137]. After a certain time, 'stage II propagation' takes place, which is marked by faster crack extension, perpendicular to the applied load,

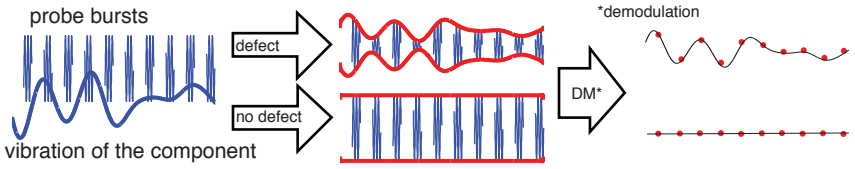

Figure 5.2 General concept of the developed crack detection method: The vibration of the component opens and closes a crack and thereby modulates the probe waves. In the absence of a crack no modulation is detected.

and cyclic features [137]. In a final stage, the sample becomes unstable and rapid crack growth, due to plastic deformation, leads to shear fracture.

A fatigue crack that undergoes a cyclic load, opens and closes (partially), causing modulation of the transmitted probe waves. The further the crack has propagated, due to the fatigue loading, the more pronounced is the modulation. The stages through which a fatigue crack goes when it propagates are illustrated in Figure 5.3.

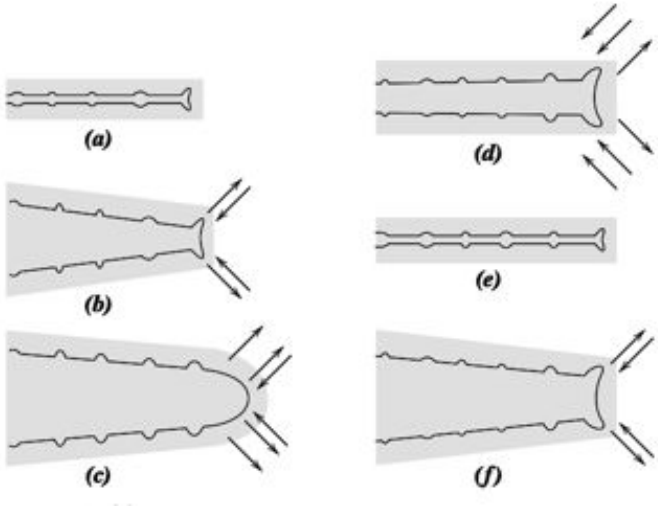

Figure 5.3 The evolution of a crack during one fatigue cycle. (Source [137].)

At the start of the stress cycle (zero or minimum load on the sample) the crack is closed or at its minimum size (Figure 5.3a). The crack tip has the shape of a sharp double-notch and the acoustic mismatch between both sides of the crack is at its minimum. If the crack is fully closed, acoustic waves are expected to be almost fully transmitted. When the load on the sample increases, the crack starts to open and the acoustic mismatch increases. Consequently, a larger part of the probe wave energy is reflected. When the load increases further, the tip notches undergo local deformation (Figure 5.3b). As the crack is opened further, the tip propagates by shear deformation and a blunted tip is formed (Figure 5.3c). When the load decreases again, the directions of the shear deformation at the tip are reversed (Figure 5.3d). Following the decreasing crack-opening, the acoustic mismatch decreases again. Eventually, a new sharp double-notch tip is formed (Figure 5.3e). While repeating these stages every cycle, the crack propagates one notch per cycle, until a critical size is reached and the stage

of rapid crack growth occurs [137].

In the performed simulations, only the effect of the size of the crack was considered. The crack growth was modelled as a constant and the evolution of the crack size was expressed by the 'average crack size'. The opening and closing of the crack due to fatigue loading were modelled as a linear variation of the average crack size. The actual crack size used to determine the probe wave transmission was thus defined as follows:

$$c(t) = at + \Delta a_{modulation} \sin(2\pi f_{loading} t) \tag{5.1}$$

with $c(t)$ the actual crack size as a function of time, a the growth rate of the average crack size, $\Delta a_{modulation}$ the modulation amplitude of the crack size, and $f_{loading}$ the frequency at which fatigue loading takes place.

A two dimensional model of a 1 mm aluminium plate with a propagating crack was used. First the transmitted energy at the crack was calculated for the S_0 and A_0 mode, using mode conversion coefficients calculated with the procedure explained in section 2.2. The incident probe wave had a frequency of 600 kHz, and hence only the first two Lamb modes, S_0 and A_0, exist in this configuration. To simplify matters, it was considered that the incident probe wave consisted of a single mode. The transmitted energy was defined as the ratio between the energy of the incident wave and the energy of the transmitted wave of the same Lamb mode. This corresponds to the definition of the mode conversion coefficient, given by expression 2.33. Energy converted from the incident mode to the other mode was neglected, which is in correspondence to the envisaged experiments where only one detected mode is analysed.

Three types of crack were considered: a symmetric crack, developing at equal pace from the top and the bottom of the plate towards the centre (left panel of Figure 5.4a), an asymmetric crack, also propagating from the top and bottom surface towards the centre but not with an equal pace (middle panel of Figure 5.4a), and a crack growing from the top to the bottom surface (right panel of Figure 5.4a).

The dependence of the relative transmitted amplitudes versus the average crack size are depicted in Figure 5.4. The average crack size is expressed as a percentage of the plate thickness, i.e. the average crack depth is 0% in the intact state and 100% when the (combined) cracks are equal to the thickness of the plate.

A distinct difference between the transmitted energy fraction of the different cracks was found. The modulation of the probe waves is thus dependent

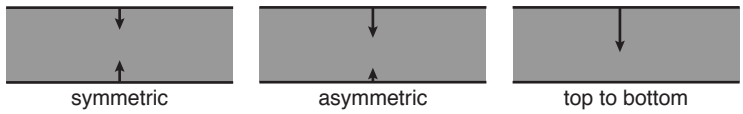

(a) Geometry of the three types of cracks. The arrows denote the growth rate of the cracks.

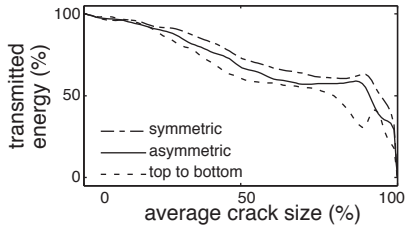

(b) Relative transmitted energy of the A_0-Lamb mode.

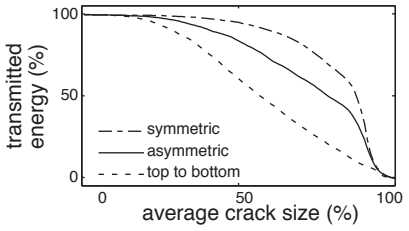

(c) Relative transmitted energy of the S_0-Lamb mode.

Figure 5.4 Simulated transmitted energy fraction versus average crack size given for an incident Lamb mode of the S_0 or the A_0 mode for three types of defect symmetry in a 1 mm aluminium plate.

on how the crack is formed and propagates. Symmetric cracks result in higher transmission than non-symmetric cracks. This behaviour can be understood when qualitatively evaluating how waves propagate through the 'crack plane'. (The stress and displacement of both Lamb modes are illustrated in Appendix A.) A mode arriving at the crack forms a source within the boundaries of the remaining connection between both sides of the crack plane. When this source is symmetric to the middle of the sample, propagation of stress and displacement on the other side of the crack are symmetric as well. Consequently, they reach the sample surfaces simultaneously, thereby generating a mode identical to the incident mode. It was verified, using the presented simulations, that in the case of a symmetric crack, no mode conversion between the different Lamb modes occurs. Consequently, all un-transmitted energy is reflected into the same Lamb mode as the incident one. Experimental validation of this observation has been done by e.g. Benmeddour et al. [133]. In the case of an asymmetric transmission area, the 'source' is closer to one of the surfaces and 'reconstruction' of the original wave pattern becomes more complicated. This results in more reflection and more mode conversion than for a symmetric crack. Because the displacement in the S_0 mode is symmetric, asymmetric placement of the 'source' has a larger influence on the transmission of this mode than for the

A_0 mode. E.g. the vertical displacement (u_z) of the A_0 mode has the same direction over the whole thickness of the plate, where for the S_0 the direction changes through the plate (cf. Figure A.1). Changing the transmission window has thus a more profound influence on the symmetric mode.

In order to emphasise the distinct difference between the transmission of both modes, the transmitted energy of the S_0 and the A_0 mode are plotted together in Figure 5.5, for the case of a symmetric crack. If the initial transmitted energy of both modes is known, their ratio could be used to detect cracks and estimate the crack size size. In practice however, this is rather difficult due to the strong dependence of the conversion coefficients on the geometry of the crack, which is very unpredictable.

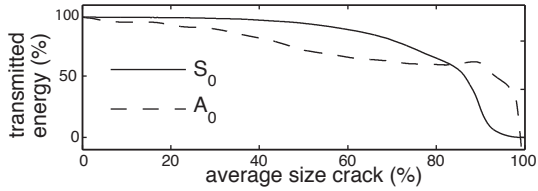

Figure 5.5 Transmitted energy of the S_0 and A_0 Lamb modes versus average crack size for a symmetric crack.

In the presented simulations, the growth rate of the average crack size a during fatigue loading was considered to be 1% of the plate thickness for every cycle and the modulation amplitude of the crack size $\Delta a_{modulation}$ was chosen to be 4% of the plate thickness. For every cycle, 50 transmitted energies (i =1 to 50), A_i^j were calculated for all of the 100 different relative sizes j of the crack. In reality, the growth rate of the average size of the crack is not constant in time. The growth rate of a crack during stage II propagation is presumed to follow Paris' law [137]. (Paris' law is discussed in section 5.5.1.) Opening and closing of the crack also depends on the average crack size and this relation is expected to be nonlinear. At a certain compression level, the crack is fully closed and additional compression does not have a further influence. Therefore both the assumption of a linear increase in crack size, and a fixed 4% modulation amplitude are not very realistic. Nevertheless, they were used because of their exemplary value. The evolution of the relative transmitted energy of a probe wave during the described linear fatigue loading process are presented in Figure 5.6 for the case of a crack growing from the surfaces to the centre (symmetric case), with transmitted energies as depicted in Figure 5.5.

The plots on the right of Figure 5.6 give a detailed view on the relation between the actual crack size and transmitted energy. The transmitted

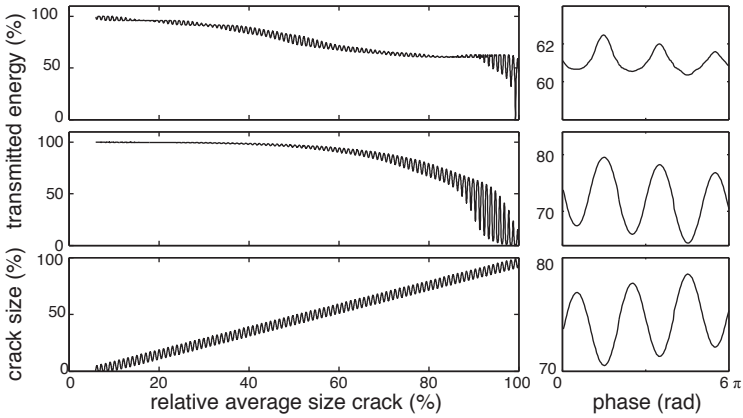

Figure 5.6 Transmitted energy of the A_0 (top, left) and S_0 mode (middle, left), and actual crack size (bottom, left) versus average crack size with an enlarged view around 80% for three fatigue cycles (right) for the case of a symmetric crack.

energy and the plots on the left are an enlarged view taken around 80% of the average crack size. The modulation, induced by fatigue loading, is clearly visible in this example.

The increase of the average crack size results in a decrease of the average transmitted energy, which could as well be concluded from Figure 5.5. Such a decrease could also be detected with measurements at a fixed load, as in classic linear US-NDT applications. However, in this example the crack was considered to be open, even when the load is minimum. In practice this is often not the case, seen that at low loads the actual crack size remains zero and the transmitted energy is constant, which makes linear US crack detection impossible.

The right hand plots in Figure 5.6 show a clear negative correlation between the instantaneous crack size and the transmitted energy. In a flawless sample the correlation between both is expected to be zero, since the transmission through an intact material is independent of the applied load. A transition from zero correlation to negative correlation would indicate the appearance of a crack. Another interesting feature is that when the crack increases, the amplitude modulation starts to increase, especially for the S_0 mode. This feature has already been exploited in other NDT methods. Vanlanduit et al. [138], defined a nonlinearity parameter which quantifies the modulation of the transmission amplitude of probe waves through a defect region. They illustrated that for a developing crack the nonlinearity related modulation

increases significantly. Other elements, such as the statistical distribution of the transmission amplitudes throughout a fatigue loading cycle, which is expected to be random in an intact sample, or the transmission amplitude at at certain load, can all be studied in order to develop diagnostic algorithms.

The goal of this project is to develop and validate different diagnostic algorithms, similar to the previous examples, using data acquired in an experimental laboratory setup. The algorithms should satisfy the requirements set in section 5.1.

From the results of this simulation can be concluded that the geometry of the fatigue cracks has a strong influence on the mode conversion and thus on the fatigue loading-induced modulation of the transmitted energy. Additionally, different crack size dependent features were detected, which can be used to construct diagnostic algorithms.

5.4 Experimental setup

The investigated samples, an aluminium plate and an aluminium bar with 1 mm thick crack-susceptible region, are described in section 5.5.1 and 5.6.1.

The excitation and detection of the probe wave packets was performed by two 'lead zirconate titanate type Pz27 soft' (PZT) transducers, produced by MEGGITT [130]. The excitation in all experiments has been done by a PZT of 50 mm by 2 mm by 1.3 mm (l × w × h). The detection has been done by this PZT and by a smaller one of 50 mm by 1 mm by 0.5 mm. The frequency spectra of both types of PZT transducers are discussed in section 4.3. The main differences are that the excitation amplitude of the thicker transducers is significantly larger than the excitation amplitude of the thin transducers for frequencies below 1 MHz, and that the difference in the width of both transducers results in a different spatial resolution. The response of the PZT transducers is the combined effect of their internal stress and the displacement of their contact surfaces. A larger contact surface smoothens the response to the propagating waves. Initially, only the thick PZT transducers were used. Later on, they were replaced by the thin ones to receive higher spatial resolution. The probe signal was a sinusoidal 600 kHz burst of 5 to 8 periods provided by a function generator (Tektronix AFG 3021) and was amplified to 50 V by a homemade amplifier. The variance in amplitude throughout one experiment was of the order of 1 V. Between different samples the variance in amplitude was of the order of 10 V.

The samples were fatigued by an MTS-810 load bench, depicted in Figure 5.7. Unless noted differently, a 6 Hz sinusoidal load between of 600 N and 6000 N was applied. These amplitudes were selected so that the fatigue led to total fracture after about half a day, providing a sufficiently large and detailed data set.

In order to compare the low frequency loading of the sample with the amplitude of the probe waves, the loading was measured. This can be done indirectly by measuring a derivative property of the loading force, e.g. the displacement of the sample, or by measuring the loading force itself. The proposed method for the ultimate practical application would be to take the low frequency signal component of the sensor PZT transducer. Here, in order to facilitate analysis of the data and due to modulation of the transducers, which is described in detail in section 5.5.4, it was chosen to record the low frequency vibrations by an extra sensor. First a Brüel & Kjaer accelerometer combined with a Brüel & Kjaer Charge Amplifier Type 2635, was used to measure the low frequency vibrations of the sample. Both methods provide an indirect measurement of the load force and have to be converted to obtain the correct loads. Later, as a result of an update of the MTS-810 controller hardware, the force applied by the MTS-810 was directly obtained from the MTS-810 hardware interface.

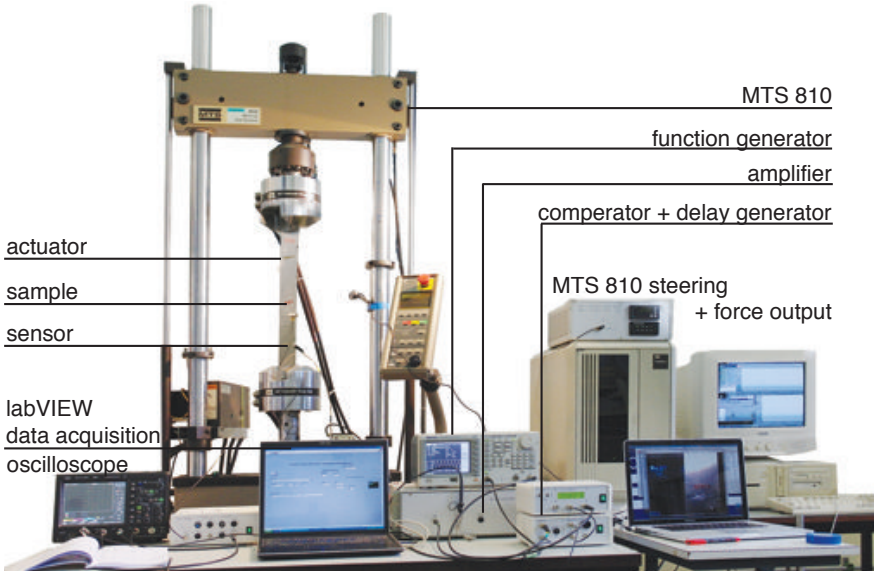

Figure 5.7 MTS-810 load bench, fitted with an aluminium plate.

For further improvement of the data analysis, the measurements were not taken randomly, but the acquisition-timing was synchronised with respect to the phase of the fatigue loading. A comparator was used to trigger a delay generator, which was set to probe every fatigue loading cycle with 50 temporally equally spaced delayed measurements. Errors in the triggering by these devices can result in unevenly distributed sampling of the fatigue loading.

The low-frequency response of the PZT, caused by the fatigue loading of the sample, was filtered out by a high-pass filter. Both the low-frequency signal of the load, and the high-frequency PZT response, were collected by an oscilloscope in sets of 50 measurements. Processing of the measurements to quantifiers of the amplitude of transmitted wave packets and values quantifying the applied force, was done afterwards in MATLAB®.

A schematic overview of the latest setup is presented in Figure 5.8.

5.5 Preliminary tests using Al plates

In this section a series of experiments are discussed. To illustrate the general observations, the results of one experiment are used. Unless stated differently, the discussed observations hold for all experiments performed on the same type of sample. In section 5.7 the results of a second experiment,

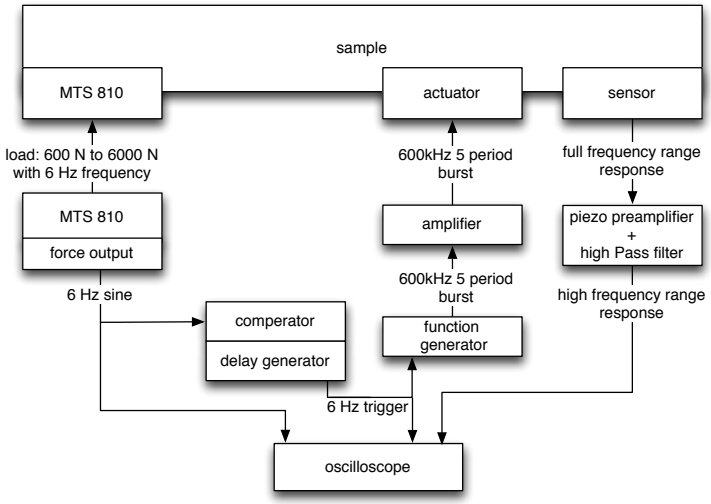

Figure 5.8 Schematic overview of the latest setup.

performed on the same type of sample, are added.

During a fatigue experiment, the sensing system is not connected to the steering of the MTS-810 fatigue loading. Consequently it was not possible to obtain the exact number of fatigue cycles while performing a measurement. In order to determine the number of cycles at a measurement, the total number of cycles of the fatigue test was interpolated. The time stamp on the measurements allows one to calculate the corresponding number of cycles. In this work, the time (in minutes) is used to refer to a specific instance. Since all experiments, unless noted differently, were performed with a fatigue cycle frequency of 6 Hz, multiplication with 360/minute gives an estimation of the corresponding number of cycles.

As mentioned earlier, multiple fatigue loading experiments, during which transmission data were collected, were performed. In a first stage, the main focus was on the development of reliable hardware with a sensitive and sturdy sensing system. The most prominent features thereof are discussed in this section. Next, the focus could be changed to actual development and validation of diagnostic algorithms for crack detection, as is presented in section 5.6.

5.5.1 Sample geometry and typical course of the experiment

Geometry of the 1 mm aluminium plate sample

The geometry of the samples was based on the dimensions of the AISHA-I standard sample, in the scope of the subsequent AISHA-II project [134]. The modified sample was 1 mm× 60 mm × 600 mm. In the middle a hole of 3 mm is drilled to accelerate crack initiation and choose the location. The transducers were placed at 200 mm from the boundaries and from each other, and hence 100 mm from the crack-initiation hole. A technical drawing of the samples is presented in Figure 5.9. In this configuration the first-arrival time of the S_0 mode is $38 \pm 3\,\mu s$ and of the A_0 mode was $68 \pm 3\,\mu s$. Bursts of the S_0 mode shorter than $30 \pm 5\,\mu s$ arrived temporally separated from the A_0 contribution of the wave packet. The first reflections of the S_0 wave were estimated to have a first-arrival time of $115 \pm 20\,\mu s$. The number of periods in one burst was chosen, considering these first-arrival times.

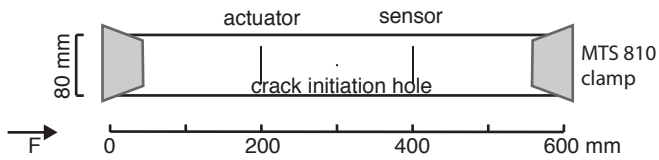

Figure 5.9 Geometry of a 1 mm aluminium plate sample. F indicates the direction of the fatigue loading force.

Experimental details

Probing has been done by a 5 cycle burst with a frequency of 600 kHz and an amplitude of 50 ±1 V. At these settings S_0 and A_0 probe waves with high signal to noise ratio were measured. Judging from the first-arrival times, it could be expected that a burst of 10 to 15 cycles would fit the time window between S_0 and A_0 arrival, but oscillations of the actuator transducer extend the wave packet. In order to obtain clean separated wave packets, in practice a burst of 5 to 8 excitation periods was used.

Fatigue loading was done at 6 Hz with the pulling force varying between 580 N and 5800 N. This leads to a maximum extension of the plate by 0.5 ± 0.1 mm for an intact sample. These loads were selected because they fall within the linear elastic regime of the stress-strain relation of 1 mm aluminium and result in initiation and growth of a crack in around three hours.

Observations about the evolution of the fatigue damage

The observed process of fatigue failure of the sample follows the expected typical behaviour. First, a period of crack initiation, during which no defects are visible to the naked eye, takes place. Then small signs, in the form of hair-line cracks, start to show around the crack-initiation hole. Since the tension is highest at the surfaces, the first crack starts on one of both surfaces and on one of both sides of the hole. Eventually, 4 hair-line cracks form, namely at both sides of the plate and of the hole. These hair-lines are first observable by eye after around $(3 \pm 1)\ 10^4$ fatigue cycles or 80 ± 5 minutes when they have a length of 2 ± 1 mm. Crack initiation is then followed by crack propagation, which is very slow initially, but accelerates with the amount of cycles. Typical behaviour of crack growth is illustrated in Figure 5.10 and can be calculated using Paris' Law: [137]

$$\left(\frac{\mathrm{d}a}{\mathrm{d}N}\right) = \mathrm{C}\Delta K^m \tag{5.2}$$

where a is the crack length, N the number of fatigue cycles, C and m material constants and ΔK the stress-intensity factor.

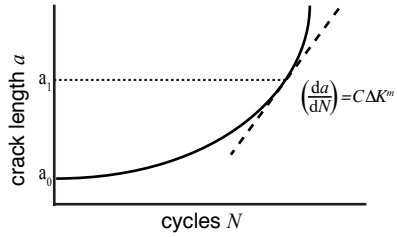

Figure 5.10 Crack length versus number of cycles. (Figure source: [137])

It is hard to quantify the actual increase of the damage in this experiment, since the cracks grow in two directions – in the width of the sample and in the depth – as marked in Figure 5.11. The initial hairlines grow to about 22 ± 5 mm, resulting in a total crack of 44 ± 10 mm, which seems to be the critical length. The next stage of 'rapid breakage' starts with the crack becoming visually open. In a matter of minutes, estimated to be $(5 \pm 1)\,10^3$ cycles, the crack grows rapidly (in the order of mm's), followed by plastic deformation of the sample and breakage. The entire process of crack initiation, crack propagation, and sample breakage typically takes $(70 \pm 15)\,10^3$ cycles, which takes 200 ± 40 minutes.

Defects in real life structures

The timescales at which cracks in real life structures develop are of a very different order than for the samples used in the fatigue experiments. Also, the loads leading to fatigue damage or of significantly different order and nature. However, the frequency range of the modulation of the cracks, induced by vibration of the component, can be considered comparable. This frequency range was measured to be in the order of 1 to 10 Hz [134]. Therefor the mechanisms of crack growth and initiation in the experimental data are strongly accelerated, while probe wave-modulated crack interaction is expected to take place on a representative time scale.

The aluminium panels of which the fuselage of most airplanes is build up, are held in place by rivets. The rivet holes act as sources of crack initiation and hence have a comparable role as the holes drilled in the experimental samples (Figure 5.11). The most significant load on the fuselage is induced by pressurisation of the cabin. During every flight an airplane is pressurised and depressurised and thus every flight corresponds to one fatigue cycle.

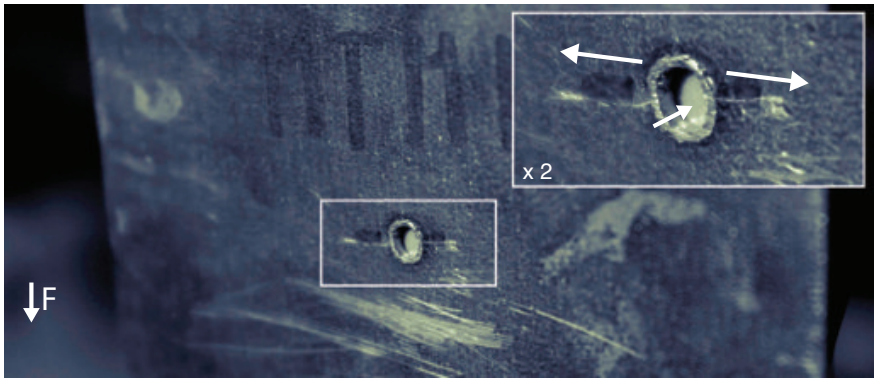

Figure 5.11 Fatigue crack on the back side of a sample after $(79 \pm 2)\, 10^3$ cycles. The arrows in the inset indicate the direction of crack growth, F denotes the direction of the fatigue loading force.

Although the largest difference in stress takes place due to pressurisation, also in-flight vibrations induce fatigue loading, which causes modulation of cracks. Due to the difference in the direction of the applied force and the difference in how the plates are attached to structure, the actual load on the fuselage panels can not easily be compared to the load applied on the samples. Also, the rivets holding the panels in place influence the forces around the rivet hole, which also has an influence on how defects are initiated and propagate.

Severe accidents due to fatigue damage in the fuselage have been reported [139]. A fatal accident with a Boeing 737-200, where a large section of the fuselage was swept away, occurred after 89680 flights and 35496 flight hours [139]. This number of cycles at failure is in the order of the $(70 \pm 15)\, 10^3$ cycles that where typically observed in this experimental environment. Despite this agreement, there is little basis to predict when the crack would have started and if the crack propagation behaved similar as in the experimental environment. Fuselages of this type of aircrafts were developed to withstand 75000 flights. Therefore, it can be expected that damage is not observed as early as in the experimental samples (after $(35 \pm 15)\, 10^3$ cycles as is indicated by Figure 5.19), but that propagation is relatively faster, once a crack is initiated.

The fatigue loading on a slat track is substantially different from the case of fuselage panels. During take off, the slats make up a large part of the wing area. The load carried by the slats is supported by slat tracks. In e.g. a Boeing 737 typically 6 to 8 slats are used, each with four slat tracks [140].

Consequently, a slat track is under large loads during take-off and landing. Again, the frequency range of the vibrations of a slat track lies between 1 and 10 Hz [134]. Therefore, a slat track undergoes a much larger number of high amplitude fatigue cycles than the fuselage. For a plane of which the slats are under substantial loads for 10 minutes during take off and landing, and which makes 2 flights a day, 350 days a year, around 4 10^6 fatigue cycles a year are expected. This number is of a totally different order than for the tested samples and for the fuselage. This estimate is strongly influenced by the number of flights a given aircraft makes.

Collected data

In total 85 sets of 50 measurements, each containing two waveforms, were collected during $(65 \pm 2)\,10^3$ cycles of fatigue loading, which corresponds to a timespan of 180 ± 5 minutes. In order to simplify analysis of the data, the measurements were synchronised with the 6 Hz fatigue loading as described in section 5.4. Figure 5.12 is an overlaid plot of the loads as a function of the phase of the fatigue load, of all sets. The precision of the delayed triggering was high throughout the entire experiment and only a small minority ($< 1\%$) of the triggers were incorrect. An incorrect trigger can be recognised in Figure 5.12 by a spike in the load. Since for most measurements the precision on the load was very high, the individual curves for the different sets are not visible. The standard deviation on the load for a given phase was in the order of $7 \pm 2\%$.

When analysing statistical features of the experimental data, it is important to know how the measurements are distributed over the fatigue loads. The measurements had a uniform probability distribution over the phase of the fatigue cycle. The load itself was sinusoidally proportional to the phase and was thus not sampled with a uniform distribution. When a sine function is sampled uniformly in time domain, a symmetric distribution arises, with

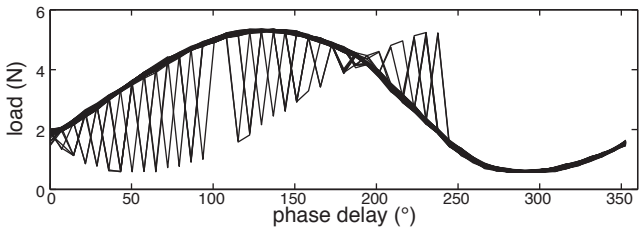

Figure 5.12 Overlaid plot of the applied fatigue load versus phase of the fatigue loading cycle for 85 sets of 50 measurements.

highest probability at the maximum and minimum amplitude and uniform-like distribution near the average of the extremes. A histogram with the data from all measurements and a histogram of one set of 50 measurements is shown in Figure 5.13. The data were distributed as expected, with higher probability towards the extremes. In perfect conditions, the distribution of a uniformly sampled sine results in equal mean and medium values, which are equal to the average of the minimum and maximum value. When statistically analysing the transmission rates corresponding to the loads, the transmission at high- and low-load have a stronger influence on the mean, median, quantiles, etc. than values at intermediate loads.

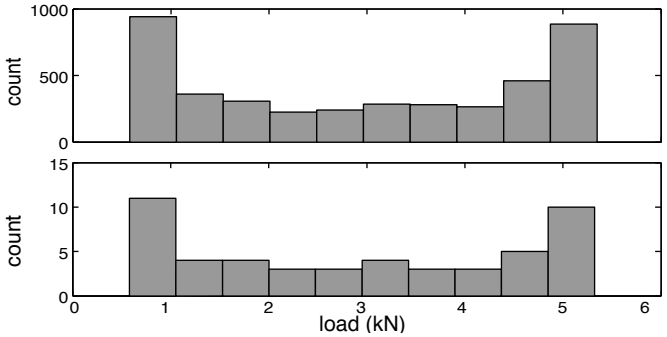

Figure 5.13 Histograms of the load for all measurements (top) and for a random set of 50 measurement (bottom).

5.5.2 Processing of experimental results

During the fatigue experiment, probe waves were continuously transmitted through the defect region. An oscilloscope, synchronised to the fatigue loading, stored 50 times the received wave packet and the output of the load signal. Hence every set consisted of 2×50 waveforms and a time stamp. These data needed to be processed for further analysis, satisfying the applicable requirements of section 5.1.

Time gating

The high-pass filtered response of the receiver transducer is shown in Figure 5.14. Only a short time window of the PZT response was processed. This window is depicted by the rectangular window in Figure 5.14. The S_0 and the A_0 Lamb modes were separated in time, as was calculated in

section 5.5.1, and the gate was set to select the S_0 mode. For detailed information about Lamb mode selection, refer to Chapter 4.

Transmission amplitude quantification

In order to examine the probe wave transmission between the actuator and the sensor, a quantifier needed to be extracted from the gated PZT response. Calculating the energy of the emitted wave and the energy of the received wave, using a PZT transducer based sensing system, is a complex process. In order to simplify matters, a linear relation between the amplitude-related properties of the selected wave packet and the transmitted energy was presumed. It was also assumed that the energy of the emitted probe wave packet was constant over the collection time of one set of (50) measurements (which is in the order of minutes). In a laboratory setup this assumption often holds for an entire experiment. In real life applications this assumption is less likely to hold on longer timescales. On the other hand, in the laboratory setup the crack size increases during the collection of one set of measurements, which is not likely to happen in a real life application. For more details concerning the origins of changes in probing energy and wave transmission properties, refer to section 5.1. A number of options to convert the PZT response into a scalar transmission amplitude were considered:

- Maximum amplitude of the wave packet (A_{ampl}): This parameter was calculated by taking the maximum value of the Hilbert transform of the wave packet. In Figure 5.15a this value is indicated by the dotted line.
- Integral of the wave packet envelope (A_E): The average of the envelope, calculated using the Hilbert transform over the entire wave packet. This value is comparable to the RMS value of the wave packet.
- Lock-in detection (A_{LI}): Lock-in detection is very useful when processing complex and noisy signals and could therefore be an optimum choice in practical applications. In order to obtain a single value from the lock-in detector some options are available. One, the averaging time can be set to match the entire length of the gated response and the value at the end of the gating window is stored as transmission amplitude. Two, a shorter averaging time can be used and the maximum value or the integral of the response of the lock-in detector can be stored. In Figure 5.16 the first method was used.

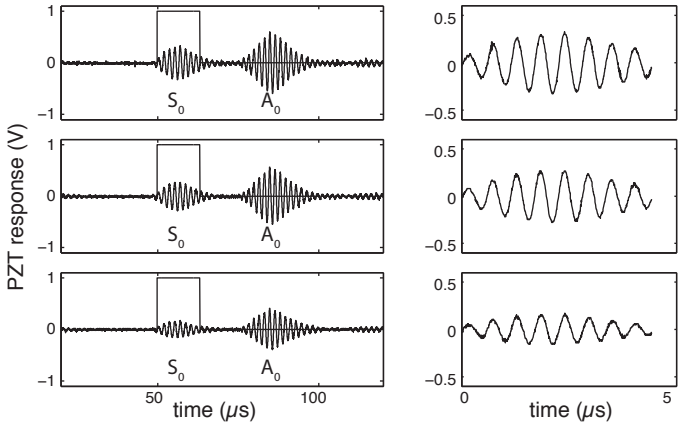

Figure 5.14 Left: Three high-passed PZT responses at different stages of the fatigue loading (top: beginning; middle: intermediate; bottom: end) of the 1 mm aluminium sample and the selected time gate. Right: The same signals after time gating.

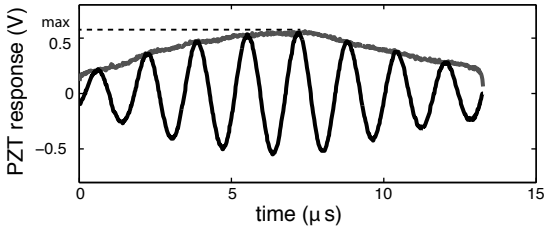

(a) Highpass gated PZT response and governing envelope.

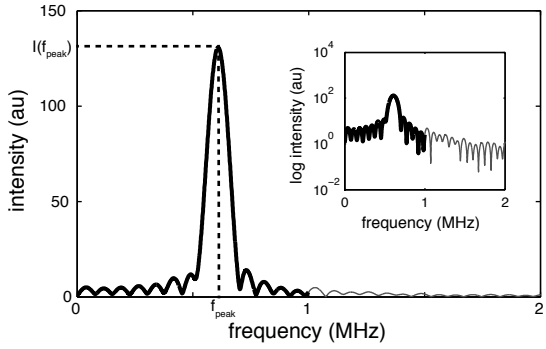

(b) Spectrum of highpass time gated PZT response.

Figure 5.15 Schematic representation of the determination of a transmission quantifying parameter in time and frequency domain.

- Amplitude peak frequency (A_{peakf}): The Fourier transform of the gated PZT response is shown in Figure 5.15b. (The PZT response was padded with zeros in order to increase the resolution in the frequency space.) Around the probe frequency of 600 kHz the frequency spectrum has a sharp peak. The frequency at which this peak is maximum is called the 'peak frequency'. This frequency is considered to be the main frequency of the selected wave packet. Shifting of a peak maximum can occur if the detection response is not flat. In that case, a peak spectrum is filtered by e.g. the flank of a bandpass spectrum of a piezoelectric sensor, which can bring about a shift of the peak frequency. The intensity of this peak corresponds to the amplitude of the waves at the peak frequency in the wave packet and is thus called the peak amplitude.

- Integral of the frequency spectrum (A_{intf}): The integral of the squared spectral peak corresponds to the total energy in the wave packet. In this case the integral was taken over only a selected range of frequencies, this range is marked in thick black in Figure 5.15b

From these five options, the peak amplitude was selected. In real life applications lock-in detection or others might be better. Both lock-in detection and the peak amplitude consider only a small frequency band and are very efficient in extracting information out of complex and noisy acoustical data. The single frequency approach eliminates a whole range of noise sources. The only substantial unwanted contribution in the processed response, could be coming from reflections of the probe signal, but, as with any other approach, these were filtered out by time gating. In the laboratory environment were the data is processed offline, the Fourier analysis based parameter was preferred. The corresponding peak frequency is also used to monitor the modulation of the sensing system in the following analysis.

The amplitudes calculated by the different options are very similar, which illustrates that they are all valid candidates to serve as quantifier for defect induced probe wave modulation. In Figure 5.16, the differences are illustrated using an arbitrary chosen set of measurements (taken when the sample was already damaged). In order to allow comparison, the results of the different methods were normalised so that their average was one. The relative differences with the amplitude peak frequency-method, as shown in the top Figure, are of the order of $\pm 1\%$, where as the difference in transmission amplitude due to fatigue loading are in the order of $\pm 10\%$, as illustrated in the bottom plot. Figure 5.17 shows the difference between the transmission

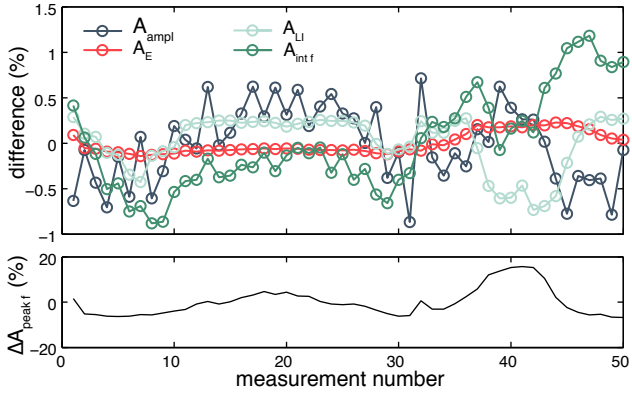

Figure 5.16 Top: Relative difference between transmission amplitude calculated by different methods (A) to the quantifier based on the peak amplitude (A_{peakf}). (Calculated as $A/A_{peakf} - 1$.)
Bottom: Relative deviation from average transmission amplitude calculated as the peak amplitude (A_{peakf}).
(Calculated as $A_{peakf}/\text{average}(A_{peakf}) - 1$.)

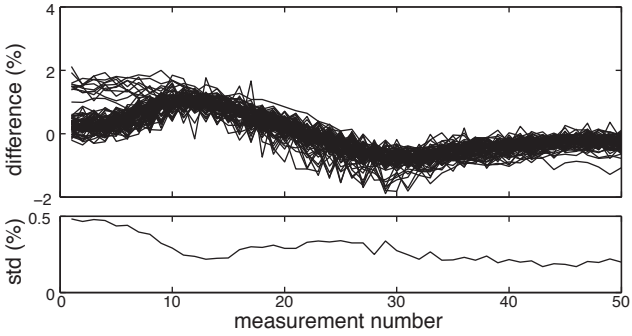

Figure 5.17 Top: Relative difference between transmission amplitude calculated as amplitude of peak frequency (A_{peakf}) and as the integral of the frequency spectrum (A_{intf}), for all sets of the fatigue experiment. (Calculated as $A^j_{intf}/A^j_{peakf} - 1$.)
Bottom: Standard deviation of the data in the top plot.

amplitude calculated with the integral of the frequency spectrum method, and the peak amplitude, for all sets acquired in one fatigue experiment, illustrating the difference between both quantities.

From here on is referred to the peak amplitude of the Fourier spectrum as the transmission amplitude and serves it as quantifier for defect-induced probe wave modulation, calculated as follows:

$$A_i^j = \max(\text{abs}(\text{fft}(\text{gated PZT response}))) \tag{5.3}$$

were $i \in \{1, 2 \dots 50\}$ denotes the measurement number and hence refers to the phase in the fatigue loading cycle, and $j \in \{1, 2 \dots \text{number of sets}\}$ denotes the number of the set of 50 measurements to which the transmission amplitudes belong and hence is linked to number of fatigue cycles or time and consequently the 'health' state of the sample.

Processing procedure summary

The data collected during an experiment were grouped in a number of sets. Every set contained 50 coupled measurements of the load-output and the high-pass filtered PZT response. First, the measurements were time gated by selecting only data within a specific time window. Next, for every measurement the measured load was averaged, while a Fourier transform of the PZT response was taken, of which the peak frequency and its amplitude were calculated. For a fatigue experiment in which n sets of measurements were collected, a data set of $n \times$ (50 couples of load and transmission amplitude) was produced. These results were then analysed for their general evolution in transmission amplitude and for nonlinear modulation by damage in the sample. An overview of workflow is represented in Figure 5.18.

5.5.3 Analysis of transmission under average and quasi-static load regimes

In this section, data analysis is performed using algorithms comparable with those used in linear ultrasonic NDT techniques, of which examples were given in the state of the art in Chapter 1. However, fatigue loading of the plate modulates the size of the crack, thereby causing nonlinear modulation of the transmission amplitudes while determining average and quasi-static quantities. Therefore, due to the possible rectification mechanisms, the modulation could induce quasi-static differences compared to classic linear US-NDT where the sample is at rest.

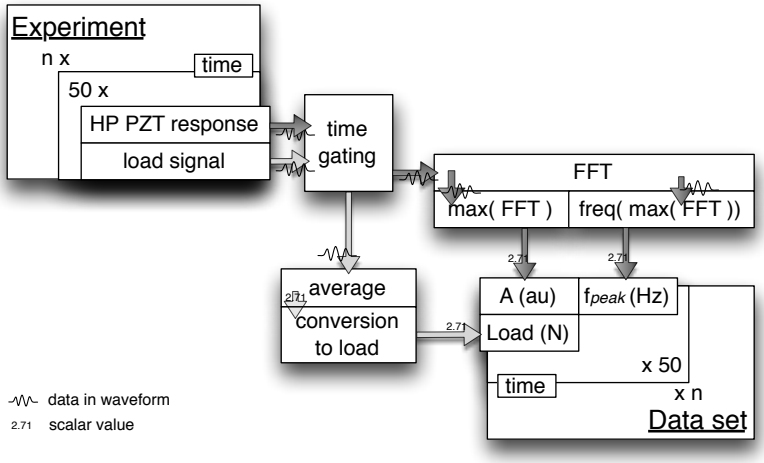

Figure 5.18 Signal processing from experiment to data set.

Transmission amplitudes at different load regimes

For every set of 50 measurements the average transmission amplitude A^j_{mean} was calculated:

$$A^j_{mean} = \sum_{i=1}^{50} A^j_i/50 \tag{5.4}$$

In addition, other distinct transmission amplitudes, i.e. the instantaneous transmission amplitude at low-load A^j_{580}, hence around 580 N, at high-load A^j_{5800}, which was around 5800 N, the maximum transmission amplitude $A^j_{\max}$, and the minimum transmission amplitude $A^j_{\min}$ throughout a modulation cycle, were extracted and are shown in Figure 5.19. The data of the entire fatigue experiment were normalised relative to the average transmission amplitude A^j_{mean} of the first 10 sets.

The different transmission amplitudes, or transmission quantifiers, were used to compare the general evolution of the transmission amplitude corresponding to different load regimes. The time at which the normalised transmission amplitude reached a decrease of 5%, 10%, and 20% is listed in Table 5.1. The results for 5% and 10% decrease provide a measure of the sensitivity in time domain of the corresponding parameter to cracks. It is was assumed that a sensitivity of this order should be reachable in real life applications. The time of 20% decrease quantifies the rate whereby the corresponding sensing parameter decreases for growing cracks.

When comparing the experimental data to the simulated data discussed in

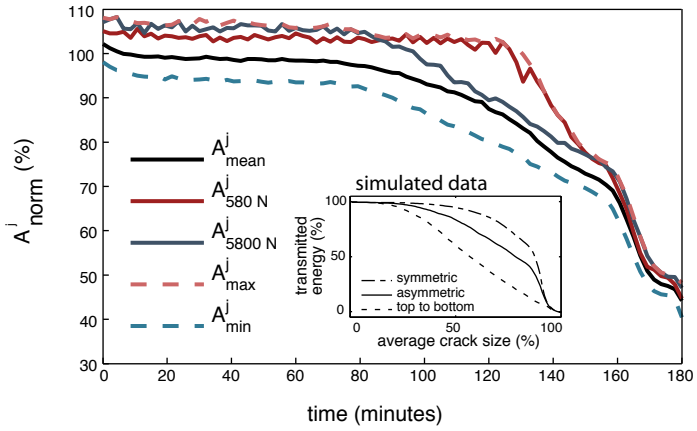

Figure 5.19 Normalised transmission amplitudes of the S_0-part versus fatigue loading time, with A^j_{norm} calculated as: the average of one set (A^j_{mean}), the amplitude at a load of 580 N ($A^j_{580\ \text{N}}$), the amplitude at a load of 5800 N ($A^j_{5800\ \text{N}}$), the maximum amplitude of a set (A^j_{max}), and the minimum amplitude of a set (A^j_{min}). All quantities have been normalised relative to the average transmission amplitude around the start of the fatigue loading.
The inset presents the simulated transmitted energy versus average crack size, as discussed in section 5.3.

(minutes)	-5%	-10%	-20%
A_{mean}	82	100	142
$A_{600\ \text{N}}$	130	133	140
$A_{6000\ \text{N}}$	82	98	146
A_{max}	132	135	145
A_{min}	75	83	123

Table 5.1 Observed fatigue durations (in minutes) needed for 5%, 10% and 20% decrease in transmission quantifiers (uncertainty = ± 5 minutes)

section 5.3, it is clear the the rate at which crack develops is not linear. However, a quantitative comparison between both results is not possible because the simulated system is overly simplified.

The performance of a typical off-line linear US crack detection technique was estimated by using the transmission amplitudes of measurements at 580 N. Under the assumption of quasi-static behaviour, these loads were closest to the off-line/out-of-order/in-rest conditions in which regular off-line maintenance inspections are carried out. From here on, this case is is referred to as the in-rest situation associated with the in-rest transmission amplitude. For the in-rest transmission amplitude, a 5% decrease was found after 130 ± 5 minutes, with soon after, a rapid decrease in amplitude for the remainder of the experiment.

Measurements were taken at different fatigue loads, which is characteristic for on-line detection. In on-line-detection, the most straightforward candidate to serve as a defect development quantifier is the average transmission amplitude A_{mean}, since it is susceptible to changes in transmission at a wide range of loads. The average amplitude (black in Figure 5.19) decreased quasi-monotonically with increasing fatigue time. A 5% decrease was found after 85 ± 5 minutes and a 10% decrease after 100 ± 5 minutes. Using the average amplitude A_{mean} is thus more sensitive to the initiating/emerging crack than the in-rest amplitude $A_{580\ \text{N}}$, which could be obtained in a test of the component out of operation. The highest sensitivity to cracks and lowest transmission amplitude was expected for measurements at high-load ($A_{5800\ \text{N}}$), since the cracks are largest at this point in the fatigue cycle. However, at the initial stage of the fatigue experiment the high-load amplitudes were unexpectedly high and even close to the maximum amplitude. From the instance (around 80 minutes) where the fatigue cracks started to significantly reduce the measured transmission, the high-load amplitude decreased rapidly. Nevertheless, the high-load amplitude remained high and was always higher than the average amplitude. This unexpected observation is discussed in section 5.5.4. The minimum amplitude (A_{min}), which was expected to coincide with the high-load amplitude, was the most sensitive parameter. It also had the most stable decrease rate in the time range between initial crack detection (75 ± 5 minutes) and the start of rapid transmission decrease (at 160 ± 5 minutes). A constant decrease rate is of great value when predicting the remaining lifetime. The maximum transmission amplitude (A_{max}) coincided with the low-load/at-rest amplitude from crack detection, until the stage of rapid amplitude decrease.

Overall, a great improvement in 'time of crack detection' was achieved for

all 'on-line'/under load obtained amplitudes (high-load, maximum, average) with respect to the in-rest method (580 N). Until about 55 ± 5 minutes of fatigue, which was 30% of the lifetime of the sample, the transmission amplitude at low-loads were not affected, while these at higher loads were already decreasing. During that period the load on the sample has a significant influence on the reduction of the transmission amplitude.

Transmission amplitudes for different Lamb modes

At the selected frequency (600 kHz) only two Lamb modes exist in a 1 mm aluminium plate: the S_0-mode and the A_0-mode. In these experiments, the influence of defect development on the A_0-mode contribution of the probe wave packets was similar to the above described behaviour of the S_0-mode contribution. The same anomalies between the expected maximum- and minimum-transmission and the observed extreme transmission were found. However, the instance at which the decrease in amplitude started was different for the different modes, as could expected from the simulations in section 5.3. Such differences in sensitivity to cracks, depending on the geometry and the orientation of the crack, could be exploited to design detection algorithms based on the difference between the different modes, or on mode-conversion at the crack site [141].

The effect of the Lamb mode choice was studied by calculating the ratio between the transmitted amplitude of the S_0 and the A_0 contributions of the received wave packets. In order to obtain the transmission amplitudes for the A_0-mode, the experimental data were processed as described in section 5.5.2, but with the time gate set over the A_0-wave packet. Since the transmission amplitudes for both Lamb modes were measured simultaneously, linear changes in the propagation properties of the sample and linear changes of the actuator efficiency and detector sensitivity were filtered out by taking the ratio of both:

$$R^j = A^j_{S_0} / A^j_{A_0} \tag{5.5}$$

In real life applications this provides a great improvement on the long-term stability of the sensing system.

The resulting ratios are plotted in Figure 5.20a. The most interesting features are expected to be found around the instance at which the fatigue damage started to influence the transmission amplitude, which was at around 90 ± 5 minutes. Before this moment, the transmission rates of both Lamb modes are expected to be equal.

The ratios of the average amplitude, the high-load amplitude, and the minimum amplitude, all strongly increase at 80 ± 5 minutes. This indicates that the A_0-mode is more sensitive to small cracks than the S_0 mode, which is in agreement with the simulations in section 5.3 and of which $R^j_{\text{simulation}}$ is presented in Figure 5.20b. It must be noted that the axes of both figures cannot be transformed into each other. During the stage of fast decrease in transmission, which starts at 150 ± 5 minutes for the experimental data and at 75% ± 5% for the simulated data, the S_0 mode transmission decreases fastest. In the experimental case the convergence between both regimes is marked by strong changes in the ratio, and also the results of the final stage do not correspond to the simulated data. These differences are expected to result from crack geometry induced changes in transmission amplitudes, as were simulated for the A_0 in Figure 5.4b.

The combination of the strong increase in R^j, indicating an acceleration in crack development, with the robustness against unwanted linear effects in the sensing system, makes comparison of Lamb modes a very interesting defect indicating parameter.

5.5.4 Amplitude modulation analysis

The transmission amplitude was presumed to be modulated by the size of the crack, which varies along with the load on the sample. In the previous section, unexpected observations about the relation between fatigue load and measured transmission amplitude were made. The transmission amplitude at high-loads was higher than the average transmission amplitude, while it was expected to be close to the minimum transmission amplitude. In this section, it is studied how the periodical load on the sample affects the measured transmission amplitude.

Plots of the fatigue load, the measured transmission amplitudes, and the peak frequencies of the S_0 contribution versus the phase of the fatigue cycle, and a plot of the transmission amplitude versus the load, are shown in Figure 5.21. These plots correspond to different instances in the fatigue process as is indicated in Figure 5.21a. The plots on the left correspond with early crack initiation. These data were acquired within the first 20 minutes of the experiment. The stage of an emerging crack is shown in the middle plots and was measured around 100 minutes into the fatigue process. The points in the right plots were measured 10 minutes before failure, during rapid crack growth.

There is a clear difference between the frequency of the periodic fatigue load

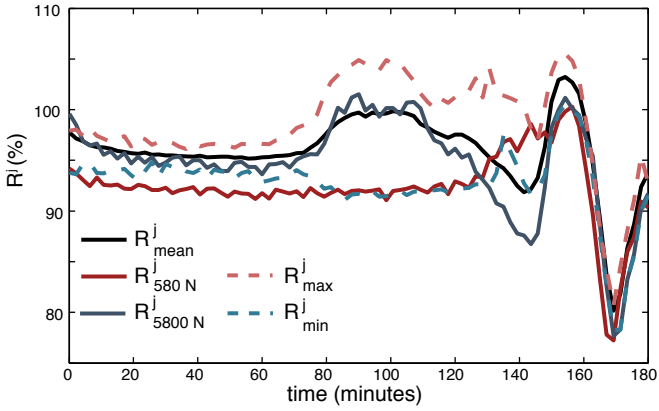

(a) Experimentally obtained ratios of different quasi-static transmission amplitudes.

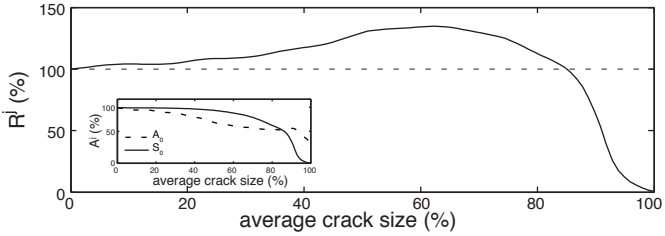

(b) Simulated ratios of the A_0 and the S_0 mode, in correspondence with section 5.3.

Figure 5.20 Ratio between the S_0 and A_0 transmission amplitudes, with $R^j = A^j_{S_0}/A^j_{A_0}$.

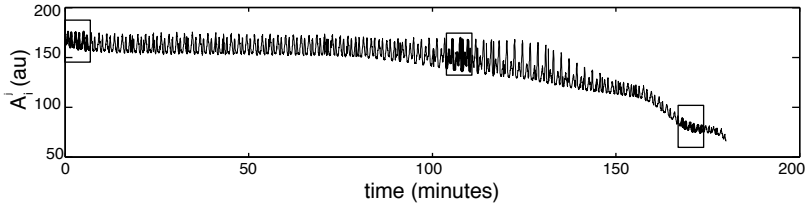

(a) Peak amplitude versus time.

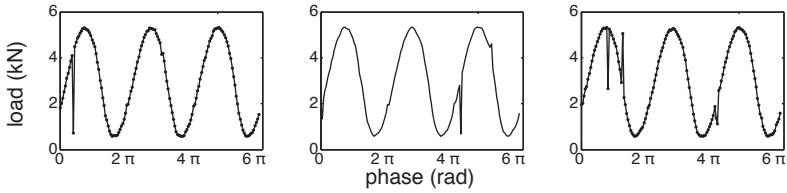

(b) Fatigue load versus phase of the fatigue loading.

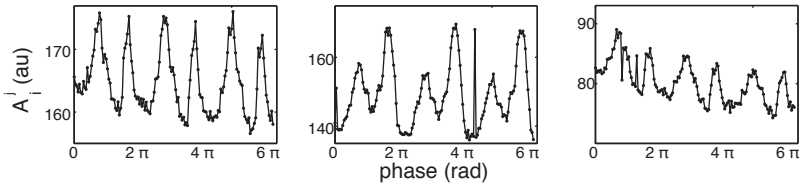

(c) Peak amplitude versus phase of the fatigue loading.

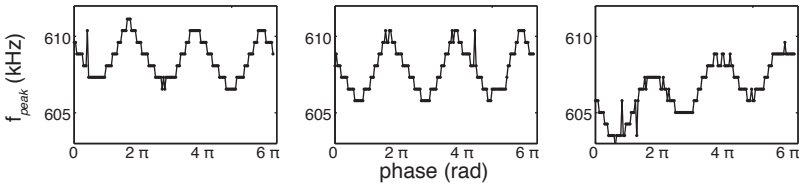

(d) Peak frequency versus phase of the fatigue loading.

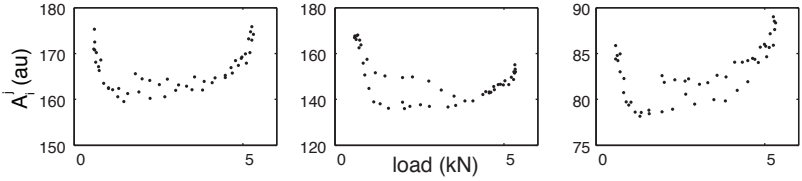

(e) Peak amplitude versus fatigue load for 50 measurements, corresponding to the sampling of one fatigue load cycle.

Figure 5.21 Modulation of different features of the S_0 contribution of the detected probe waves and the corresponding load. From left to right: within the first 15 minutes, after 100 minutes, 10 minutes before failure as depicted by the boxes in the plot (a).

and the frequency of f_{peak}, on one hand, and the modulation frequency of the measured amplitude A_i^j on the other hand. The transmission amplitude appears to reach a local maximum at low loads, which was expected, and a maximum at high loads, which is against predictions, but agrees with the earlier observations. Consequently, these observations are in contrast with the assumption that measured transmission amplitude is lowest at high pulling loads. This unexpected amplitude increase at high loads, results in frequency doubling compared to the fatigue cycle frequency.

The shape of the transmission amplitudes changes while the fatigue crack develops. However, the nonlinear modulation is very complex (Figure 5.21d) and comparison between the load and transmission amplitude does not reveal useful features for the development of crack detection algorithms. The modulation of the peak frequency was of the order of 1%. This modulation is much larger than the Doppler shift induced by the transducers moving away or towards each other, during the cyclic extension of the plate. The latter shift was expected to be less than 0.015% or 90 Hz for fatigue loading at 6 Hz.

Both unexpected effects – a large modulation of the probe wave frequencies, and the frequency of the amplitude modulation being doubled compared to the fatigue loading frequency – are presumed to result mainly from modulation of the sensing system. The actuation and detection efficiency of the respective PZT transducers, is modulated by the applied low frequency vibrations, which not only induce stresses around the defect, but also in the region of the plate where the PZT transducers are mounted. The extension amplitude of the plate was 0.15% ± .05%, which leads to a maximum extension of the PZT transducers of 3 µm ± 1 µm.

The efficiency of a PZT transducer, and thereby of the sensing system, is frequency dependent. A number of geometrically defined resonance frequencies ($f_{\text{resonance}}$) exist and form peaks in the detection or excitation efficiency. In Figure 5.22a the efficiency of a sensing system consisting of a 1.3 mm thick PZT transducer as actuator and a 0.5 mm thick transducer as detector, is presented. This configuration differs from the one used in the experimental data, where two 1.3 mm thick transducers were mounted on a 1 mm aluminium plate. (For a detailed description of the different PZT transducers, refer to section 4.3.1.) In order to test the transmission efficiency of the latter sensing system, a burst of a given frequency and five periods was transmitted between the actuator and the sensor. The sensor response was processed in according to the procedure described in section 5.5.2. A resonance peak is observed at 618 ± 2 kHz and at 1600 ± 20 kHz. It is clear that

a change in frequency leads to a change in sensing efficiency. This effect is indicated by the dashed lines in Figure 5.22a. The mechanical quality factor Q of the sensing system for the peak around 618 kHz is 3.5, which is a lot smaller than the Q factor of the individual PZT transducers, which is 80 [131]. The observed frequency modulation was in the order of 6 kHz. For this sensing system this results in an expected amplitude modulation of 2%, which is close to half the observed modulation.

When designing a sensing system in which frequency modulation is expected, the probe frequency should be chosen in a region where the modulation coefficient is zero. The modulation coefficient is the directional coefficient of the linear relation between the amplitude and the probe frequency and is depicted in Figure 5.22b. It must be stressed that the frequency response, and therefor the amplitude modulation, is strongly affected by the characteristics of the system. The use of different PZT transducers, as was the case here, results in different resonance peaks and different amplitude modulation.

The relation between the amplitude modulation and the frequency of the detected wave packet for the experimental data is depicted in Figure 5.23. As expected, the modulation differs from the modulation of the sensing system depicted in Figure 5.22. The relation between frequency and transmission amplitude explains the frequency doubling observed in Figure 5.21.

A valid explication for the frequency modulation was not found. It can only be expected that it results from nonlinearity in the sensing system induced by the high stresses in the actuator and sensor PZT transducers.

Beforehand, it was assumed that the low-frequency modulation of the actuator PZT transducer would only have a minor influence on the actual amplitude of the emitted probe and that the modulation of the sensor PZT transducer would be filtered out by the high-pass filter and severe frequency modulation was not expected at all. Also, these LF piezoelectric effects due to the extension of the plate were expected to be linear, or at least monotonic, with the extension of the plate. The experimental observations suggest that these assumption were (partially) incorrect and that measures had to be taken in order to avoid nonlinear modulation of the sensing system. The results of this modification are discussed in the next sections.

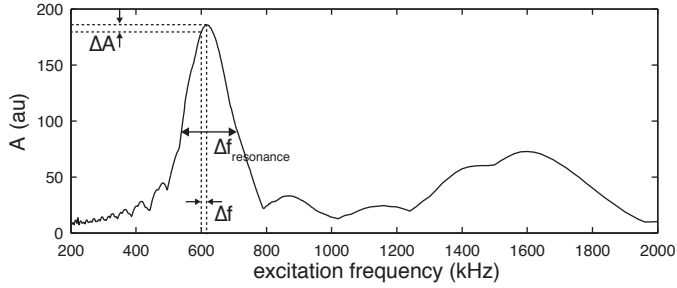

(a) Transmission amplitude versus excitation frequency.

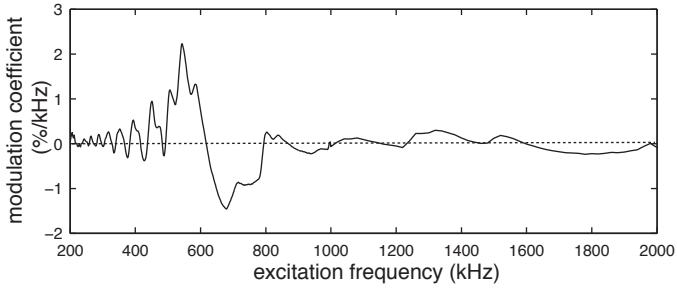

(b) Modulation coefficient versus excitation frequency.

Figure 5.22 Transmission efficiency and corresponding amplitude modulation in a not vibrating 1 mm aluminium plate. Probe waves of variable excitation frequencies were transmitted between an actuator and a sensor.

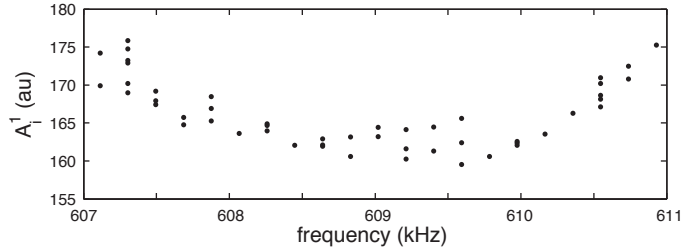

Figure 5.23 Transmission versus measured frequency in one set of measurements of a fatigue loading experiment

5.5.5 Concluding remarks on the experiments using an aluminium plate as sample.

Using 1 mm aluminium plates as samples, a test setup was developed and validated. An extensive set of samples was used to improve the configuration of the setup. A probe signal was chosen in order to allow time-separated arrival of the S_0 and A_0 Lamb modes in order to allow mode selection. Changes to the triggering were made to ease analysis of the transmission amplitudes versus the applied load. LabVIEW software to control the experiment and to save the measurements was developed.

Steady-state ultrasonic crack detection ($A^j_{5800\ \mathrm{N}}$, A_{min}) was achieved and proven to be more sensitive than in-rest crack detection ($A^j_{580\ \mathrm{N}}$). The selection and comparison of different Lamb modes proved to be successful and to allow for the estimation of defect size.

The proposed nonlinear ultrasonic crack detection, in which low frequency vibration is compared to transmission of high frequency probe waves as depicted in Figure 5.21e, could not be performed. This was due to the large nonlinear modulation of the PZT transducers by the, load induced, extension of the plate. In real life applications, the PZT transducers should be chosen and placed so they do not undergo nonlinear modulation induced by the vibrations of the system. Placing them in stress nodes of thicker sections of the component, where deformation of the transducer is within the linear working range of the transducers. PZT materials should be specifically selected to operate under the expected stress and deformation conditions. In order to meet these conditions a new sample in which the PZT transducers were placed in a low-extension region was created.

5.6 Crack detection in an aluminium structure

In order to obtain the results presented in this section, the same setup, sensing system, and signal processing as described in the previous section were used. The sample was adapted to address the issues of nonlinear modulation of the sensing system due to fatigue loading (cf.section 5.5.5). The effect of the adoptions made to the sample were verified and the performance of the analysis of the quasi-static load transmission was validated. Under these circumstances, defect detection algorithms, exclusively based

on vibration induced nonlinear modulation of probe waves by the defect, could be developed.

In line with the previous section, the results of one experiment are used to illustrate the general findings. Unless explicitly stated, the discussed observations hold for all experiments performed on this type of sample.

5.6.1 Geometry of the sample and fatigue loading experiment

As discussed in section 5.5, fatigue loading of 1 mm aluminium plates resulted in large nonlinear effects in the PZT transducers. The measured transmission amplitude was heavily modulated, even for intact samples. This modulation — considered to be a combined effect of modulation in excitation and in detection — was the result of extension of the region where the transducers were placed. In order to address these issues, a 6 mm aluminium bar was chosen and a central plate-like defect region was created by reducing the thickness to 1 mm over 90 mm, as illustrated in Figure 5.26

The sample was equipped with 2 PZT transducers, identical to those used on the 1 mm plate samples in section 5.5.1, but since they were placed on a thick section of the sample, the transducers could be expected to undergo much less extension strain. The probe signals were kept identical: 600 kHz, 5 cycles, and 50 $\pm$ 1 V. The fatigue loading was slightly increased to a sinusoidal load between 600 N and 6000 N. Due to the different type of aluminium, the sample-life increased to (125 $\pm$ 10) 10^3 cycles, which took 360 ± 5 minutes when loading at 6 Hz. The evolution of the defect followed typical fatigue crack behaviour, as discussed in section 5.5.1, but crack initiation took much longer than with the previous type of samples.

In the presented experiment, 211 sets of 50 measurements were collected and a 212^{th} set of 25 measurements, after which the sample broke. An overlaid plot of the loads for al measurements is shown in Figure 5.24. This illustrates that the measurements were uniformly distributed over the fatigue loading cycle except for a small number of 'false triggers', which can be recognised as downward spikes.

Responses of the sensor, the applied time gate, and the gated results are presented in Figure 5.25. Due to the complex geometry of the sample, with reflection and mode conversion occurring at the thickness steps between the transducers and the crack region, the wave packets were very complex. It was therefore no longer possible to differentiate between different Lamb

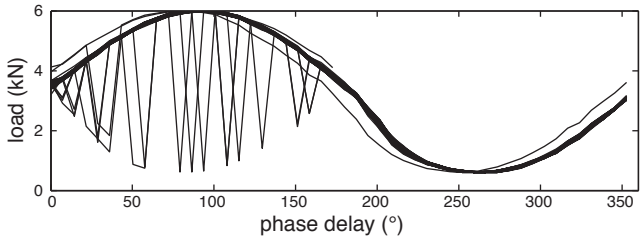

Figure 5.24 Overlaid plot of the applied fatigue load versus phase of to the fatigue loading cycle for 212 sets of 50 measurements.

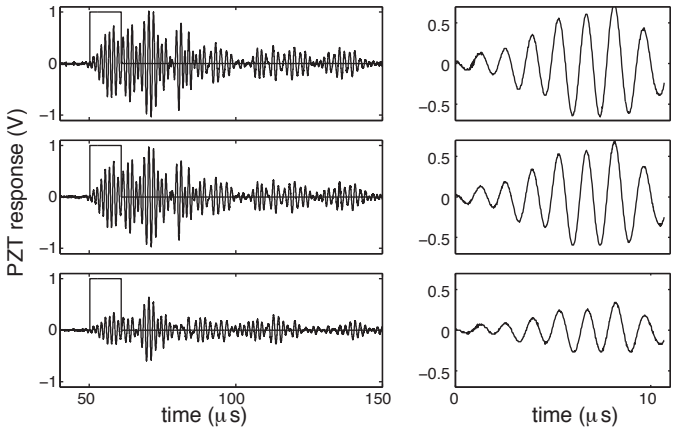

Figure 5.25 Left: Three high-passed PZT responses at different stages of the fatigue loading (top: begin; middle: middle; bottom: end) of the 6 mm aluminium sample and the selected time gate. Right: The same response after time gating.

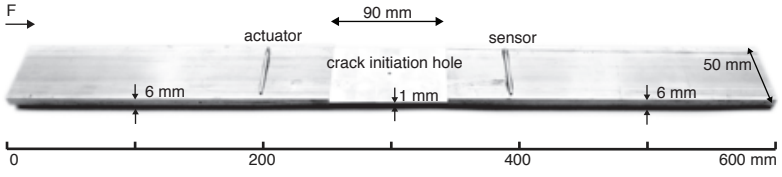

Figure 5.26 An intact 6 mm aluminium bar with a 1 mm thick crack susceptible region .

modes and thus Lamb mode selective detection, as in section 5.5.3, could not be achieved. The time window was chosen so that only the earliest arriving waves were processed. In real life applications this would be the best option in order to avoid the influence of modulated reflections, which arrive later due to having traveled over a longer distance. In this laboratory environment the use of a longer time gate had only a weak influence on the calculated transmission amplitudes. Nevertheless, the short time window was preferred since it fits better in the proposed time gating philosophy. The transmitted amplitudes were calculated as in expression 5.3 using the gated response.

5.6.2 Steady state ultrasonic analysis

In analogy with the analysis of the steady-state transmission in the plate-sample, presented in section 5.5.3, the average amplitude (A^j_{mean}), the maximum amplitude (A^j_{max}), the minimum amplitude (A^j_{min}), the high-load amplitude ($A^j_{6000\ \text{N}}$), and the low-load/in-rest amplitude ($A^j_{600\ \text{N}}$) are obtained and the results are presented in Figure 5.27. Table 5.2 lists the time at which the amplitude reached a decrease of 5%, 10%, and 20%. In this experiment, the transmission amplitude measured at loads around 600 N were used to represent the case of in-rest detection, typically taking place when the component is out of service and under low-loads.

During crack initiation, i.e. while a non-propagating crack is formed due to fatigue loading, a smooth decrease of 1.25±0.03% per hour for all parameters of transmission amplitude is observed. A decrease of 5% is achieved after 4 hours, hence 10% a decrease was more suitable as reference for significant local decrease indicating an emerging crack.

The in-rest amplitude $A^j_{600\ \text{N}}$, which is comparable to the amplitudes measured in traditional ultrasonic transmission measurements performed while the component is out of order, decreased 10% in 303 ± 5 minutes. In accordance with section 5.5.3. The other defect transmission amplitudes were considered on-line detection since they correspond to measurements in operational conditions. For this sample the difference between A^j_{max} and between $A^j_{600\text{N}}$, and A^j_{min} and $A^j_{6000\text{N}}$ was small. The average amplitude was close to the average of the extremes, but became somewhat lower as soon as crack formation became detectable. A decreased 10 % is noted after 261 ± 5 minutes for the amplitude of the high-load ($A^j_{6000\ \text{N}}$) and after 272 ± 5 minutes for the average amplitude. As described in section 5.5.3, due to load induced crack opening and therefore crack impedance contrast

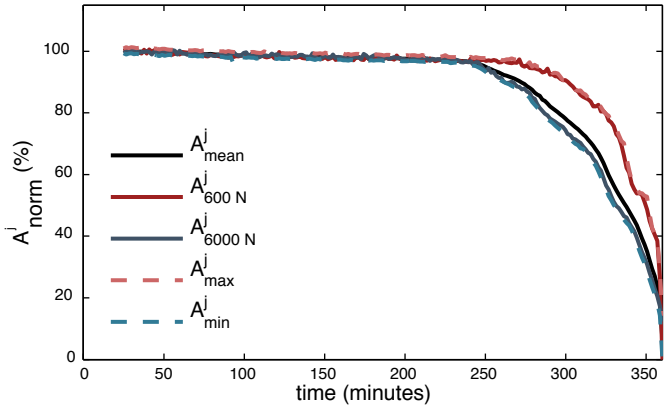

Figure 5.27 Normalised transmission amplitudes versus fatigue loading time, with A^j_{norm} calculated as: the average of one set (A^j_{mean}), the amplitude at a load of 600 N ($A^j_{600\ \text{N}}$), the amplitude at a load of 6000 N ($A^j_{6000\ \text{N}}$), the maximum amplitude of a set (A^j_{max}), and the minimum amplitude of a set (A^j_{min}). All quantities have been normalised relative to the average transmission amplitude around the start of the fatigue loading.

(minutes)	-5%	-10%	-20%
A_{mean}	248	272	295
$A_{600\ \text{N}}$	275	303	325
$A_{6000\ \text{N}}$	250	261	287
A_{max}	270	297	325
A_{min}	249	267	288

Table 5.2 Observed fatigue durations (in minutes) needed for 5%, 10% and 20% decrease in transmission quantifiers (uncertainty = ± 5 minutes)

enhancement, the analysis of the general evolution of the transmission amplitude turns out to be more sensitive when the sample is inspected in under-load conditions than in in-rest.

5.6.3 Nonlinear modulation based diagnostic algorithms

In the following, the nonlinear modulation of the transmission amplitude, due to low-frequency vibration of the fatigue cracks is studied, in order to develop diagnostic algorithms to analyse if damage is present.

Five quantitative parameters describing the state – healthy or damaged – of the sample were developed. The goals set in the introduction of this chapter (section 5.1), regarding these parameters were: simplicity, unambiguity, online applicability and reference-free operation.

Shape analysis

In order to analyse and illustrate the influence of the crack on the transmission amplitudes, and to check if PZT-induced nonlinearity was reduced, Figure 5.28 shows results at different stages of the fatigue process: on the left, data measured during crack initiation, in the middle data in an early stage of a detectable crack, and on the right data during rapid crack growth.

The frequency doubling noted for the 1 mm sample has disappeared and all modulation takes place at the fatigue loading frequency of 6 Hz. The modulation of the peak frequency has decreased to 0.2%, which is still much larger than the expected Doppler shift. The peak frequency itself has shifted to 700 ± 5 kHz. Given the substantial loading-induced probe wave frequency modulation, the choice of transmission amplitude quantification method, as described in section 5.5.2, is important. Methods based on a fixed frequency, e.g. lock-in detection, using the excitation frequency as reference signal, would result in apparent, frequency modulation induced, amplitude modulated effects.

The amplitude modulation of the measured transmission amplitudes in the intact sample (Figure 5.28b, left) was in phase with the fatigue loading. This contradicts the theoretical assumption that for an intact sample the measured transmission is independent of the applied loads and thereby illustrates that the measured transmitted amplitudes were still affected by more than only mode conversion at the crack. It is likely that the new

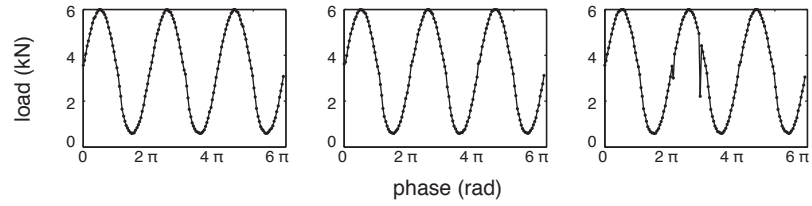

(a) Fatigue load

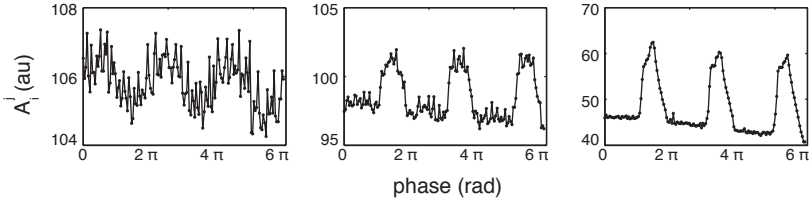

(b) Transmission amplitude

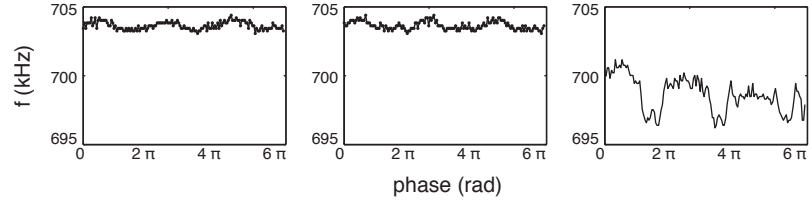

(c) Peak frequency

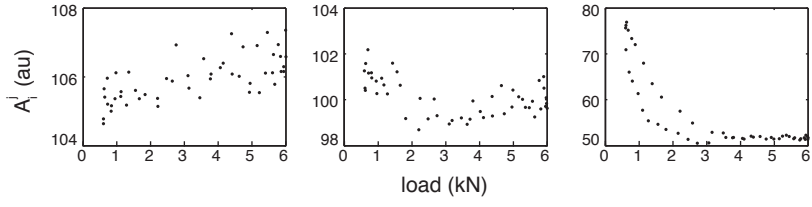

(d) Transmission amplitude versus load

Figure 5.28 Fatigue load, transmission amplitude, and the peak frequency versus phase of fatigue loading (150 points in every plot) and transmission amplitude versus load (50 points in every plot). From left to right: within the first 15 minutes, after 253 minutes, 20 minutes before failure.

placing of the transducers did not entirely eliminate the modulation of the PZT transducers. Changes in time-of-flight of the probe wave packets, due to the extension of the plate, could also act as a modulation source. Also physical properties, such as the density and the longitudinal- and shear-wave velocity, could be affected by loading the sample. The combination of all these effects resulted in frequency and amplitude modulation in the intact sample. However, the modulation depth is merely a few multiples of the noise on the data, which is quite small.

The transmission amplitude during early detectable crack development (Figure 5.28b and 5.28d, middle) was modulated by about ±5%. The depicted measurements are those where the modulation of A_i^j became obvious and where the transmission amplitudes and loading started to behave as expected by the simulations made in section 5.3. At high loads, a considerably smaller transmission amplitude is observed than at low loads. The transmission amplitude shows clipping-like behaviour for transmission at high loads. The load where clipping starts to occur, is called the cut-off load. Above a certain load the transmission amplitudes reaches a fixed minimum value, which decreases with time, which corresponds with observations made during analysis using steady state transmission features in section 5.6.2. At loads below the cut-off load, transmission amplitudes were load dependent and exhibited asymmetrical properties, invalidating the earlier assumption that the measurements were performed under quasi-static conditions. This asymmetry is most notable in the transmission amplitude versus load plots of the rapidly growing crack (Figure 5.28d, right).

The load dependence of the transmission amplitudes of the crack in an evolved stage (Figure 5.28b and 5.28d, right) exhibits similar features as observed fpr a developing crack: clipping occurs at high loads and asymmetric load-dependent transmission amplitudes at lower loads. At this point the amplitude modulation depth has significantly increased to 60% and the frequency modulation to ±0.6%.

The transmission amplitude versus load relation is determined by a combination of different features, of which the importance shifts as the fatigue crack evolves. A schematic interpretation is presented in Figure 5.29.

In an intact sample, the only source of amplitude modulation is considered to be the sensing system. In the left plot in Figure 5.29 the modulation in an intact sample is depicted. Although high-pass filtering of the PZT response removes the low frequency modulation, amplitude modulation of the high frequency probe waves is still observed. Therefore the 'intact sample' modulation represents the baseline modulation and is due to the PZT

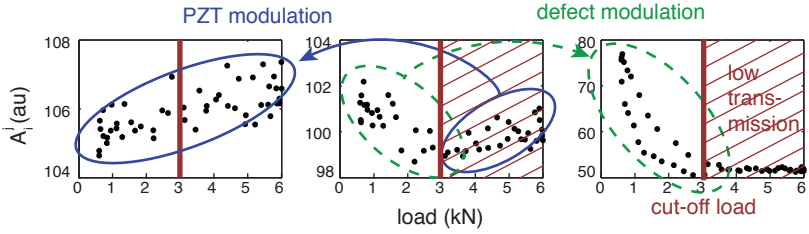

Figure 5.29 Combined transmission amplitude modulation by varying load. From left to right: within the first 15 minutes, after 253 minutes, 20 minutes before failure. This Figure corresponds to Figure 5.28d.

transducers in the sensing system.

The interaction of probe waves with a crack can be classified into two load regimes. At loads above the cut-off load, a fixed minimum transmission amplitude is observed, corresponding to the red shaded area in the left plot of Figure 5.29. Above the cut-off load the influence of the fatigue cracks on the transmission amplitude appears to be at its maximum. Consequently, changing the load within this region does not lead to modulation of the transmission amplitude. This can be understood as the crack impedance remaining constant once the crack is full open. The cut-off load can be expected to be dependent on the geometry of the crack and therefore to change when the crack develops. However, no consistent evolution of the cut-off load during the fatigue experiment was detected. Below the cut-off load the transmission amplitudes were dynamically modulated by the applied load, as was predicted by the simulations in section 5.3. Since the sample was severely damaged at this stage, the observed modulation, in both load regimes, was considered to be predominantly defect-related.

The middle plot of Figure 5.29 depicts the transition between predominantly PZT-related modulation and the defect induced modulation. Below the cut-off load, the effect of defect-related modulation is larger than the effect of PZT-related modulation. Hence, the net outcome of the combined effects is a decrease of transmission amplitude. Above the cut-off load the influence of the fatigue crack is manifested as a steady decrease. At the selected instance/crack-size the fixed decrease in amplitude was still in the order of the increase in transmission amplitude due to PZT-related modulation and this is clearly visible in the sum of both effects.

In general it can be concluded that the adapted sample was much more robust against non-defect-related modulation and that comprehensive two-regime modulation by the fatigue cracks is observed. The peak frequency

modulation is low and the sensing system-related modulation of the transmission amplitudes is limited, linear and comprehensive throughout the sample life. The developing crack induces a load dependent decrease of the measured transmission amplitudes. At low loads decreasing transmission for increasing load is observed while at high loads the minimum transmission amplitude is constant. Other observations include a decrease in transmission that stops at a cut-off load, in which the cut-off load did not seem to be related to the state of the damaged sample, and the transmission amplitudes at low loads being asymmetric with respect to increasing or decreasing load. As longs as the applied loads remain below the observed cut-off load, a linear load-amplitude relation can be expected. By recognising these features, a trained person or AI algorithm could detect crack-induced modulation. The next step is to exploit these observations to define diagnostic algorithms that use quantitative parameters, allowing unambiguous crack detection whit a minimum need for human interpretation of data.

Correlation analysis (CA)

The initial idea when developing this NDT technique was to evaluate the correlation between the load on the sample and the corresponding transmission amplitude, in order to determine the health of the sample. A negative correlation is expected when damage is present, since the transmission amplitude decreases with increasing load. In the case of an intact sample it was expected that the load and the transmission would be uncorrelated. Due to modulation of the PZT transducer response in the sensing system, load dependent modulation of the transmission amplitudes is observed in the experimental data, implying a positive correlation.

In the previous section it was concluded that the effect of the load on the transmission amplitudes consists of two regimes, one in which the load and transmission are linearly dependent and one in which the transmission amplitude is at a load independent minimum value. The correlation is thus expected do depend predominantly on the latter regime. Using Pearson's linear correlation coefficient [142], the correlation between the transmission amplitude and the load was calculated for all the data, and for the reduced data set that only included points measured at an applied load smaller than a cut-off load of 3300 N. The results are presented in Figure 5.30.

For both cases a sharp transition, with high contrast, of the correlation takes place after around 240 ± 5 minutes, with the correlation for the measurements taken at loads below the cut-off load decreasing two to five minutes

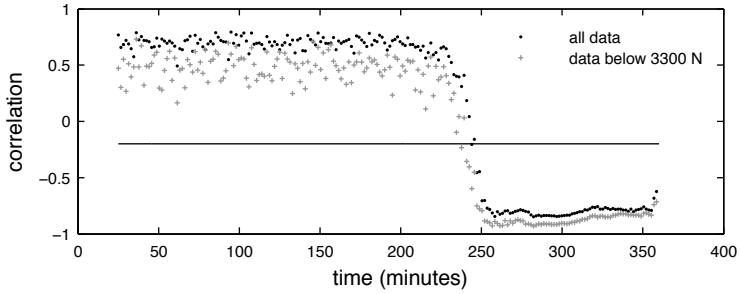

Figure 5.30 Correlation between the transmission amplitude and the applied load, calculated using all data (black dots) or calculated using data points measured at a load below 3300 N (grey crosses) versus time.

earlier. With the correlation calculated using all data, an initially positive linear correlation is observed but as the crack initiates and starts to emerge the correlation becomes negative. The correlation calculated with reduced data is initially lower, when the effect of the damage becomes significant, it decreases and follows a similar evolution as the correlation calculated with all data. As expected the correlation of the reduced data tends most to the simplified case of a correlation coefficient -1.

Automated diagnoses could simply be done by comparing the correlation with a threshold value. The properties of the monitored component have to be taken into account, when defining the threshold value. In the present case a high correlation is found for both methods of calculating the correlation. The threshold was chosen to be -0.2, which results in detection at 240 ± 5 minutes for both methods. When calculating the correlation using all data, the deviations on the correlation are relatively small and a high contrast between intact and damaged is observed. Therefore the actual threshold value can be varied between 0.5 and -0.7, which makes this method very robust for this sample. When the correlation is calculated using the reduced data the threshold should be between 0.1 and -0.8, again a wide range resulting in robust detection. Setting the threshold to a value outside this detection range or changing the initial and final values of the correlation would result in false detection or no detection of damage. However there is little or no reason to set the threshold values outside this range. More problematic would be the occurrence of continued limited correlation in the damaged state. In that case, increasing the number of measurements could offer a solution. During damage detection in real life applications, where crack growth is not expected to evolve on a timescale of minutes, it is always advised to perform additional measurements, using more samples, in order

to confirm the damaged state of the component.

An important requirement for the proposed technique is a sensitive device to measure or estimate the load on the sample. In one of the experiments, an uniaxial accelerometer was used and the output had a phase shift to the actual load. Using these results, without correction for the phase shift, results in permanent low correlation and thus the damage cannot be detected.

The proposed method is quite insensitive to changes in wave propagation properties caused by environmental changes. The highest threat comes from potential (nonlinear) modulation of the sensing system and the load measurement. In that case analysing the correlation between amplitude and differentiation between negative correlation resulting from sensing system related modulation or defect induced modulation is not reliable.

Modulation coefficient of transmission amplitude versus load analysis (MCA)

The degree of correlation as such, provides very limited information about the relation between the load and the transmission. In the case of negative correlation between not-defect-related amplitude modulation and applied load, the latter cannot be differentiated from modulation induced by emerging defects by analysing correlation data. The modulation coefficient (MCA) is defined as the direction coefficient of the linear fit of the transmission amplitude as a function of the applied load. Therefore it can be used to further interpret the calculated correlation and besides, it can be used, in certain circumstances, as a detection parameter on its own. Again, accurate knowledge of the load for every measurement is necessary.

When calculating the modulation coefficient, the absolute values of the transmission amplitude have a large influence on the interpretation, which makes these results very sensitive to environmental changes as discussed in section 5.1. In order to address this drawback, it is convenient to normalise and scale the transmission amplitudes between zero and one within every set of 50 measurements:

$$A^j_{i,norm} = \frac{A^j_i - A^j_{\max_5}}{A^j_{\max_5} - A^j_{\min_5}} \tag{5.6}$$

with $A^j_{\max_5}$ and $A^j_{\min_5}$ the average of the five respectively maximum or minimum transmission amplitudes. The normalised data is shown further on, in the top plot of Figure 5.34. The modulation coefficient was calculated

by fitting the normalised transmission amplitude as a linear function of the applied load. Again, results are given for the modulation coefficient calculated using all data and for modulation coefficient calculated using the, previously defined, reduced data (MCBCOA).

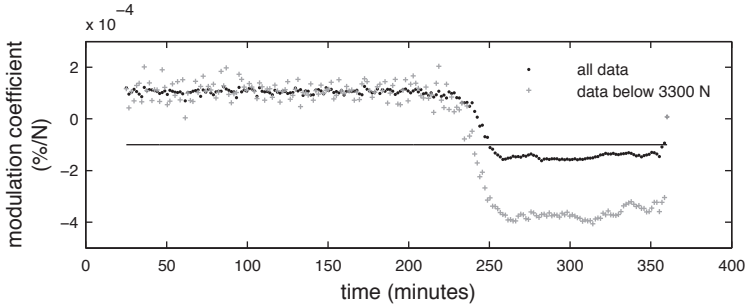

Figure 5.31 Modulation coefficient of the normalised transmission amplitudes as a function of applied load, calculated using all data (black dots) or calculated using data points measured at a load below 3300 N (grey crosses), versus time.

In Figure 5.31, two clear transitions, indicating the presence of fatigue damage, are observed. This approach has a comparable sensitivity as correlation-based diagnoses. However, when not-defect-related baseline modulation induces strong negative correlation, damage cannot be detected by using a shift in correlation. In contrast, by analysing the modulation coefficient, defects can be detected as long as the defect-related modulation coefficient has a significant influence on the total modulation coefficient.

In order to apply this method, the modulation coefficients in intact and damaged conditions need to be stable and known in advance in order to define a threshold value. For the here investigated sample, a threshold of -10^{-4} was chosen. This resulted in detection at 250 ± 5 minutes and 240 ± 5 minutes, for modulation coefficients calculated respectively using all data and reduced data. The choice of the threshold value is very critical, especially when calculating the modulation coefficients using all data. Since the relation between the transmission amplitude and the load is only expected to be linear below the cut-off load (cf. Figure 5.29), the use of only the reduced data is preferable. In practice the choice of the cut-off load could be made by calculating the correlation while varying the cut-off load. Whereby the cut-off load resulting in the highest correlation could be selected. An other option would be to choose a substantially low cut-off load value for which the relation between transmission and load would always be linear. In the case of a lower loading amplitude a fully linear

relation is expected making the cut-off approach unnecessary. Using the reduced data results in a high contrast transition from positive modulation coefficients, in the order of 10^{-4}, to values around $-4\,10^{-4}$. Changing the reference value, within the transition range between initial and final modulation coefficients, has only a limited influence on the instance of detection. A change outside this, limited and experimentally defined, range would lead to complete malfunctioning of the diagnostic algorithm.

As a result of the normalisation, this method remains very stable when the propagation amplitudes change linearly and has good sensitivity in time. Its main weakness is the need for known/expected values of the initial and final modulation coefficient of the transmission amplitude as a function of the load, and the severe consequences if one of both drastically changes due to inadequate calibration values. This technique cannot be considered to be reference-free. But in components where the modulation coefficient is proven to be constant for the intact sample and much lower in the case of damage, the approach is quite promising.

Modulation depth analysis (MDA)

Due to the variable load on the sample, it was possible to perform measurements at different crack sizes, and modulation of the transmission amplitude, corresponding with the simulations in section 5.3, is observed. According to these observations and previously mentioned simulations, the modulation of the size of the crack and its corresponding mode conversion are not linearly proportional to the applied load and neither is mode conversion linear to the crack size. However, from previous observations in this section it was concluded that the modulation depth of the transmission amplitudes increases with the average degree of fatigue damage. Therefore the modulation depth is a promising parameter to evaluate the health of the sample.

Calculating the modulation depth using the absolute values of the transmission amplitudes has identical problems as the classic techniques analysing the general evolution of the transmission amplitude. As described in section 5.1, uncontrolled, not-defect-related changes in propagation properties or to the sensing system, would make the results useless. In order to remove the dependency on the absolute transmission amplitudes, the data were normalised by dividing every measurement by the average transmission amplitude of its set:

$$A^j_{i,norm} = A^j_i / A^j_{mean} \tag{5.7}$$

This normalisation partially removes the need to have available reference measurements of the vulnerable transmitted amplitude and it filters out global not-defect-related fluctuations in transmitted energy. The normalised transmission amplitudes are shown in the top plot of Figure 5.32. The standard deviation of the normalised transmission amplitudes within one set was used as the parameter for the modulation depth (MD^j):

$$\mathrm{MD}^j = \mathrm{std}(A^j_{i,norm}) \tag{5.8}$$

The results are shown in the bottom plot of Figure 5.32. The beginning of detectable crack development occurs after 250 ± 5 minutes, which is comparable to the steady-state detection in section 5.6.2. The onset is marked by a sharp increase of the modulation depth. The modulation depth monotonically increases in the early stage of the detectable crack. At the end stage non-monotonic behaviour takes place. This reflects the strong decrease in amplitude at low loads, as in Figure 5.27, and indicates that the sample was severely damaged.

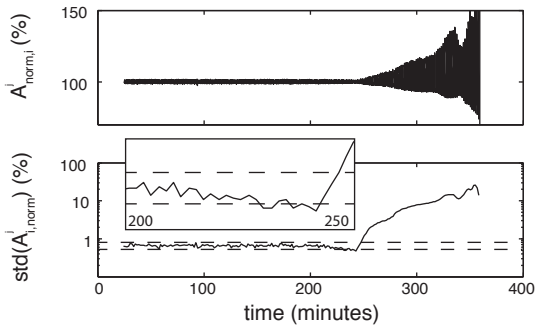

Figure 5.32 Normalised transmission amplitude (top) and corresponding modulation depth calculated as the standard deviation of the normalised transmission amplitude (solid, bottom) with error lines for the original modulation depth (dashed, bottom), all versus time.

The modulation depth of the transmission amplitudes differs with a very high contrast between the undamaged state and the damaged state. Its value doubles between 250 ± 5 minutes and 260 ± 5 minutes and triples compared to its original value. In this interval the transmission decrease detected by at-rest transmission analysis was less than 10%. It is worth noting that the modulation depth significantly decreases before it started to significantly increase. The dashed lines correspond with the error – calculated as three times the standard deviation – on the values of the demodulation depth at the start of the experiment. The decrease in modulation depth

occurs because the PZT-related modulation of the transmission amplitude is in phase with the fatigue loading, while the defect-related modulation has the opposite phase (Figure 5.28b). At the beginning of the crack detection these effects cancel out and, in two out of the three performed experiments, a significant decrease in transmission amplitude is observed. These results are in correspondence with the work of Vanlanduit et al. [138] on crack detection in a rod, using Rayleigh waves as probe waves.

In the third experiment the sample was loaded at a higher frequency, resulting in a shorter duration of the instance where both effects are of comparable order. This could explain why this effect was not measured. These structure-specific effects can thus be used to detect cracks in an even earlier stage. In this test, modulation depth based defect detection would have detected the start of a crack 20 ± 5 minutes earlier than high-load transmission amplitude analysis (cf. section 5.6.2). Figure B.5 in Appendix B illustrates these differences.

As threshold value, the initial average modulation depth, increased with three times the initial standard deviation on the modulation depth, was used. This results in recognition of the damage state of the sample after 249 ± 5 minutes. An increase of the threshold value, within the same order of magnitude, results in later detection of the crack formation.

This approach is very successful when the modulation depth scales linearly with the transmission amplitude. A high increase of the modulation depth allows for unambiguous defect recognition. The largest drawback of the method is that the assumed linear relation might not hold. Also, a reference value of the initial modulation depth of the probe waves is required. The drastic increase of the standard deviation reduces potential problems due to changes in modulation depth of an intact sample, but the need for a reference modulation depth is still there.

High transmission load analysis (HTLA)

The accurate knowledge of the load on the sample can also be used to monitor differences in the transmission behaviour of the sample. In theory the transmission amplitude of an intact sample is constant and thus independent of the applied load. Nevertheless, Figure 5.28b illustrates that in practice both are correlated and, using the current type of sample, in phase. Here, the load levels at which the maximum transmission amplitudes were measured were above average for an intact sample and these

loads are always expected to be below the average load for a damaged sample. In summary, the load at which the highest transmission amplitude is measured changes throughout the experiment and is a good indicator for the presence of fatigue damage.

The 'high-transmission loads' in Figure 5.33 were calculated by taking the average of the loads corresponding to the five highest transmission amplitudes for every set of 50 measurements. Averaging improves the robustness of the technique compared to using the load corresponding to the absolute maximum transmission amplitude.

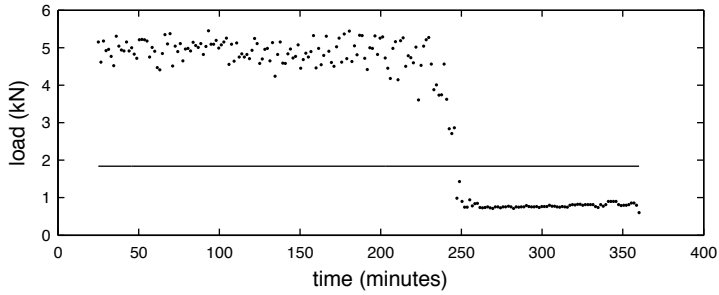

Figure 5.33 Average load of the 5 highest transmission amplitudes.

A strong transition around 250±5 minutes is observed. The high-transmission loads before the transition have a large variance. This indicates that for high transmission amplitudes the relation between the load and the actual value of the transmission amplitude is rather weak, causing a high noise level. This was also observed in the plots in Figure 5.28. In the damaged sample the highest transmission amplitudes were measured at low loads and were less scattered, which corresponds to expectations.

As a reference value twice the lowest load in every set was used. In situations of varying load on the component, the average of the current set could be used. Using more measurements in one set decrease the variance on the results and a threshold close to the minimum observed load can be used.

In practice this method is more robust than analysis of the evolution of steady state transmission amplitudes, since changes in probe excitation or transmission amplitude measurements over longer timescales do not have an influence on the outcome. The drawback is that accurate knowledge of the load, or a related parameter, is necessary.

Median transmission analysis (MTA)

The measured data have a uniform distribution over the phase of the fatigue loading. The measured loads are thus symmetrically distributed, with a high probability towards high and low loads. In an intact sample, where the load and transmission amplitude are expected to be linear, the median A^j_{median} should be the close to the average A^j_{mm} of the maximum and minimum transmission amplitude. When the relation between load and transmission amplitude becomes nonlinear, the distribution of the transmission amplitudes changes, which should lead to deviations between A^j_{median} and A^j_{mm}.

To calculate the median A^j_{median}, the same normalisation as used when calculating the modulation coefficient, given by expression 5.6 was used. The resulting transmission amplitudes are depicted in the top part of Figure 5.34.

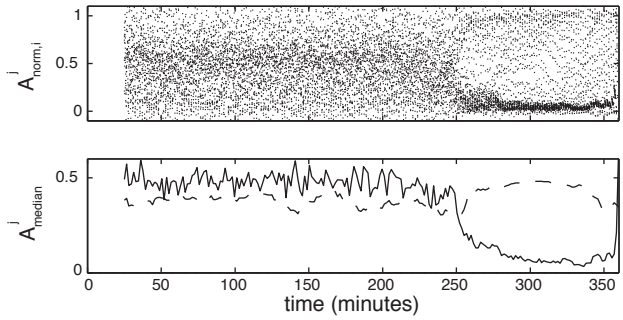

Figure 5.34 Normalised transmission amplitudes (top), median of the normalised transmission amplitudes (solid, bottom) compared to three times the local standard deviation of the median transmission amplitude (dashed, bottom).

The median of the normalised data were calculated and compared to the expected median of 0.5 for an intact sample. As can be observed from scatter plot in the top panel of Figure 5.34 transmission amplitudes for an intact sample are symmetrically distributed. In contrast, transmission amplitudes in a damaged sample are not symmetrically distributed. The difference between the high-load range with fixed low transmission and the below cut-off load range with load dependent transmission is very clear in the scatter plot. Accordingly, the median is decreasing when a crack forms (Figure 5.34, solid, bottom).

In order to provide automated interpretation of these results, a threshold level was defined as three times the local standard deviation of the high fre-

quency changes of the median. If the difference between the expected value of 0.5 and the median was more than the local threshold value, the sample was considered damaged. For the short and faster loaded sample a larger standard deviation on the median is observed. This was partially due to not uniformly distributed sampling, causing a broader transition between 'intact' and 'damaged'. In real life, where the structure is not expected to break in a matter of hours, confirmation measurements could be performed when a 'compromised' state is reported. This would improve the robustness of the outcome. When multiple measurements can be obtained at one state of the crack, the standard deviation used to calculate the reference level can be locally calculated, improving the detection sensitivity, and making this diagnostic algorithm smarter than most others. The approach resolves most of the remaining issues of the other techniques, such as reference dependence, linearity requirements, etc. It is therefore the most robust and general applicable solution.

Other diagnostic algorithms

A number of other diagnostic algorithms were considered or presented in literature. A list of options and their main drawbacks is presented:

- Frequency analysis on the transmission amplitude as function of the phase in the fatigue cycle, could be performed. In practice a Fourier transform of a number of sampling cycles, as depicted for three cycles in Figure 5.28b would be calculated and the amplitude and phase could be used. On one hand, the shift in phase at the transition from sensing system related in phase modulation to defect-related out of phase modulation would reveal the presence of damage. Second the higher harmonics are expected to change. Both effects are present in the discussed sample and have good sensitivity and contrast. Nevertheless they cannot be considered applicable for most real life applications. They are strongly dependent on cyclic behaviour of the loading and of adequate sampling thereof, which in is not available in most situations.
- Neural network recognition of normalised spectra could be trained in order to recognise patterns within one experiment. However, applying the obtained network to data from other experiments did not result in successful diagnoses of the sample.
- Detection of higher harmonics of the probe frequency is the most common approach in nonlinear ultrasonics. Here this approach cannot be

used because of the probing signal and time gating. The detected waves are Lamb waves they are dispersive. Waves with a higher harmonic frequency travel at different group velocities than the probe waves and are filtered out by time gating.

5.7 Automated defect detection algorithms

In the two previous sections, a number of methods to quantify the health of the different samples were defined. In this section they are recapitulated. The goal of these methods is to convert every set of 50 measurement, which have been collected during the fatigue loading process, to one single value. This defect development quantifier can than be compared with a threshold value, in order to decide if a sample is healthy or not. The performances of these different defect diagnostic algorithms for different samples are compared.

In the following, a summary of the different sample health evaluation schemes is presented, for a detailed description refer to sections 5.5.3, 5.6.2 and 5.6.3.

- General evolution of $A^j_{\text{in-rest load}}$ analysis (GEIRA):
  In this approach, the transmission amplitude is measured when the component is out of operation (in-rest). In the performed fatigue experiments this measurement was replaced by a measurement at the lowest load, which was close to 600 N. The transmission amplitude is expected to decrease with increasing damage. As threshold a fixed value of 95% of the initial transmission amplitude was used. This value was significantly lower than the transmission amplitudes around the instance when the general decrease in amplitude started, but high enough to provide sensitive crack detection. This diagnostic algorithm is highly sensitive to environmental changes, which can affect the transmission amplitude.

- General evolution of $A^j_{\text{high load}}$ analysis (GEHLA):
  Here, for every set the transmission amplitude at the maximum load, close to 6000 N, was taken. At the maximum fatigue load the crack size is expected to be at its maximum and therefore also the decrease in transmission. The threshold value was defined as 95% of its initial value, in accordance with the previous method (i.e. GEIRA). It has an identical vulnerability to environmental changes as the previous method (i.e. GEIRA).

- Correlation between LF loading and HF probe wave analysis (CA):
  In this algorithm, the transmission amplitude and the corresponding applied load were used. For every set the correlation coefficient was calculated. From experimental observations the correlation is expected to be positive for an intact sample. The correlation of a damaged sample is expected to be negative, because higher load results in a larger crack and thus in less transmission. The correlation between both was calculated and compared to a fixed threshold. This threshold was set to -0.2, in order to assure significant negative correlation. This algorithm is quite robust for environmental changes since the actual values of the transmission amplitudes do not affect the correlation. However, strong negative correlation arising from non-defect-related modulation, would make this technique unusable. Environmental changes affecting the sensing system are the most likely cause of non-defect-related modulation in this method.

- Correlation of data below a cut-off load analysis (CBCOA):
  In this approach the correlation between the transmission amplitude and the corresponding applied load was calculated for a reduced data set. Only data measured below a certain cut-off load was used. It was experimentally observed that only the transmission amplitudes measured below this cut-off load vary linear with the applied load, hence the correlation is expected to be larger than when calculated using all data. The same threshold value as in the previous algorithm (CA) was used and the same general conclusions on the algorithm and the threshold value apply.

- Modulation coefficient of data below a cut-off load analysis (MCBCOA):
  Also here, the transmission amplitude and the corresponding applied load were used. The transmission amplitude was normalised, to lie in the interval [0 1], and thereby very robust to environmental changes. For every set the modulation coefficient, i.e. the linear fit of the transmission amplitude as a function of the applied load, was calculated. For the aforementioned reasons, only data measured at loads below the cut-off load was used. The modulation coefficient is expected to transition from a fixed value to a negative value, when damage is present. A fixed threshold was used to differentiate between healthy and damaged. This threshold had to be defined in calibration measurements since a theoretical prediction of the values is not possible. Hence, this method is not reference-free and is very susceptive to errors on measured load values.

- Modulation depth analysis (MDA):
  It was also tried to only use the transmission amplitude. Every set was normalised by dividing the data by the average transmission amplitude. This presumes that the modulation depth scales linear with the transmission amplitude. The modulation depth was calculated by taking the standard deviation of every set. In an intact sample, only limited modulation by the sensing system is presumed. The initiation and propagation of cracks increases the modulation. The threshold value was the average modulation depth of the intact component (or sample) increased with three times the standard deviation on the modulation depth in the initial stage. Due to the sharp increase in modulation for a growing crack, environmental changes altering the modulation depth in an intact sample could be compensated by increasing the threshold value.

- High-transmission load analysis (HTLA):
  Here, the load and the transmission amplitude were used. The average load corresponding to the (five) highest transmission amplitudes was calculated. When a crack is present transmission is significantly higher at low loads. Without a crack, the relation between load and transmission is observed to be sample dependent. In general, it can be expected that the average high transmission load is higher than the lowest loads. Accurate probing of the loads or a load indicating parameter is essential. Twice the lowest load is taken as threshold value. Environmental changes in transmission amplitude and small (systematic) errors on the load measurements are not expected to influence this method.

- Median transmission analysis (MTA):
  It is also possible to only use the transmission amplitude, obtained with symmetrically distributed sampling over the load (cf. section 5.6.3). Every set is normalised, to lie in the interval [0 1], making the data very robust to environmental changes. Next, the median was calculated. The median in an intact sample is expected to be close to 0.5 when the modulation of the sensing system is absent or linear. When a defect is present, and the applied loads are sufficiently high to reach the cutoff load, the distribution of the transmission amplitudes becomes asymmetric and the median becomes smaller than 0.5. As reference value, twice the local standard deviation of the high frequency part of median was chosen. If the condition of symmetric sampling over the load is not filled calibration measurements are nec-

essary. However, this method is very robust if the load is higher higher than the cut-off load.

Automated evaluations of the sample health by the different approaches discussed above, were performed for two 1 mm aluminium plates and for three 6 mm samples. The results are shown in Figure 5.35. Figures of the detection parameter and the threshold value throughout the experiment, for every sample and every technique are attached in appendix B. These tests were performed in the laboratory, where the excitation and detection efficiency of the transducers and the not-defect-related wave propagation properties of the samples can be considered constant. Hence, the steady state amplitude analysing detection techniques can be considered very stable and thus used as reference measurements.

In all tests, the sensitivity of the linear high-load method (GEHLA) is much better than the classic at-rest method (GEIRA). Due to the very high threshold value, the high-load method is often the best performing diagnostic algorithm.

The correlation-, modulation coefficient-, and median-based diagnostic algorithms (CA, CBCOA, MCBCOA, MTA) are most sensitive to nonlinear modulation of the sensing system. Consequently these algorithms perform badly on the aluminium plates, where the sensing system was strongly modulated by the fatigue loading.

The general evolution of the high-load transmission-, correlation-, modulation coefficient-, and high-transmission load based methods (GEHLA, CA, CBCOA, MCBCOA, HTLA) all require measurements of the load. In the methods where only data measured under the cut-off load were used, detection is not possible when the measurements on the load have systematical errors, as with 6 mm-sample 2.

In all proposed nonlinear detection algorithms, strategies to diminish the effects of environmental changes on the propagation properties of the components and on the transmission amplitude measured by the sensing system were incorporated. The most robust solutions, with respect to this issue, are the correlation- and high-transmission load-based algorithms (CA, CBCOA, HTLA) since they only depend weakly on the transmission. The algorithms (MCBCOA, MTA) in which the transmission amplitude is normalised by expression 5.6, can also be considered very robust. The general evolution analysing methods (GEIRA, GEHLA) are not suitable when transmission efficiency or propagation properties are expected to change.

Correlation analysis (CA, CBCOA) has the strong advantage that the used

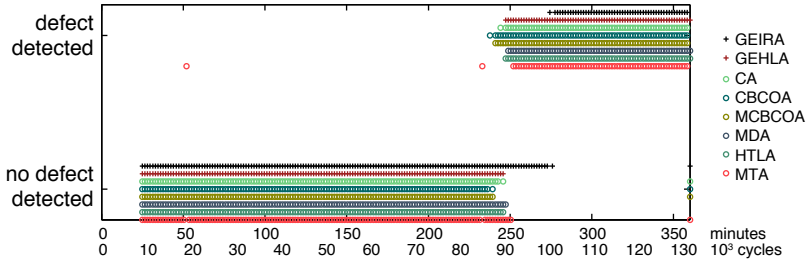

(a) 6 mm aluminium bar with a 1 mm thick crack susceptible region type sample, used as reference sample in section 5.6.

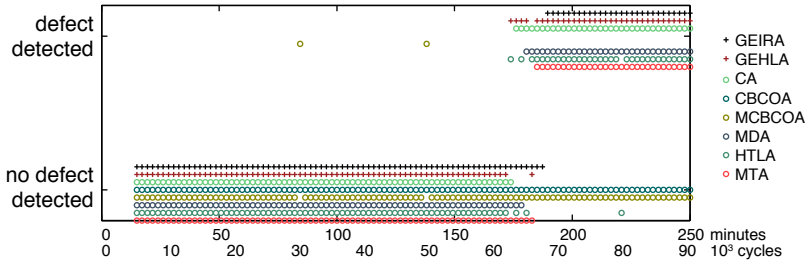

(b) 6 mm aluminium bar with a 1 mm thick crack susceptible region type sample, as described in section 5.6. Measurements were stopped before the sample failed.

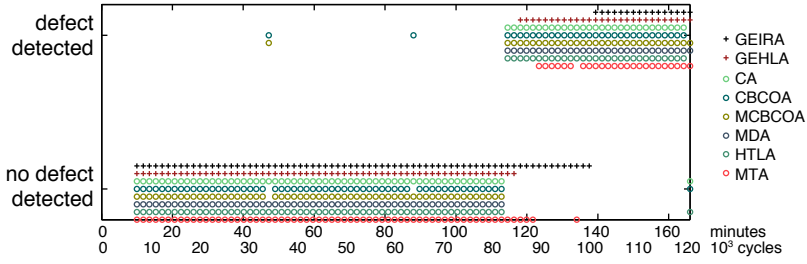

(c) 6 mm aluminium bar with a 1 mm thick crack susceptible region type sample, as described in section 5.6. Fatigue loading was performed at 12 Hz and due to a problem in the triggering mechanism, the data was not sampled with a normal distribution of the fatigue cycle.

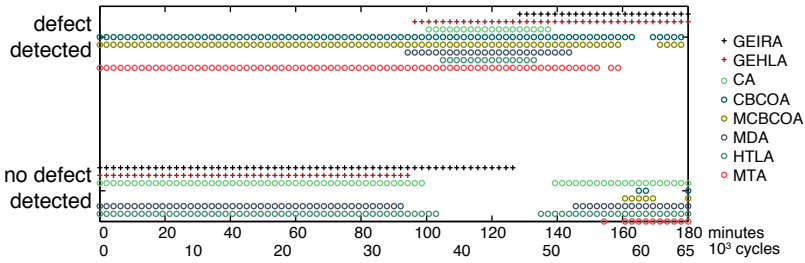

(d) 1 mm aluminium plate type sample, the reference sample in section 5.5.

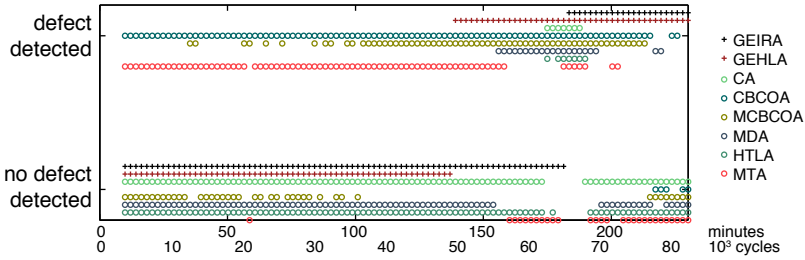

(e) 1 mm aluminium plate type sample, as described in section 5.5. Adequate measuring of the applied load was not available during this experiment.

Figure 5.35 The outcome of the different diagnostic algorithms for five different samples. To evaluate the state of the sample, the different defect development quantifiers were compared the corresponding threshold values, plots thereof are presented in appendix B. In the experiments with the 1 mm aluminium plate type samples the sensing system was affected by strong nonlinear modulation caused by fatigue loading.

quantity does not dependent on the actual transmission amplitudes. But it has the major drawback that it cannot be used if the initial modulation of the sensing system is (strongly) negative, since a negative correlation is associated with a defect. Modulation coefficient based algorithms (MCB-COA) offer an outcome to this problem, but these need detailed reference values on the expected initial modulation coefficient and the order of the modulation coefficient in a damaged sample. Without this information, it is not possible to choose a good threshold value.

Evaluation of the modulation depth (MDA) reveals the start of a crack formation in every sample, but it is not unambiguous at large cracks in the aluminium plate. In general, modulation depth analysis (MDA) is highly effective in detecting cracks and has a high contrast due to the significant increase of the modulation depth at the beginning of a crack formation.

Analysis of the high-transmission loads (HTLA) proved similar performances as the evaluation of the modulation depth (MDA). In the 1 mm samples large nonlinear modulation of the PZT transducers in the sensing system, induced by fatigue loading, makes this method unsuitable as a general method for crack detection, as can be concluded from Figure 5.21. Nevertheless, in the specific case of these two 1 mm thick samples, the nonlinear PZT-modulation was in such a way, that for an intact sample high transmission took place at high loads. In this, very specific, case the transition from intact to damaged was very dramatic. For the 6 mm samples, were the sensing system was not strained, this method is very successful, if adequate load measuring is provided. At the time when 6 mm sample 2 was measured, this load measuring was not yet optimised, and therefore the threshold value had to be doubled in order to detect the defect.

Median transmission analysis (MTA) cannot be applied in cases of unpredictable modulation of the transmitter-receiver system, as with the 1 mm samples. For the three other samples it offers adequate sensitivity, which can be enhanced by increasing the number of samples during one set, improving the error on the median.

A summeriest overview of the most important features related to the tested diagnostic algorithms is presented in Table 5.3. The crosses indicate how strong the performance of a method is affected by the corresponding feature.

All together, at first sight general evolution based detection using measurements at high loads (GEHLA) seems to be the best choice, due to its simplicity and high sensitivity. As stressed earlier, environmental variations in the component make this method of defect detection inapplicable. The

nonlinear techniques all have their specific pros and cons but were designed to withstand these harsh conditions. The technical possibilities and the specific component determines which approach is best suited.

A schematic overview of the performance and the features influencing the performance of the diagnostic algorithms is presented in Table 5.3.

	GEIRA	GEHLA	CA	MCA	MDA	HTLA	MTA
Closed defect detection	- - -	-	+++	+++	+++	+++	+++
Load measurement			xxx	xx		x	
Calibration	xxx	xxx		xx	x		
Robustness to sensing system modulation							
long timescale	- - -	- - -	+++	+++	+	+++	+++
short timescale	++	+++	- - -	- - -	-	- -	- - -
Contrast between damaged and undamaged	- - -	- -	+++	+++	++	+++	++
Normalisation				xx	xx		xx

Table 5.3 Overview of the features of the different diagnostic algorithms.
GEIRA: General evolution of $A^j_{\text{in-rest load}}$ analysis,
GEHLA: General evolution of $A^j_{\text{high load}}$ analysis,
CA: Correlation between LF loading and HF probe wave analysis,
MCA: Modulation coefficient analysis,
MDA: Modulation depth analysis,
HTLA: High-transmission load analysis,
MTA: Median transmission analysis.
x: The amount of x's indicates the sensitivity to small errors on the quantity or in the process.
+ and - : Go from very good to very bad.

Chapter 6

Conclusions

In this thesis, a non-destructive testing method using nonlinear ultrasonics was studied, with the aim to detect early stage fatigue damage in vibrating components. Although a large variety of NDT techniques are commercially available, only a limited amount thereof can be implemented to perform structural health monitoring in operational conditions. A nonlinear ultrasonic NDT technique to detect damage in such harsh environments needs to differentiate between nonlinear features related to a defect, and other nonlinearity features, e.g. resulting from vibrating mechanical contacts. Besides this, it must be resistant to environmental changes, such as temperature differences or dirt built-up, which, in most ultrasonic techniques, have a severe influence on the sensing system. In order to get deeper insight in the mechanisms of nonlinear modulation of a gap between the two surfaces of a delamination (or by extension, a crack), and specifically of the role of the presence of air in the gap, nonlinear effects in an absorptive bilayer were simulated and analysed, Lamb mode selection using different sensing systems was tested, a feasibility study of the proposed detection scheme was performed, a laboratory test environment to acquire experimental data was developed, different diagnostic algorithms were defined, and their performance was compared using experimental data.

In the proposed NDT technique, the targeted defect susceptible area is probed by ultrasonic waves. In the presence of a vibrating defect, the probe waves undergo nonlinear modulation when propagating through the defect. The developed diagnostic algorithms relate this modulation to the vibration of the component in order to evaluate its state.

Air filled delaminations in an absorptive bilayer

A theoretical study of the nonlinear interaction of probing Lamb waves with a vibrating air filled delamination in a steel/rubber bilayer was performed. In this model, the physical properties of the air layer in the delamination are periodically changing, thereby inducing modulation of the probe waves. The dispersion characteristics of the Lamb modes in the delaminated region were calculated and analysed for a wide compression range. The LM_S mode, which roughly follows the S_0 mode of steel, was found to be the most suitable probe mode for detection in real life applications. Strong coupling between rubber and steel was observed near the cut-off frequencies for longitudinal waves in the delamination. In order to predict this coupling, an analytical matching condition was derived. For a given frequency, the compression at which the coupling is maximum, and consequently maximum attenuation is reached, depends on the thermodynamical conditions of the air layer. By examining the normal displacement on the surfaces of the structure, it was illustrated that cross-modulation between the probe wave amplitudes and the cyclic vibration of the delamination is largest when the compression is in the vicinity of the coupling-compression.

Lamb mode selection

When working with plate-like samples or components, the advantages of Lamb mode selection are significant. Filtering out unwanted modes reduces complicated interference, which arises when multiple Lamb modes and their reflections of a single frequency coincide at the sensor. In this work, three different approaches for Lamb mode selection were validated.

Using wavelength selection, the A_0 Lamb mode of interest, of which the wavelength matched the array-spacing, was significantly amplified. The specific combination of the array elements had a strong influence on suppression of the S_0 mode, which was the unwanted mode, and consequently on the increase in the ratio between the preferred and the not-preferred mode. Wave scattering due to reflections and mode conversion at the individual elements of the sensor array reduced the array's performance, and hence limited its number of useful elements. In excitation-mode, increasing the number of elements in the transducer array resulted in higher amplification and contrast increase than in the detection configuration. Nevertheless, the maximum ratio between the preferred A_0 and not-preferred S_0, for the actuator and sensing array, were comparable. Combining a selective actuator and sensor was not attempted, although the obtained results indicate

that this would provide a promising sensing system. Wavelength selection provides a simple tool, i.e. only analog hardware is necessary, to select Lamb modes with a wavelength matching the array spacing.

An electronic control system to actuate a mode selective transmission array, which could excite up to 24 elements individually, was designed and partially tested. Nevertheless, further development of this multiplexed actuator array was put on hold. The complexity and corresponding cost of the development of a 24 channel amplifier was not justifiable in the scope of this project. Consequently, only the implementation of velocity selective detection of Lamb modes was achieved. The individually measured transducer responses were delayed off-line. The results were comparable for selection of both modes (S_0, A_0) and in accordance with the results obtained by wavelength selection. Velocity selection is a very versatile tool capable of selecting multiple modes. However, it requests dedicated hardware and is therefore less cheap and easy to implement.

In a third approach, it was attempted to exploit the difference in the symmetry of the displacement pattern of symmetric and asymmetric Lamb waves, to select a preferred symmetry. In principle, this procedure is very straightforward and simple to implement. A symmetric mode is selected by adding the out of plane displacement, while to select an asymmetric mode the out off plane displacement has to be subtracted. In practice Lamb mode selection by this method was unsuccessful. Due to the complexity of the stress distributions, and resulting piezoelectric signal generation in the PZT transducers glued to the sample, the output of the transducers is not linearly related to a single stress or displacement of the probe waves. Therefore mode selection, based on the (a)symmetry of Lamb wave displacement, could not be performed. As was illustrated by other research groups, a dedicated choice of transducers could resolve this problem and provide a cheap and easy tool for high contrast mode selection.

Detection of vibrating cracks

The emphasis of this work was on the development and validation of diagnostic algorithms to detect crack defects in a vibrating environment. As explained while describing the methodology in Chapter 5, ultrasonic probe waves undergo mode conversion and are reflected when interacting with a defect. The transmitted amplitude of the probe waves decreases when the crack, and hence the impedance mismatch in the medium, increases. On the other hand, when a crack closes, e.g. due to compression, the acous-

tic mismatch disappears and the probe waves become insensitive to the (closed) defect. In a vibrating component, the state of the crack dynamically changes, consequently the amplitude of the transmitted probe waves undergoes nonlinear modulation. In this PhD thesis, diagnostic algorithms were developed and validated. These algorithms were based on the nonlinear modulation of the probe waves by the vibrating crack.

In order to quantify the defect-related modulation of the transmitted probe waves, a dedicated sensing system was developed. By combining short burst probe waves and time gating, the detected wave packets were separated from reflections originating from boundaries or mechanical contacts. This assured that the detected probe waves were only modulated by the interaction with the defect and not by e.g. vibrating mechanical contacts.

During fatigue loading of 1 mm aluminium plates, large nonlinear modulation of the sensing system took place. This modulation predominantly resulted from nonlinear piezoelectric behaviour in the PZT transducers. The strain induced nonlinear sensing system modulation hindered the development of the proposed diagnostic algorithms. These algorithms were based on the nonlinear effects of the plate modulation on the probe wave transmission through the damaged region and high base-line modulation made them unsuitable. Therefore, an adapted sample was introduced, in which the transducers were placed in a low stress area in order to prevent sensing system nonlinearity.

Two classic US-NDT schemes, evaluating quasi-steady signal amplitude features, were compared with five new algorithms developed during this work. In the classic scheme, the decrease in transmission amplitude, caused by the developing crack, is monitored. In order to allow unambiguous linear US-NDT, calibration measurements and a transmission setup with unaltered wave propagation properties over the entire component-life are necessary. The five new nonlinear US-NDT algorithms were developed to address these unpractical requirements.

A first algorithm exploits the negative correlation between transmission amplitude and crack size. This algorithm requires that no significant negative correlation, e.g. induced by the sensing system, is present. If this requirement is met, it provides good sensitivity and contrast.

A similar approach is based on a modulation coefficient, which was expressing the sensitivity of the transmission amplitude on the applied load. In this approach the state of the sample is related to the magnitude of the modulation coefficient and a sudden change thereof is attributed to damage. In

order to set a threshold, prior knowledge of the modulation coefficient in an intact and in a damaged component is required.

A third algorithm monitors the amplitude of the nonlinear modulation of the normalised transmitted amplitude. This modulation depth was shown to drastically increase for an emerging defect. Again, calibration measurements are necessary to define a threshold value. However, due to the strong increase in modulation depth in an early stage of the crack, moderate changes of the baseline/reference value of the modulation depth can be absorbed by choosing a rather high threshold value, with respect to the expected baseline variation, which only has a small influence on the sensitivity. This algorithm is less sensitive to systematic changes of the structure, of the probe emission amplitude, and of the transmitted wave detection efficiency than the aforementioned algorithms and linear US-NDT.

It is also possible to study the load at which a maximum in transmission is measured. A convergence from a regime in which high loads resulted in high transmission amplitudes to a regime of high transmission at low loads, as expected for the case of a crack, was observed. This type of detection is very robust to changes in the sensing system.

In a final approach, statistical features of the transmission amplitude, rescaled to the interval [0 1], were used. The median of the normalised transmission amplitudes was compared with its expected value of 0.5. This quantifier proved to be a robust defect dependent parameter. The threshold value was defined as the local standard deviation of the median, which makes this technique reference-free.

These five modulation based methods were shown to provide robust, based on a cheap sensing system, and sensitive nonlinear ultrasonic defect detection. The different diagnostic algorithms were developed accordingly to different situations with regard to the sensing system, availability of reference measurements, expected influence of environmental changes, etc. With the presented concept, cracks in inaccessible, high risk zones of components in vibrating structures, such as airplane wings or wind turbines, for different conditions and components can be detected.

Outlook

When performing crack detection in plates, the option to discriminate between different modes allows for the development of smarter detection algorithms and self-calibrating sensing systems. Symmetry-based mode selec-

tion is particularly interesting, due to its simplicity in implementation and high contrast between symmetrical and asymmetrical modes.

A detailed study of the stress inside the PZT transducers, e.g. using a finite element model of the plate with the transducers, could provide better insight on the generation of Lamb wave induced piezoelectric signals, and modulation of those signals due to nonlinear effects. Alternatively, a different type of transducers could be used, e.g. other PZT-types or geometries of piezoelectric transducers or accelerometers.

The nonlinear modulation of the PZT transducers in the sensing system should be investigated further and resolved in order to detect defects in plates. Again, the use of a different type of piezoelectric transducers could offer a solution. Especially, the use of hard PZT transducers as actuators, which are able to transmit more power than the currently used soft Pz27 type of PZT transducers, would be preferable.

The experimental data, with which the five nonlinear modulation based diagnostic algorithms were validated, were acquired with an identical probe wave packet, i.e. a 600 kHz burst of less than 8 periods. A study on the influence of the probe wave frequency and the number of periods in one probe wave packet on the sensitivity to defects of the developed algorithms, should be performed.

In order to validate the proposed diagnostic algorithms for crack detection of solid objects, experiments with Rayleigh waves probing, e.g. a rod, are suggested. The use of Rayleigh waves instead of Lamb waves is expected to simplify matters. Since only one Rayleigh mode exists, the length of the probe wave packet is determined by the first reflections and can therefore be longer, especially when the transducers are placed closer around the location where the crack is expected.

Appendix A

Displacement and stress inside a plate

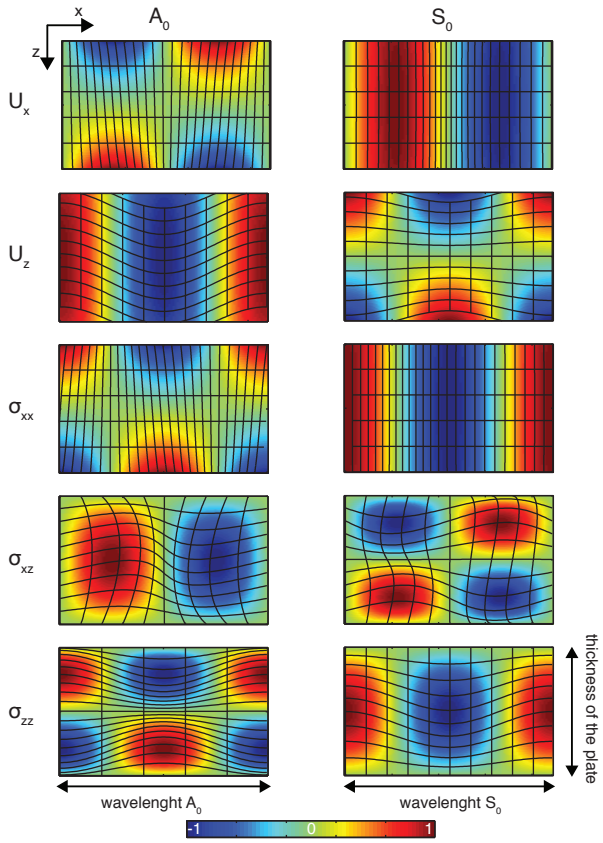

Figure A.1 Displacement and stress of the A_0 and the S_0 Lamb mode inside an solid plate. The length of the x-axis is equal to one wavelength and the length of the z-axis is equal to the plate thickness. The displacement and stress are normalised. The overlaying grid plots are an indicator of the direction and the amplitude is arbitrary.

Appendix B

Diagnostic algorithms applied on five samples

The diagnostic algorithms presented in Chapter 5 consist of a defect development quantifier and a corresponding threshold value. Both elements were designed to provide unambiguous defect detection. In the following figures both are plotted for experiments on five different samples. These figures correspond to Figure 5.35.

The experiments were all performed as described in Chapter 5, with two exceptions. In one experiment on a 6 mm aluminium bar with a 1 mm thick crack susceptible region type sample, the fatigue loading frequency was increased to 12 Hz, which resulted in a problem in the triggering and consequently a non-uniform sampling of the fatigue cycle. In one experiment on a 1 mm aluminium plate type sample, the loading force was not measured adequately. Both exceptions are stated in the caption of the corresponding figures.

During the experiments with the 1 mm aluminium plate type samples, the stress across the sample caused strong nonlinear modulation of the sensing system. This problem was resolved in the 1 mm aluminium plate type samples by placing the sensor system in a low stress region.

In the figures, a short description of how the defect development quantifier and a corresponding threshold value were defined is given, for the a detailed discussion refer to section 5.7.

General evolution of $A^j_{\text{in-rest load}}$ analysis (GEIRA):

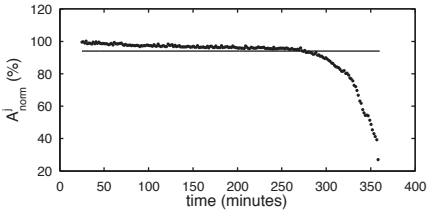

(a) 6 mm aluminium bar with a 1 mm thick crack susceptible region type sample, the reference sample in section 5.6

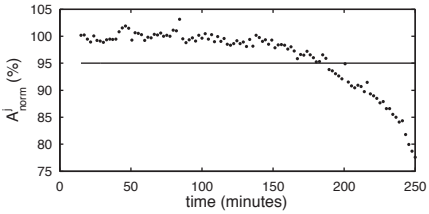

(b) 6 mm aluminium bar with a 1 mm thick crack susceptible region type sample, as described in section 5.6. Measurements were stopped before the sample failed.

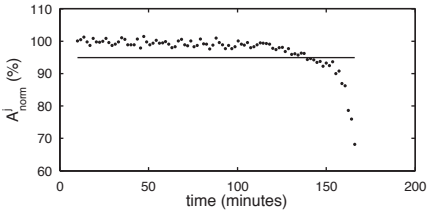

(c) 6 mm aluminium bar with a 1 mm thick crack susceptible region type sample, as described in section 5.6. Fatigue loading was performed at 12 Hz and due to a problem in the triggering mechanism, the data was not sampled with a normal distribution of the fatigue cycle.

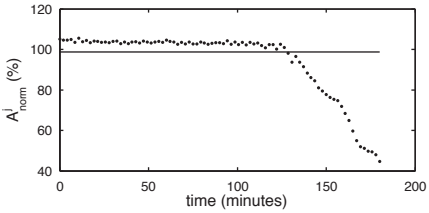

(d) 1 mm aluminium plate type sample, the reference sample in section 5.5.

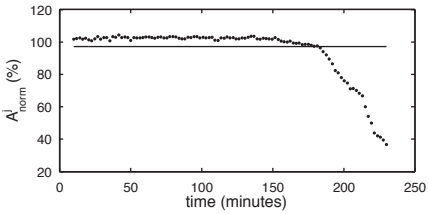

(e) 1 mm aluminium plate type sample, as described in section 5.5. Adequate measuring of the applied load was not available during this experiment.

Figure B.1 $A^j_{600\text{N}}$ is the transmission amplitude at the minimum load in a fatigue cycle. The threshold value is 95% of the initial transmission amplitude at minimum load. amplitude.

General evolution of $A^j_{\text{high load}}$ analysis (GEHLA):

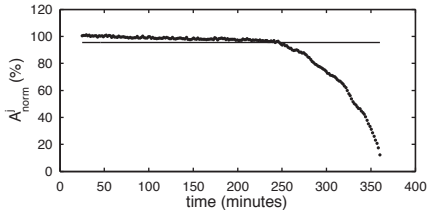

(a) 6 mm aluminium bar with a 1 mm thick crack susceptible region type sample, the reference sample in section 5.6.

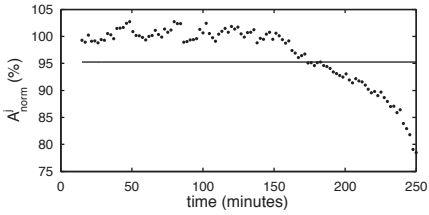

(b) 6 mm aluminium bar with a 1 mm thick crack susceptible region type sample, as described in section 5.6. Measurements were stopped before the sample failed.

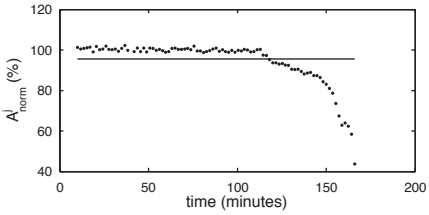

(c) 6 mm aluminium bar with a 1 mm thick crack susceptible region type sample, as described in section 5.6. Fatigue loading was performed at 12 Hz and due to a problem in the triggering mechanism, the data was not sampled with a normal distribution of the fatigue cycle.

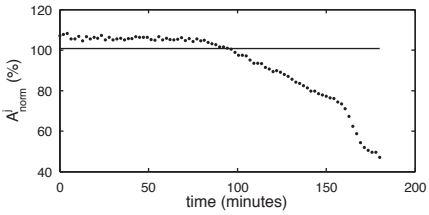

(d) 1 mm aluminium plate type sample, the reference sample in section 5.5.

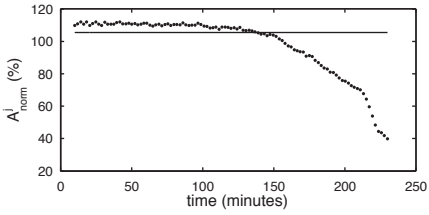

(e) 1 mm aluminium plate type sample, as described in section 5.5. Adequate measuring of the applied load was not available during this experiment.

Figure B.2 $A^j_{6000\text{N}}$ is the transmission amplitude at the maximum load in a fatigue cycle. The threshold value is 95% of the initial transmission amplitude at maximum load.

Correlation between LF loading and HF probe wave analysis (CA):

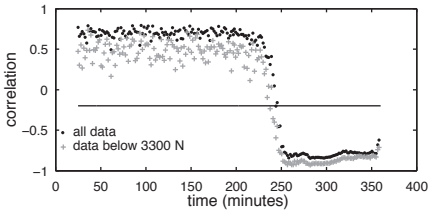

(a) 6 mm aluminium bar with a 1 mm thick crack susceptible region type sample, the reference sample in section 5.6.

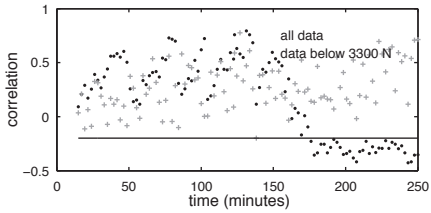

(b) 6 mm aluminium bar with a 1 mm thick crack susceptible region type sample, as described in section 5.6. Measurements were stopped before the sample failed.

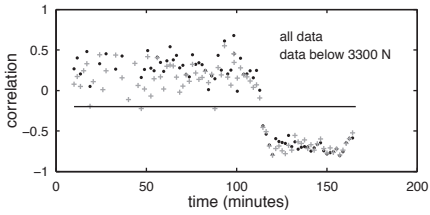

(c) 6 mm aluminium bar with a 1 mm thick crack susceptible region type sample, as described in section 5.6. Fatigue loading was performed at 12 Hz and due to a problem in the triggering mechanism, the data was not sampled with a normal distribution of the fatigue cycle.

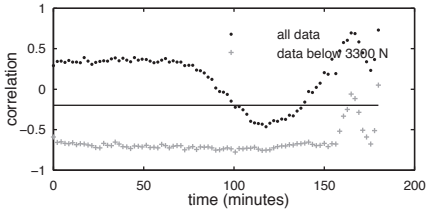

(d) 1 mm aluminium plate type sample, the reference sample in section 5.5.

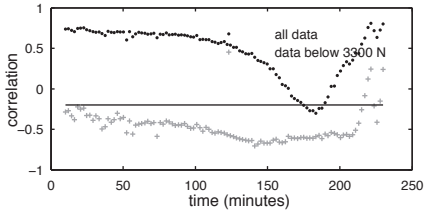

(e) 1 mm aluminium plate type sample, as described in section 5.5. Adequate measuring of the applied load was not available during this experiment.

Figure B.3 For every set the Pearson correlation between the transmission amplitude and the corresponding applied load was calculated. In order to increase sensitivity, a second data set was constructed in which only data measured below loads of 3300 N were considered (CBCOA). The threshold was set to -0.2, in order to assure significant negative correlation.

Modulation coefficient of data below a cut-off load analysis (MCBCOA):

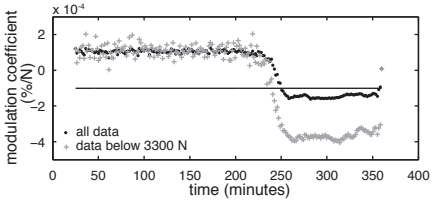

(a) 6 mm aluminium bar with a 1 mm thick crack susceptible region type sample, the reference sample in section 5.6.

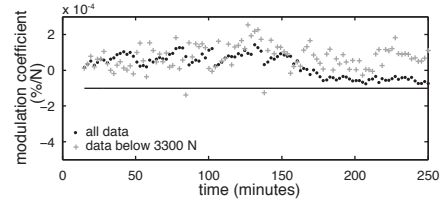

(b) 6 mm aluminium bar with a 1 mm thick crack susceptible region type sample, as described in section 5.6. Measurements were stopped before the sample failed.

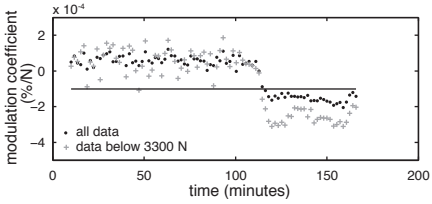

(c) 6 mm aluminium bar with a 1 mm thick crack susceptible region type sample, as described in section 5.6. Fatigue loading was performed at 12 Hz and due to a problem in the triggering mechanism, the data was not sampled with a normal distribution of the fatigue cycle.

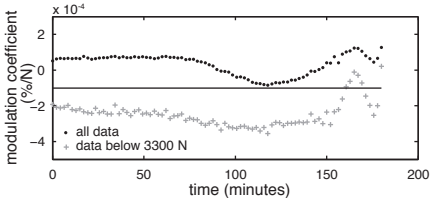

(d) 1 mm aluminium plate type sample, the reference sample in section 5.5.

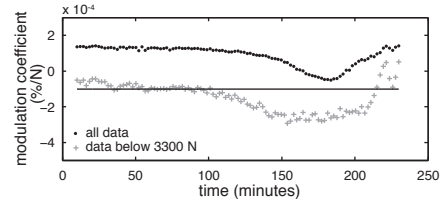

(e) 1 mm aluminium plate type sample, as described in section 5.5. Adequate measuring of the applied load was not available during this experiment.

Figure B.4 The transmission amplitude was normalised, to lie in the interval [0 1]. For every set the modulation coefficient, i.e. the linear fit of the transmission amplitude as a function of the applied load, was calculated. Thereby using only data measured under at loads below the cut-off load. Here the results obtained with a dataset including all data are presented as well. The threshold value was -10^{-4}.

Modulation depth analysis (MDA):

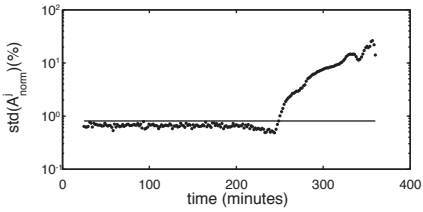

(a) 6 mm aluminium bar with a 1 mm thick crack susceptible region type sample, the reference sample in section 5.6.

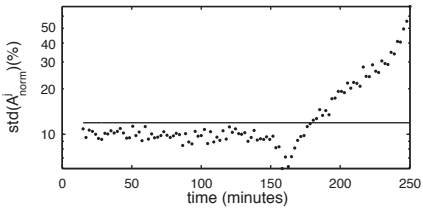

(b) 6 mm aluminium bar with a 1 mm thick crack susceptible region type sample, as described in section 5.6. Measurements were stopped before the sample failed.

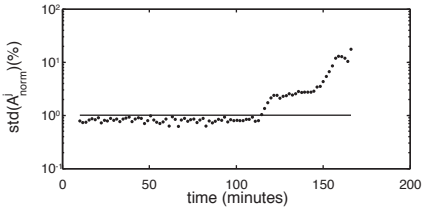

(c) 6 mm aluminium bar with a 1 mm thick crack susceptible region type sample, as described in section 5.6. Fatigue loading was performed at 12 Hz and due to a problem in the triggering mechanism, the data was not sampled with a normal distribution of the fatigue cycle.

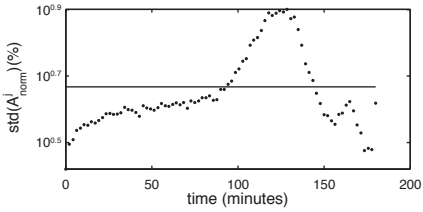

(d) 1 mm aluminium plate type sample, the reference sample in section 5.5.

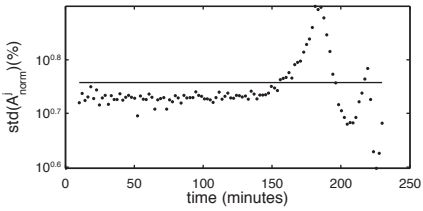

(e) 1 mm aluminium plate type sample, as described in section 5.5. Adequate measuring of the applied load was not available during this experiment.

Figure B.5 Every set was normalised by dividing the data by the average transmission amplitude. The modulation depth was calculated by taking the standard deviation of every set.The threshold value was the average modulation depth of the intact component (or sample) increased with three times the standard deviation on the modulation depth in the initial stage.

High-transmission load analysis (HTLA):

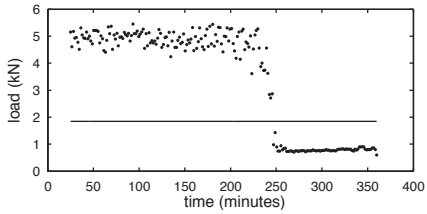

(a) 6 mm aluminium bar with a 1 mm thick crack susceptible region type sample, the reference sample in section 5.6.

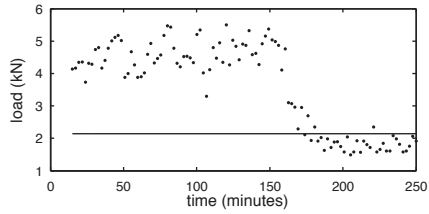

(b) 6 mm aluminium bar with a 1 mm thick crack susceptible region type sample, as described in section 5.6. Measurements were stopped before the sample failed.

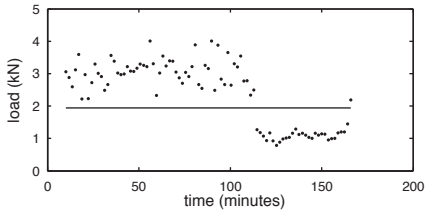

(c) 6 mm aluminium bar with a 1 mm thick crack susceptible region type sample, as described in section 5.6. Fatigue loading was performed at 12 Hz and due to a problem in the triggering mechanism, the data was not sampled with a normal distribution of the fatigue cycle.

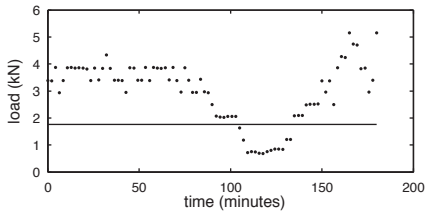

(d) 1 mm aluminium plate type sample, the reference sample in section 5.5.

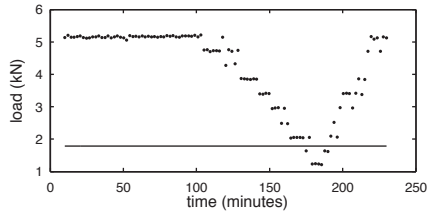

(e) 1 mm aluminium plate type sample, as described in section 5.5. Adequate measuring of the applied load was not available during this experiment.

Figure B.6 The average load corresponding to the five highest transmission amplitudes was calculated. Twice the lowest load is taken as threshold value.

Median transmission analysis (MTA):

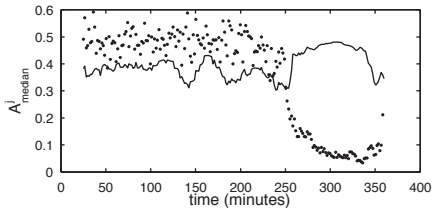

(a) 6 mm aluminium bar with a 1 mm thick crack susceptible region type sample, the reference sample in section 5.6.

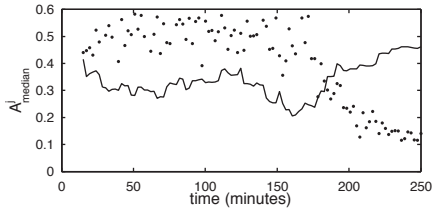

(b) 6 mm aluminium bar with a 1 mm thick crack susceptible region type sample, as described in section 5.6. Measurements were stopped before the sample failed.

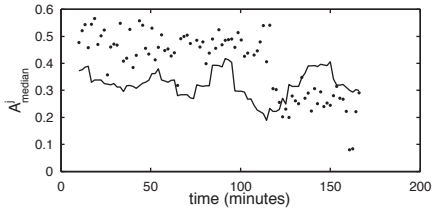

(c) 6 mm aluminium bar with a 1 mm thick crack susceptible region type sample, as described in section 5.6. Fatigue loading was performed at 12 Hz and due to a problem in the triggering mechanism, the data was not sampled with a normal distribution of the fatigue cycle.

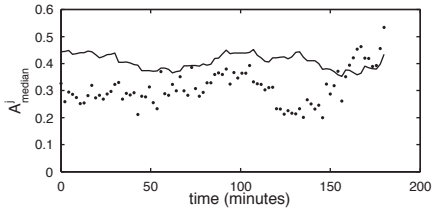

(d) 1 mm aluminium plate type sample, the reference sample in section 5.5.

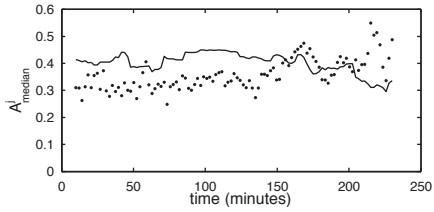

(e) 1 mm aluminium plate type sample, as described in section 5.5. Adequate measuring of the applied load was not available during this experiment.

Figure B.7 Every set of measurement data is normalised, to lie in the interval [0 1], then the corresponding the median was calculated (A^j_{median}). The threshold value is twice the local standard deviation of the high frequency part of median.

Appendix C

Lamb modes in triple layers

In this appendix is described how the displacement and stress fields for Lamb waves in a triple layer structure, with a shear-free middle layer, can be calculated. This procedure was used when simulating the results presented in section 3.4.

The displacement fields for the forward propagating Lamb mode in the first ($0 \leq z \leq d_1$), the second ($d_1 \leq z \leq d_2$) and the third ($d_2 \leq z \leq d_3$) layer of the composite plate can be written as follows (with $d_1 = d_{l1}$, $d_2 = d_{l1} + d_{l2}$, $d_3 = d_{l1} + d_{l2} + d_{l3}$, and d_{ln} the thickness of layer n):

$$\begin{aligned}
u_{z,1} =& (-A^+_{1T} k e^{ik_{Tz,1}z} - A^-_{1T} k e^{-ik_{Lz,1}z} + A^+_{1L} k_{Lz,1} e^{ik_{Lz,1}z} - A^-_{1L} k_{Lz,1} e^{-ik_{Lz,1}z}) \\
& e^{i(ky-\omega t)} \\
u_{z,1} =& (A^+_{1T} k_{Tz,1} e^{ik_{Tz,1}z} - A^-_{1T} k_{Tz,1} e^{-ik_{Tz,1}z} + A^+_{1,L} k e^{ik_{Lz,1}z} + A^-_{1L} k e^{-ik_{Lz,1}z}) \\
& e^{i(ky-\omega t)} \\
u_{z,2} =& (A^+_{2L} k_{Lz,2} e^{ik_{Lz,2}z} - A^-_{2L} k_{Lz,2} e^{-ik_{Lz,2}z}) \\
& e^{i(ky-\omega t)} \\
u_{z,2} =& (A^+_{2L} k e^{ik_{Lz,2}z} + A^-_{2L} k e^{-ik_{Lz,2}z}) \\
& e^{i(ky-\omega t)} \\
u_{z,3} =& (-A^+_{3T} k e^{ik_{Tz,3}z} - A^-_{3T} k e^{-ik_{Lz,3}z} + A^+_{3L} k_{Lz,3} e^{ik_{Lz,3}z} - A^-_{3L} k_{Lz,3} e^{-ik_{Lz,3}z}) \\
& e^{i(ky-\omega t)} \\
u_{z,3} =& (A^+_{3T} k_{Tz,3} e^{ik_{Tz,3}z} - A^-_{3T} k_{Tz,3} e^{-ik_{Tz,3}z} + A^+_{3,L} k e^{ik_{Lz,3}z} + A^-_{3L} k e^{-ik_{Lz,3}z}) \\
& e^{i(ky-\omega t)}
\end{aligned}$$

where

$$\begin{aligned}
k^2_{Lz,n} &= k^2_{L,n} - k^2 \quad \text{with} \quad n = 1, 2, 3 \\
k^2_{Tz,n} &= k^2_{T,n} - k^2 \quad \text{with} \quad n = 1, 3
\end{aligned}$$

in which $k_{L,n}$ is longitudinal waves wavenumber in layer n (for $n = 1, 2, 3$), $k_{T,n}$ is the wavenumber of shear waves in the layer n (for $n = 1, 3$) (in the second layer viscosity is neglected), k is the wavenumber of Lamb mode, $A^{\pm}_{1T,1L}$, $A^{\pm}_{3T,3L}$ are the unknown coefficients to be found. Expressions for stress tensor components can be easily written down taking into account standard stress-strain relations.

Taking into account free boundary conditions at $z = 0, d_3$ and boundary conditions at $z = d_{1,2}$ (continuity of mechanical displacement vector component u_z, stress tensor component σ_{zz} and the boundary conditions $\sigma_{yz} = 0$), a system of 10 linear equations for 10 unknown coefficients can be written down. The determinant of the system has to be equal to zero. This condition leads to the following dispersion equation for Lamb modes wavenumbers:

$$\frac{\alpha_1(m_2^+ - m_3^+ m_2^-/m_3^-) + k_{Lz,2}(m_4^+ + m_3^+ m_4^-/m_3^-)}{\alpha_1(m_2^+ - m_3^+ m_2^-/m_3^-) - k_{Lz,2}(m_4^+ + m_3^+ m_4^-/m_3^-)} e^{(2ik_{Lz,2}d_{l2})} - \frac{\alpha_2(n_2^+ - n_3^+ n_2^-/n_3^-) + k_{Lz,2}(n_4^+ + n_3^+ n_4^-/n_3^-)}{\alpha_2(n_2^+ - n_3^+ n_2^-/n_3^-) - k_{Lz,2}(n_4^+ + n_3^+ n_4^-/n_3^-)} = 0$$

where

$m_1^+ = kb_1 \exp(ik_{Lz,1}d_1) + kc_1 \exp(-ik_{Lz,1}d_1) + k_{Tz,1} \exp(ik_{Tz,1}d_1)$,
$m_1^- = kc_1 \exp(ik_{Lz,1}d_1) + kb_1 \exp(-ik_{Lz,1}d_1) + k_{Tz,1} \exp(-ik_{Tz,1}d_1)$,
$m_2^+ = k_{Lz,1}b_1 \exp(ik_{Lz,1}d_1) + k_{Lz,1}c_1 \exp(-ik_{Lz,1}d_1) - k \exp(ik_{Tz,1}d_1)$,
$m_2^- = k_{Lz,1}c_1 \exp(ik_{Lz,1}d_1) + k_{Lz,1}b_1 \exp(-ik_{Lz,1}d_1) - k \exp(-ik_{Tz,1}d_1)$,
$m_3^+ = a_{L,1}b_1 \exp(ik_{Lz,1}d_1) + a_{L,1}c_1 \exp(-ik_{Lz,1}d_1) + \exp(ik_{Tz,1}d_1)$,
$m_3^- = -a_{L,1}c_1 \exp(ik_{Lz,1}d_1) + a_{L,1}b_1 \exp(-ik_{Lz,1}d_1) + \exp(-ik_{Tz,1}d_1)$,
$m_4^+ = b_1 \exp(ik_{Lz,1}d_1) + c_1 \exp(-ik_{Lz,1}d_1) + \exp(ik_{Tz,1}d_1)$,
$m_4^- = c_1 \exp(ik_{Lz,1}d_1) + b_1 \exp(-ik_{Lz,1}d_1) + \exp(-ik_{Tz,1}d_1)$,

$n_1^+ = kb_2 \exp(i(k_{Tz,3} - k_{Lz,3})d_{l3}) + kc_2 \exp(i(k_{Tz,3} + k_{Lz,3})d_{l3}) + k_{Tz,3}$,
$n_1^- = kc_2 \exp(-i(k_{Tz,3} + k_{Lz,3})d_{l3}) + kb_2 \exp(i(k_{Lz,3} - k_{Tz,3})d_{l3}) + k_{Tz,3}$,
$n_2^+ = -k_{Lz,3}b_2 \exp(i(k_{Tz,3} - k_{Lz,3})d_{l3}) + k_{Lz,3}c_2 \exp(i(k_{Tz,3} + k_{Lz,3})d_{l3}) + k$,
$n_2^- = k_{Lz,3}c_2 \exp(-i(k_{Tz,3} + k_{Lz,3})d_{l3}) + k_{Lz,3}b_2 \exp(i(k_{Lz,3} - k_{Tz,3})d_{l3}) + k$,
$n_3^+ = -k_{L,2}b_2 \exp(i(k_{Tz,3} - k_{Lz,3})d_{l3}) + a_{L,2}c_2 \exp(i(k_{Tz,3} + k_{Lz,3})d_{l3}) - 1$,
$n_3^- = k_{L,2}c_2 \exp(-i(k_{Tz,3} + k_{Lz,3})d_{l3}) - a_{L,2}b_2 \exp(i(k_{Lz,3} - k_{Tz,3})d_{l3}) - 1$,
$n_4^+ = b_2 \exp(i(k_{Tz,3} - k_{Lz,3})d_{l3}) + c_2 \exp(i(k_{Tz,3} + k_{Lz,3})d_{l3}) - a_{T,2}$,
$n_4^- = c_2 \exp(-i(k_{Tz,3} + k_{Lz,3})d_{l3}) + b_2 \exp(i(k_{Lz,3} - k_{Tz,3})d_{l3}) - a_{T,2}$,

$a_{(L,T);1} = 2kk_{(L,T)z,1}/(k_{T,1}^2 - 2k^2)$,
$a_{(L,T);2} = 2kk_{(L,T)z,3}/(k_{T,1}^2 - 2k^2)$,

$\alpha_1 = \lambda k_{L,2}^2/(\mu_1(k_{T,1}^2 - 2k^2))$,
$\alpha_2 = \lambda k_{L,2}^2/(\mu_3(k_{T,3}^2 - 2k^2))$,

$b_{(1,2)} = (a_{T,(1,2)}a_{L,(1,2)} - 1)/(2a_{L,(1,2)})$,
$c_{(1,2)} = (a_{T,(1,2)}a_{L,(1,2)} - 1)/(2a_{L,(1,2)})$

μ_1, λ, and μ_3 are the appropriate Lame coefficients of the first, the second and the third layer materials. All unknown coefficients can be connected to the coefficient A_{1T}^{+} by the following expressions:

$$
\begin{aligned}
A_{1T}^{-} &= -A_{1T}^{+} m_3^{+}/m_3^{-}, \\
A_{1L}^{+} &= (b_1 + c_1 m_3^{+}/m_3^{-}) A_{1T}^{+}, \\
A_{1L}^{-} &= (c_1 + b_1 m_3^{+}/m_3^{-}) A_{1T}^{+}, \\
A_{2L}^{+} &= A_{1L}^{+} \frac{\exp(-ik_{Lz,2}d_1)}{2k_{Lz,2}\alpha_1} (\alpha_1 (m_2^{+} - m_3^{+} m_2^{-}/m_3^{-}) + k_{Lz,2}(m_4^{+} + m_3^{+} m_4^{-}/m_3^{-})) \\
A_{2L}^{-} &= A_{1T}^{+} \frac{\exp(-ik_{Lz,2}d_1)}{2k_{Lz,2}\alpha_1} \left(-\alpha_1 (m_2^{+} - m_3^{+} m_2^{-}/m_3^{-}) + k_{Lz,2}(m_4^{+} + m_3^{+} m_4^{-}/m_3^{-})\right) \\
A_{3L}^{+} &= A_{1L}^{+} \beta \left(b_2 \exp(ik_{Tz,3}d_3) + c_2 n_3^{+}/n_3^{-} \exp(-ik_{Tz,3}d_3)\right) \\
&\qquad \exp(ik_{Lz,2}d_{l2} - ik_{Lz,3}d) \\
A_{3L}^{-} &= A_{1T}^{+} \beta \left(c_2 \exp(ik_{Tz,3}d_3) + b_2 n_3^{+}/n_3^{-} \exp(-ik_{Tz,3}d_3)\right) \\
&\qquad \exp(ik_{Lz,2}d_{l2} - ik_{Lz,3}d_3) \\
A_{3T}^{+} &= A_{1T}^{+} \beta \exp(ik_{Lz,2}d_{l2} - ik_{Lz,3}d_3) \\
A_{3T}^{-} &= -A_{1T}^{+} \beta \, n_3^{+}/n_3^{-} \exp(ik_{Lz,2}d_{l2} - ik_{Lz,3}d_3)
\end{aligned}
$$

where

$$
\beta = \frac{\alpha_1 (m_2^{+} - m_3^{+} m_2^{-}/m_3^{-}) + k_{Lz,2}(m_4^{+} + m_3^{+} m_4^{-}/m_3^{-})}{-\alpha_1 (n_2^{+} - n_3^{+} n_2^{-}/n_3^{-}) + k_{Lz,2}(n_4^{+} + n_3^{+} n_4^{-}/n_3^{-})} \tag{C.1}
$$

Substituting the expressions for $A_{n,(L,T)}^{\pm}$ into the equations for $u_{(y,z),n}$, with $n = 1, 2, 3$, the displacement fields for Lamb modes in the three layered structure are found.

Bibliography

[1] C. R. Farrar and H. Sohn, "Pattern recognition for structural health monitoring", in *Workshop on Mitigation of Earthquake Disaster by Advanced Technologies* (Las Vegas, NV, USA) (Nov. 30 - Dec. 1, 2000).

[2] D. Adams, J. White, M. Rumsey, and C. Farrar, "Structural health monitoring of wind turbines: method and application to a HAWT", Wind Energy **14**, 603–623 (2011).

[3] H. Pfeiffer and M. Wevers, "Aircraft integrated structural health assessment–structural health monitoring and its implementation within the European project AISHA", in *Proceedings of EU Project Meeting on Aircraft Integrated Structural Health Assessment (AISHA)* (2007).

[4] Y. Liu and S. Nayak, "Structural health monitoring: State of the art and perspectives", JOM **64**, 789–792 (2012).

[5] (2014), URL `http://oxforddictionaries.com/definition/english/infrastructure`.

[6] J. Brownjohn, "Structural health monitoring of civil infrastructure", Philosophical Transactions of the Royal Society A: Mathematical, Physical and Engineering Sciences **365**, 589–622 (2007).

[7] E. Aktan, S. Chase, D. Inman, and D. Pines, "Monitoring and managing the health of infrastructure systems", in *Proceedings of the 2001 SPIE Conference on Health Monitoring of Highway Transportation Infrastructure* (2001).

[8] URL `www.enel.it/it-IT/`.

[9] C. J. Hellier, *Handbook of nondestructive evaluation.* (New York: MacGraw-Hill) (2001).

[10] P. C. Chang, A. Flatau, and S. C. Liu, "Review paper: Health monitoring of civil infrastructure", Structural health monitoring **2**, 257 (2003).

[11] P. E. Mix, *Introduction to Nondestructive Testing: A Training Guide*, 2nd edition (John Wiley & Sons, Inc., Hoboken, New Jersey) (2005).

[12] J. P. Lynch, "An overview of wireless structural health monitoring for civil structures", Philosophical Transactions of the Royal Society A: Mathematical, Physical and Engineering Sciences **365**, 345–372 (2007).

[13] C. R. Farrar and K. Worden, "An introduction to structural health monitoring", Philosophical Transactions of the Royal Society **365**, 303–315 (2007).

[14] D. McCann and M. Forde, "Review of NDT methods in the assessment of concrete and masonry structures", NDT & E International **34**, 71 – 84 (2001).

[15] D. Breysse, "Nondestructive evaluation of concrete strength: An historical review and a new perspective by combining NDT methods", Construction and Building Materials **33**, 139 – 163 (2012).

[16] A. M. Alani, M. Aboutalebi, and G. Kilic, "Integrated health assessment strategy using NDT for reinforced concrete bridges", NDT & E International **61**, 80 – 94 (2014).

[17] S. Bhaumik, M. Sujata, and M. Venkataswamy, "Fatigue failure of aircraft components", Engineering Failure Analysis **15**, 675–694 (2008).

[18] Airbus, "Innovative materials", URL `www.airbus.com/innovation/proven-concepts/in-design/innovative-materials/`.

[19] S. Pitt and R. Jones, "Multiple-site and widespread fatigue damage in aging aircraft", Engineering Failure Analysis **4**, 237 – 257 (1997).

[20] K. Diamanti and C. Soutis, "Structural health monitoring techniques for aircraft composite structures", Progress in Aerospace Sciences **46**, 342 – 352 (2010).

[21] I. Pitropakis, H. Pfeiffer, and M. Wevers, "Crack detection in aluminium plates for aerospace applications by electromagnetic impedance spectroscopy using flat coil sensors", Sensors and Actuators A: Physical **176**, 57 – 63 (2012).

[22] D. N. Alleyne and P. Cawley, "The interaction of Lamb waves with defects", Ultrasonics, Ferroelectrics and Frequency Control, IEEE Transactions on **39**, 381–397 (1992).

[23] M. Castaings, E. Le Clezio, and B. Hosten, "Modal decomposition method for modeling the interaction of Lamb waves with cracks", The Journal of the Acoustical Society of America **112**, 2567–2582 (2002).

[24] Z. Su, L. Ye, and Y. Lu, "Guided Lamb waves for identification of damage in composite structures: A review", Journal of Sound and Vibration **295**, 753 – 780 (2006).

[25] M. Rahammer, P. Menner, and G. Busse, "Thermal waves for NDE of aircraft: comparison of lockin thermography and lockin interferometry", Quantitative infra red thermography journal **10**, 42–54 (2013).

[26] P. Menner, H. Gerhard, and G. Busse, "Lockin-interferometry: Principle and applications in NDE", Strojniški vestnik **57**, 183–191 (2011).

[27] C. C. Ciang, J.-R. Lee, and H.-J. Bang, "Structural health monitoring for a wind turbine system: a review of damage detection methods", Measurement Science and Technology **19**, 122001 (2008).

[28] P. Johnson, J. TenCate, R. Guyer, and K. Van Den Abeele, "Resonant nonlinear ultrasound spectroscopy", (december 18 2001), US Patent 6,330,827.

[29] C. Doyle, "Fibre Bragg grating sensors an introduction to Bragg gratings and interrogation techniques", http://www.smartfibres.com (2003).

[30] I. Pitropakis, H. Pfeiffer, T. Gesang, S. Janssens, and M. Wevers, "Crack detection in aluminium 2024-T3 plates and in an Airbus A320 slat-track using electrical crack gauges", in *Proc. WCNDT 2012, 18th World Conference on Non-Destructive Testing*, 1–14 (2012).

[31] H. Pfeiffer, P. Heer, I. Pitropakis, G. Pyka, G. Kerckhofs, M. Patitsa, and M. Wevers, "Liquid detection in confined aircraft structures based on lyotropic percolation thresholds", Sensors and Actuators B: Chemical **161**, 791–798 (2012).

[32] Z. Su and L. Ye, "An intelligent signal processing and pattern recognition technique for defect identification using an active sensor network", Smart Materials and Structures **13**, 957 (2004).

[33] A. Raghavan and C. E. Cesnik, "Review of guided-wave structural health monitoring", Shock and Vibration Digest **39**, 91–116 (2007).

[34] J. Zhang, B. W. Drinkwater, P. D. Wilcox, and A. J. Hunter, "Defect detection using ultrasonic arrays: The multi-mode total focusing method", NDT & E International **43**, 123 – 133 (2010).

[35] B. Rocha, C. Silva, and A. Suleman, "Development of a PZT phased array and FBG network for structural health monitoring based on guided Lamb waves", CEAS Aeronautical Journal 1–10 (2013).

[36] V. T. Prado, R. T. Higuti, C. Kitano, Ó. Martínez-Graullera, and J. C. Adamowski, "Lamb mode diversity imaging for non-destructive testing of plate-like structures", NDT & E International **59**, 86 – 95 (2013).

[37] I. Park, Y. Jun, and U. Lee, "Lamb wave mode decomposition for structural health monitoring", Wave Motion **51**, 335 – 347 (2014).

[38] J. E. Michaels, "Detection, localization and characterization of damage in plates with an in situ array of spatially distributed ultrasonic sensors", Smart Materials and Structures **17**, 035035 (2008).

[39] Y. Lu, L. Ye, Z. Su, and N. Huang, "Quantitative evaluation of crack orientation in aluminium plates based on Lamb waves", Smart Materials and Structures **16**, 1907 (2007).

[40] A. J. Hunter, B. W. Drinkwater, and P. D. Wilcox, "Autofocusing ultrasonic imagery for non-destructive testing and evaluation of specimens with complicated geometries", NDT & E International **43**, 78 – 85 (2010).

[41] Y. Lu, L. Ye, and Z. Su, "Crack identification in aluminium plates using Lamb wave signals of a PZT sensor network", Smart Materials and Structures **15**, 839 (2006).

[42] P. S. Tua, S. T. Quek, and Q. Wang, "Detection of cracks in plates using piezo-actuated Lamb waves", Smart Materials and Structures **13**, 643 (2004).

[43] D. Dai and Q. He, "Structure damage localization with ultrasonic guided waves based on a time–frequency method", Signal Processing **96, Part A**, 21 – 28 (2014).

[44] G. Giridhara, V. Rathod, S. Naik, D. R. Mahapatra, and S. Gopalakrishnan, "Rapid localization of damage using a circular sensor array and Lamb wave based triangulation", Mechanical Systems and Signal Processing **24**, 2929 – 2946 (2010).

[45] M. Lemistre and D. Balageas, "Structural health monitoring system based on diffracted Lamb wave analysis by multiresolution processing", Smart Materials and Structures **10**, 504 (2001).

[46] Z. Su, X. Wang, Z. Chen, L. Ye, and D. Wang, "A built-in active sensor network for health monitoring of composite structures", Smart Materials and Structures **15**, 1939 (2006).

[47] S. Hosseini, S. Duczek, and U. Gabbert, "Damage localization in plates using mode conversion characteristics of ultrasonic guided waves", Journal of Nondestructive Evaluation **33**, 152–165 (2014).

[48] Y.-H. Kim, D.-H. Kim, J.-H. Han, and C.-G. Kim, "Damage assessment in layered composites using spectral analysis and Lamb wave", Composites Part B: Engineering **38**, 800 – 809 (2007).

[49] N. Quaegebeur, P. Micheau, P. Masson, and A. Maslouhi, "Structural health monitoring strategy for detection of interlaminar delamination in composite plates", Smart Materials and Structures **19**, 085005 (2010).

[50] D. Wang, L. Ye, Y. Lu, and F. Li, "A damage diagnostic imaging algorithm based on the quantitative comparison of Lamb wave signals", Smart Materials and Structures **19**, 065008 (2010).

[51] A. Leleux, P. Micheau, and M. Castaings, "Long range detection of defects in composite plates using Lamb waves generated and detected by ultrasonic phased array probes", Journal of Nondestructive Evaluation **32**, 200–214 (2013).

[52] N. Mori, S. Biwa, and T. Hayashi, "Reflection and transmission of Lamb waves at an imperfect joint of plates", Journal of Applied Physics **113**, 074901–074901–10 (2013).

[53] J. He, X. Guan, T. Peng, Y. Liu, A. Saxena, J. Celaya, and K. Goebel, "A multi-feature integration method for fatigue crack detection and crack length estimation in riveted lap joints using Lamb waves", Smart Materials and Structures **22**, 105007 (2013).

[54] J.-B. Ihn and F.-K. Chang, "Detection and monitoring of hidden fatigue crack growth using a built-in piezoelectric sensor/actuator network: II. Validation using riveted joints and repair patches", Smart Materials and Structures **13**, 621 (2004).

[55] U. Zerbst, C. Klinger, and D. Klingbeil, "Structural assessment of railway axles – a critical review", Engineering Failure Analysis **35**, 54 – 65 (2013).

[56] T. Kang, D.-H. Lee, S.-J. Song, H.-J. Kim, Y.-D. Jo, and H.-J. Cho, "Enhancement of detecting defects in pipes with focusing techniques", NDT & E International **44**, 178 – 187 (2011).

[57] P. B. Nagy, F. Simonetti, and G. Instanes, "Corrosion and erosion monitoring in plates and pipes using constant group velocity lamb wave inspection", Ultrasonics (2014).

[58] M. Siqueira, C. Gatts, R. da Silva, and J. Rebello, "The use of ultrasonic guided waves and wavelets analysis in pipe inspection", Ultrasonics **41**, 785 – 797 (2004).

[59] B. Verma, T. K. Mishra, K. Balasubramaniam, and P. Rajagopal, "Interaction of low-frequency axisymmetric ultrasonic guided waves with bends in pipes of arbitrary bend angle and general bend radius", Ultrasonics **54**, 801 – 808 (2014).

[60] S. K. Chakrapani, D. Barnard, and V. Dayal, "Nondestructive evaluation of helicopter rotor blades using guided Lamb modes", Ultrasonics **54**, 826 – 833 (2014).

[61] Z. Hameed, Y. Hong, Y. Cho, S. Ahn, and C. Song, "Condition monitoring and fault detection of wind turbines and related algorithms: A review", Renewable and Sustainable Energy Reviews **13**, 1 – 39 (2009).

[62] D. N. Alleyne and P. Cawley, "Optimization of Lamb wave inspection techniques", NDT & E International **25**, 11 – 22 (1992).

[63] L. Ge, X. Wang, and C. Jin, "Numerical modeling of PZT-induced Lamb wave-based crack detection in plate-like structures", Wave Motion – (2014).

[64] Y. Y. Kim, J. C. Hong, S. W. Han, I. K. Kim, and C. I. Park, "The effectiveness of the continuous wavelet transform in the analysis of

elastic waves", in *Ultrasonics, 2003 IEEE Symposium on*, volume 2, 1388–1391 Vol.2 (2001).

[65] W. Zhu and J. L. Rose, "Lamb wave generation and reception with time-delay periodic linear arrays: A BEM simulation and experimental study", Ultrasonics, Ferroelectrics and Frequency Control, IEEE Transactions on **46**, 654–664 (1999).

[66] P. D. Wilcox, M. J. S. Lowe, and P. Cawley, "Mode and transducer selection for long range Lamb wave inspection", Journal of Intelligent Material Systems and Structures **12**, 553–565 (2001).

[67] J. Qiu and H. Ji, "Research on applications of piezoelectric materials in smart structures", Frontiers of Mechanical Engineering **6**, 99–117 (2011).

[68] J. Pohl, C. Willberg, U. Gabbert, and G. Mook, "Experimental and theoretical analysis of Lamb wave generation by piezoceramic actuators for structural health monitoring", Experimental Mechanics **52**, 429–438 (2012).

[69] X. Liu, Z. Jiang, and L. Ji, "Investigation on the design of piezoelectric actuator/sensor for damage detection in beam with Lamb waves", Experimental Mechanics **53**, 485–492 (2013).

[70] C. Willberg, S. Duczek, and U. Gabbert, "Increasing the scanning range of Lamb wave based SHM systems by optimizing the actuator–sensor design", CEAS Aeronautical Journal 1–12 (2013).

[71] T. Porchez and E. Ringgaard, "Mode and direction selectivity for ultrasonic SHM applications using piezo-composite transducers and dedicated electronics", Technical Report, AISHA II - EU- FP7 - CP 212912 (2011).

[72] Y. G.-U. Ricón, F. C. Segovia, and F. M. de Espinosa Freijo, "Lamb waves generation on thin plates using piezocomposites", Journal of the European Ceramic Society **27**, 4147 – 4151 (2007).

[73] B. C. Lee and W. J. Staszewski, "Sensor location studies for damage detection with Lamb waves", Smart Materials and Structures **16**, 399 (2007).

[74] G. Shui, J.-Y. Kim, J. Qu, Y.-S. Wang, and L. J. Jacobs, "A new technique for measuring the acoustic nonlinearity of materials using Rayleigh waves", NDT & E International **41**, 326 – 329 (2008).

[75] C. Pruell, J.-Y. Kim, J. Qu, and L. Jacobs, "A nonlinear-guided wave technique for evaluating plasticity-driven material damage in a metal plate", NDT & E International **42**, 199 – 203 (2009).

[76] Z. Su, C. Zhou, M. Hong, L. Cheng, Q. Wang, and X. Qing, "Acousto-ultrasonics-based fatigue damage characterization: Linear versus nonlinear signal features", Mechanical Systems and Signal Processing **45**, 225 – 239 (2014).

[77] C. Zhou, M. Hong, Z. Su, Q. Wang, and L. Cheng, "Evaluation of fatigue cracks using nonlinearities of acousto-ultrasonic waves acquired by an active sensor network", Smart Materials and Structures **22**, 015018 (2013).

[78] M. Hong, Z. Su, Q. Wang, L. Cheng, and X. Qing, "Modeling nonlinearities of ultrasonic waves for fatigue damage characterization: Theory, simulation, and experimental validation", Ultrasonics **54**, 770 – 778 (2014).

[79] P. Blanloeuil, A. Meziane, and C. Bacon, "Numerical study of nonlinear interaction between a crack and elastic waves under an oblique incidence", Wave Motion **51**, 425 – 437 (2014).

[80] J. H. Cantrell and W. T. Yost, "Nonlinear ultrasonic characterization of fatigue microstructures", International Journal of Fatigue **23, Supplement 1**, 487 – 490 (2001).

[81] M. Amura and M. Meo, "Prediction of residual fatigue life using nonlinear ultrasound", Smart materials and structures **21** (2012).

[82] A. Kumar, C. J. Torbet, T. M. Pollock, and J. W. Jones, "In situ characterization of fatigue damage evolution in a cast al alloy via nonlinear ultrasonic measurements", Acta Materialia **58**, 2143 – 2154 (2010).

[83] A. Srivastava and F. L. di Scalea, "On the existence of antisymmetric or symmetric Lamb waves at nonlinear higher harmonics", Journal of Sound and Vibration **323**, 932 – 943 (2009).

[84] B. WU, B. sheng YAN, and C. fu HE, "Nonlinear ultrasonic characterizing online fatigue damage and in situ microscopic observation", Transactions of Nonferrous Metals Society of China **21**, 2597 – 2604 (2011).

[85] I. Solodov and G. Busse, "Listening for nonlinear defects: A new methodology for nonlinear NDE.", AIP Conference Proceedings **1022**, 569 – 572 (2008).

[86] I. Solodov, N. Krohn, and G. Busse, "CAN: an example of nonclassical acoustic nonlinearity in solids", Ultrasonics **40**, 621 – 625 (2002).

[87] I. Y. Solodov, "Ultrasonics of non-linear contacts: propagation, reflection and NDE-applications", Ultrasonics **36**, 383 – 390 (1998).

[88] P. B. Nagy, "Fatigue damage assessment by nonlinear ultrasonic material characterization", Ultrasonics **36**, 375–381 (1998).

[89] G. Shkerdin and C. Glorieux, "Nonlinear modulation of Lamb modes by clapping delamination", The Journal of the Acoustical Society of America **124**, 3397–3409 (2008).

[90] Y. Ohara, S. Horinouchi, M. Hashimoto, Y. Shintaku, and K. Yamanaka, "Nonlinear ultrasonic imaging method for closed cracks using subtraction of responses at different external loads", Ultrasonics **51**, 661 – 666 (2011).

[91] V. Zaitsev, L. Matveev, and A. Matveyev, "On the ultimate sensitivity of nonlinear-modulation method of crack detection", NDT & E International **42**, 622 – 629 (2009).

[92] X. Liu, Z. Dao, J. Zhu, W. Qu, X. Gong, K. Van Den Abeele, and L. Ma, "Localization of material defects using nonlinear resonant ultrasound spectroscopy under asymmetric boundary conditions", Physics Procedia - International Congress on Ultrasonics, Santiago de Chile, January 2009 **3**, 55 – 61 (2010).

[93] K. V. D. Abeele, A. Sutin, J. Carmeliet, and P. A. Johnson, "Micro-damage diagnostics using nonlinear elastic wave spectroscopy (NEWS)", NDT & E International **34**, 239 – 248 (2001).

[94] H. J. Lim, H. Sohn, M. P. DeSimio, and K. Brown, "Reference-free fatigue crack detection using nonlinear ultrasonic modulation under various temperature and loading conditions", Mechanical Systems and Signal Processing **45**, 468 – 478 (2014).

[95] H. Sohn, H. J. Lim, M. P. DeSimio, K. Brown, and M. Derriso, "Nonlinear ultrasonic wave modulation for online fatigue crack detection", Journal of Sound and Vibration **333**, 1473 – 1484 (2014).

[96] V. Zaitsev, V. Nazarov, V. Gusev, and B. Castagnede, "Novel nonlinear-modulation acoustic technique for crack detection", NDT & E International **39**, 184 – 194 (2006).

[97] T. J. Ulrich, P. A. Johnson, and A. Sutin, "Imaging nonlinear scatterers applying the time reversal mirror", Journal of the Acoustical Society of America **119**, 1514–1518 (2006).

[98] K.-Y. Jhang, "Nonlinear ultrasonic techniques for nondestructive assessment of micro damage in material: A review", International Journal of Precision Engineering and Manufacturing **10**, 123–135 (2009).

[99] B. Auld and M. Tan, "Symmetrical Lamb wave scattering at a symmetrical pair of thin slots", in *Ultrasonics Symposium, 1977*, 61–66 (1977).

[100] M. Tan and B. Auld, "Normal mode variational method for two- and three-dimensional acoustic scattering in an isotropic plate", in *1980 Ultrasonics Symposium*, 857–861 (1980).

[101] S. Rokhlin, "Interaction of Lamb waves with elongated delaminations in thin sheets", Int. Adv. Nondestr. Test **6**, 263–285 (1979).

[102] S. Rokhlin, "Diffraction of Lamb waves by a finite crack in an elastic layer", The Journal of the Acoustical Society of America **67**, 1157–1165 (1980).

[103] S. I. Rokhlin, "Resonance phenomena of Lamb waves scattering by a finite crack in a solid layer", The Journal of the Acoustical Society of America **69**, 922–928 (1981).

[104] L. Wang and J. Shen, "Scattering of elastic waves by a crack in a isotropic plate", Ultrasonics **35**, 451 – 457 (1997).

[105] M. J. S. Lowe, P. Cawley, J.-Y. Kao, and O. Diligent, "The low frequency reflection characteristics of the fundamental antisymmetric Lamb wave A0 from a rectangular notch in a plate", The Journal of the Acoustical Society of America **112**, 2612–2622 (2002).

[106] B. C. Lee and W. J. Staszewski, "Modelling of Lamb wave interaction with open and closed fatigue cracks for damage detection", IOP Conference Series: Materials Science and Engineering **10**, 012059 (2010).

[107] B. Hosten, L. Moreau, and M. Castaings, "Reflection and transmission coefficients for guided waves reflected by defects in viscoelastic

material plates", The Journal of the Acoustical Society of America **121**, 3409–3417 (2007).

[108] D. Broda, W. Staszewski, A. Martowicz, T. Uhl, and V. Silberschmidt, "Modelling of nonlinear crack–wave interactions for damage detection based on ultrasound—a review", Journal of Sound and Vibration **333**, 1097 – 1118 (2014).

[109] G. Konstantinidis, B. W. Drinkwater, and P. D. Wilcox, "The temperature stability of guided wave structural health monitoring systems", Smart Materials and Structures **15**, 967 (2006).

[110] A. Marzani and S. Salamone, "Numerical prediction and experimental verification of temperature effect on plate waves generated and received by piezoceramic sensors", Mechanical Systems and Signal Processing **30**, 204 – 217 (2012).

[111] S. J. Lee and H. Sohn, "Lamb wave tuning curve calibration with improved PZT modeling", (2009).

[112] H. Lamb, "On waves in an elastic plate", Proceedings of the Royal Society of London. Series A **93**, 114–128 (1917).

[113] I. S. Sokolnikoff, *Mathematical Theory of Elasticity* (R.E. Krieger Publishing Company) (1956).

[114] J. D. Achenbach, *Wave propagation in elastic solids* (North-Holland) (1999).

[115] H. B. Phillips, *Vector analysis* (John Wiley Sons, New York) (1933).

[116] G. Shkerdin and C. Glorieux, "Nonlinear clapping modulation of Lamb modes by normally closed delamination", Ultrasonics, Ferroelectrics and Frequency Control, IEEE Transactions on **57**, 1426–1433 (2010).

[117] G. Shkerdin and C. Glorieux, "Lamb mode conversion in an absorptive bi-layer with a delamination", The Journal of the Acoustical Society of America **118**, 2253–2264 (2005).

[118] C. Glorieux, K. Van de Rostyne, K. Nelson, W. Gao, W. Lauriks, and J. Thoen, "On the character of acoustic waves at the interface between hard and soft solids and liquids", The Journal of the Acoustical Society of America **110**, 1299–1306 (2001).

[119] K. Van de Rostyne, C. Glorieux, W. Gao, W. Lauriks, and J. Thoen, "Experimental investigation of leaky Lamb modes by an optically induced grating", Ultrasonics, Ferroelectrics and Frequency Control, IEEE Transactions on **49**, 1245–1253 (2002).

[120] G. Shkerdin and C. Glorieux, "Interaction of Lamb modes with delaminations in plates coated by highly absorbing materials", Ultrasonics, Ferroelectrics and Frequency Control, IEEE Transactions on **54**, 368–377 (2007).

[121] M. F. Hamilton, "Fundamentals and applications of non-linear acoustics", in *Non-linear wave propagation in mechanics AMD*, volume 77 (The American Society of Mechanical Engineers, New York) (1986).

[122] N. Krohn, R. Stoessel, and G. Busse, "Acoustic non-linearity for defect selective imaging", Ultrasonics **40**, 633 – 637 (2002).

[123] K. Pfleiderer, N. Krohn, R. Stoessel, and G. Busse, "Defect-selective imaging by nonlinear scanning vibrometry and by nonlinear air-coupled ultrasound inspection", in *NDT.net, Proceedings of the 8th ECNDT, Barcelona, June 2002*, volume 8 (2003).

[124] M. Meo and G. Zumpano, "Nonlinear elastic wave spectroscopy identification of impact damage on a sandwich plate", Composite Structures **71**, 469 – 474 (2005).

[125] R. Serway and J. Jewett, *Physics for scientists and engineers* (Cengage Learning) (2013).

[126] L. D. Landau and E. M. Lifshitz, *Fluid Mechanics* (Pergamon Press, London) (1959).

[127] T. D. Rossing, *Springer Handbook of Acoustics* (Springer New York) (2007).

[128] A. J. Moulson and J. M. Herbert, *Electroceramics: Materials, Properties, Applications, Second Edition* (John Wiley & Sons Ltd) (2003).

[129] V. Piefort, "Finite element modelling of piezoelectric active structures", Ph.D. thesis, Faculty of Applied Sciences - ULB (2001).

[130] MEGGITT Sensing Systems - Ferroperm Piezoceramics, production sheet.

[131] URL `www.meggittsensingsystems.com`.

[132] N. Bosman, "Mode selection of Lamb waves by multiplexed piezoelectric transducer", Master's thesis, KU Leuven (2013).

[133] F. Benmeddour, E. Moulin, J. Assaad, S. Djili, *et al.*, "Generation of a selected Lamb mode by piezoceramic transducers: Application to nondestructive testing of aeronautical structures", Piezoelectric materials and devices-Practice and applications (2013).

[134] H. Pfeiffer, "Aircraft integrated structural health assessment II", URL `http://sirius.mtm.kuleuven.be/Research/AISHA-II/`, FP7-AAT-2007-RTD-1 Project Number: 212912.

[135] URL `http://commons.wikimedia.org/wiki/File:Wing.slat.600pix.jpg`.

[136] URL `www.airliners.net`.

[137] D. G. R. William D. Callister, *Fundamentals of Materials Science and Engineering* (John Wiley & Sons Canada) (2005).

[138] S. Vanlanduit, R. Longo, P. Guillaume, R. Pintelon, and J. Dirck, "Tracking of cracks in fatigue experiments using nonlinear propagation of multi-sine surface acoustic waves", in *Ultrasonics Symposium, 2007. IEEE*, 686 –689 (2007).

[139] National Transportation Safety Board, "Aircraft Accident Report: AAR89-03", Technical Report, Washington D.C., United States of America Government (1989).

[140] Federal Aviation Administration, "China Airlines Flight 120, Boeing B-737-800, B18616", Technical Report, Washington D.C., United States of America Government (2007).

[141] B. Verstraeten, "Development of a diagnostic method for thermoelastic characterization of coatings using laser-ultrasonics", Ph.D. thesis, KU Leuven (2013).

[142] MathWorks, "corr", URL `www.mathworks.co.uk/help/stats/corr.html`.

Publication list

Publications in international journals

L. Liu, S. Creten, Y. Firdaus, A. Flores Cuautle, M. Kouyaté, M. Van der Auweraer, C. Glorieux - *Fluorescence spectra shape based dynamic thermometry* - Applied Physics Letters (2014)

Communications at international conferences and symposia

S. Creten, C. Glorieux - *Piezoelectric detection of vibrating closed cracks* - Anglo-French Physical Acoustics Conference (AFPAC 2014) - Surrey UK (2014)

U. Harmankaya, A. Kaslilar, B. Verstraeten, S. Creten, C. Glorieux, K. Wapenaar, D. Draganov - *Locating a Buried Cavity Using Ghost Scattered Waves in a Scale-model Experiment* - 76th EAGE Conference & Exphibition - Amsterdam (2014)

S. Creten, C. Glorieux, E. Ringgaard, T. Porchez - *Novel approaches of nonlinear ultrasonics in SHM* - AISHA II OPEN PROJECT MEETING - Leuven (2011)

S. Creten, C. Glorieux , E. Ringgaard, T. Porchez - *Detection of closed defects in vibrating structures with piezo-excited and detected acoustic waves* - 5th International Conference on Emerging Technologies in Non-destructive Testing - Ioannina (2011)

Communications at other conferences and symposia

S. Creten, C. Glorieux - *Crack dectection by demodulation of nonlinear cross-modulation of guided waves* - ATF seminary - Leuven (2012)

S. Creten, C. Glorieux - *Early crack detection in vibrating structures with piezo-excited and detected acoustic waves* - 2012 Annual General Scientific Meeting of the Belgian Physical Society - Brussel (2012)

S. Creten, C. Glorieux - *A concept for detection of closed defects in vibrating structures with piezo-excited and detected acoustic waves* - 2011 Annual General Scientific Meeting of the Belgian Physical Society - Namur (2011)